

# VLA observations of $\gamma$ -loud AGN on the southern hemisphere

Masterarbeit am Lehrstuhl für Astronomie  
von  
Jonas Andreas Walter Ringholz



Fakultät für Physik und Astronomie  
Julius-Maximilians-Universität Würzburg

Würzburg, den 17. Januar 2018

*Verantwortlicher Hochschullehrer:*

Prof. Dr. M. Kadler



---

## Zusammenfassung

Aktive Galaxien Kerne (AGK) sind die innersten Teile einer Galaxie, in der ein supermassives schwarzes Loch Massen akkretiert. AGK können anhand von drei Parametern unterschieden werden, dem Verhältnis zwischen optischen Fluss und Radiofluss, Radioleuchtkraft und Sichtwinkel. In folge der Akkretion bilden radio laute AGK hoch relativistische Plasmajets in beide Richtungen entlang ihrer Rotationsachse, die Ausdehnungen bishin zu megaparsec Skalen erreichen können. Unter großen Sichtwinkel werden diese Quellen Radio-Galaxien und unter kleinen Sichtwinkel Blazare genannt. [Fanaroff & Riley \(1974\)](#) fanden einen Zusammenhang zwischen Leuchtkraft und Morphologie von Radio-Galaxien. Die leuchtschwächeren Objekte (FR1 Galaxien) mit einer ausgedehnten Leuchtkraft von  $\log(L_{\text{ext}}/W_s^{-1}) < 24.5$  besitzen einen hellen Kern und oft einen zweiseitigen Jet mit komplexen Schwadenstrukturen und abnehmender Oberflächenhelligkeit in den äußeren Bereichen. Die leuchtstärkeren Quellen (FR2 Galaxien) mit Leuchtkräften von  $\log(L_{\text{ext}}/W_s^{-1}) > 26$  zeigen einen hellen Kern und meist einen einseitig sichtbaren schmalen Jet und Hotspots umgeben mit handelartiger Struktur auf beiden Seiten am Ende des Jets, in denen das Plasma durch das intergalaktische Medium abgebremst wird. Auch Blazare können in leuchtschwächere BL Lacs und die leuchtstärkere Flachspektrum Radio Quasare (FSRQs) unterteilt werden. Blazare besitzen ein flaches kerndominiertes Spektrum, das bei niedrigen Frequenz steil wird durch den Einfluss von relativistischen beaming-Effekten. Nach dem vereinheitlichten Modell von AGK sollten BL Lacs die rotierten und gebeamten Pendant zu FR1 Galaxien und FSRQs die rotierten und gebeamten Pendant zu FR2 Galaxien sein.

Zur Überprüfung dieser Theorie muss die ausgedehnte Emission von Blazaren studiert werden. Mit Hilfe dieser könnte ein Zusammenhang zwischen interner Jetenergie und Jetgeschwindigkeit hergestellt werden, da diese nicht durch Beamingeffekte beeinflusst wird und somit direkt zur internen Jetenergie proportional ist. [Kharb et al. \(2010\)](#) studierten Morphologie und ausgedehnte Leuchtkraft von Blazaren aus dem MOJAVE Beobachtungsprogramm (MOJAVE Sample) an der nördlichen Hemisphäre. Diese Studie erweitert das Sample auf die südlich Hemisphäre erweitern. Hierfür wurden die sechs  $\gamma$ -lautesten AGK aus dem TANAMI Beobachtungsprogramm (TANAMI Sample) ausgewählt die gleichzeitig auch mit dem 'Very Large Array' 'VLA bei  $\nu = 1.4$  GHz beobachtet wurden und zum Vergleich auch drei  $\gamma$ -leise Quellen. Leuchtkraft und Morphologie werden bei verschiedenen Frequenzen studiert. Alle FSRQs besitzen eine Leuchtkraft typisch für FR2 Objekte. Eine dieser Objekte zeigt auch zwei Hotspots (1104-445) und eine Quelle einen Hotspot (0402-362). Alle BL Lac Objekte weisen Leuchtkräfte im Übergangsbereich zwischen FR1 und FR2 auf, mit Ausnahme von 0521-365, die eine Leuchtkraft direkt auf der Grenze zu FR2 Objekten besitzt. Diese spezielle Quelle weist desweiteren einen einseitig sichtbaren Jet auf und einen Hotspot auf der Gegenseite, was für eine FR2 Struktur spricht. Alle anderen BL Lacs zeigen eher eine FR1-artige Morphologie. Für alle Quellen mit bestimmter scheinbarer Jetgeschwindigkeit konnte auch eine Einhüllende bezüglich dem Zusammenhang scheinbarer Jetgeschwindigkeit

---

und Kernleuchtkraft mit einem maximalen Lorentzfaktor von  $\gamma \approx 58$  gefunden werden. Für einzelne Quellen kann auch der Sichtwinkel eingegrenzt werden, durch die Messung des projizierten Jetöffnungswinkels und dem Vergleich von typischen Jetöffnungswinkel von FR1 Galaxien (Parma et al. (1987)) und FR2 Galaxien (Jeyakumar & Saikia (2000)). Auch werden spezielle Verhalten in den Morphologien von einzelnen Quellen diskutiert, wie Jetkrümmung in den meisten Quellen und einseitige Hotspots in 0521-365 und 0402-362. Für 1104-445 wird eine Diskrepanz zwischen der Größe der Quelle auf kiloparsec Skalen und der hohen scheinbaren Überlichtgeschwindigkeit bzw dem kleinen Sichtwinkel von  $\varphi \approx 1^\circ$  der Quelle entdeckt, was eine Überprüfung der Jetgeschwindigkeit in weietren Beobachtungen lohnenswert macht.

---

## Abstract

Active galactic nuclei are the innermost parts of a galaxy, in which a super massive black hole is accreting large masses. AGN can be distinguished by three parameters radio loudness, radio luminosity and the inclination angle. Due to this accretion the radio loud subclass of these sources form highly relativistic particle jets, on both sides alongside their rotation axis extending up to megaparsec-scales. When observed edge on, these sources are called radio galaxies and when observed pole on blazars. [Fanaroff & Riley \(1974\)](#) find a correlation between the morphology of radio galaxies and their luminosity. The lower luminous object (FR1 galaxies) with an extended luminosity of  $\log(L_{\text{ext}}/W\text{s}^{-1}) < 24.5$  feature a bright core, often a two sided jet, a plume like structure and declining surface-brightness in the outer parts. The more luminous objects (FR2 galaxies) with  $\log(L_{\text{ext}}/W\text{s}^{-1}) > 26$  show a bright core, a often one sided jet and hotspots with lobes on two sides along the jet axis where the jet terminates in the intergalactic medium. Also the class of blazars can be subdivided in two classes according to their luminosity BL Lacs, with low luminosity and flat spectrum radio quasars (FSRQs) with high luminosity. Both classes feature a core dominated flat radio spectrum with steepening at low frequencies, because of relativistic beaming effects. According to the unification scheme of AGN BL Lacs are the beamed and rotated counterparts of FR1 galaxies, whereas FSRQs are the beamed and rotated counterparts of FR2 galaxies.

To test this connection the extended emission of blazars has to be studied, which can also be a hint for the jet-power of the source, because extended emission is free from beaming effects. [Kharb et al. \(2010\)](#) studied blazars from the MOJAVE sample on the northern hemisphere at  $\nu = 1.4$  GHz with the VLA and found deviations from the unification scheme like BL Lac with hotspots. In this study the sample is extended to the southern hemisphere. Six of the  $\gamma$ -loudest AGN of the TANAMI sample also observed with the VLA at  $\nu = 1.4$  GHz and three  $\gamma$ -quiet sources for comparison are chosen. For the sample the extended radio luminosity together with the morphology is studied at different frequencies. All FSRQs of the sample show extended luminosities in the regime typical for FR2 objects. One of them show also two possible hotspots (1104-445) and one of them only one. All BL Lacs feature extended luminosities in the regime between FR1 and FR2 except the source 0521-365 which is on the border to the FR2 objects. This special object also show an one sided jet and a hotspot on the counterjet side. Both a hint for a more FR2 behavior. All other BL Lacs show a more FR1 like structure. For all sources with measured apparent jet speed also an envelope function for the the connection between the core luminosity and the apparent jet speed could be constrained.

For single sources also the inclination angle could be constrained by measuring the projected jet opening angles of the sources and comparing it with typical jet opening angle of FR1 galaxies ([Parma et al. \(1987\)](#)) and FR2 galaxies ([Jeyakumar & Saikia \(2000\)](#)). Also special behavior in morphologies at the single sources are discussed such as jet bending in most of the sources and only one hotspot in the sources 0521-365 and 0402-

---

362. For 1104-445 also a discrepancy between kiloparsec size and an high superluminal apparent jet speed respectively the low inclination angle of  $\varphi \approx 1^\circ$  is detected, leading to the assumption that more observations of this object are necessary to verify the jetspeed measured by [Trüstedt \(2013\)](#).

# Contents

<b>1. Scientific context</b>	<b>3</b>
1.1. Active galactic nuclei	3
1.2. Radioastronomy	13
<b>2. Analyzing blazars on kpc-scales</b>	<b>25</b>
2.1. Data-processing	25
2.1.1. Basic calibration	25
2.1.2. Hybrid-imaging	27
2.1.3. Modelfitting	32
2.2. Sample-selection	33
2.3. Analysis methods for blazars	42
2.3.1. Extended radio-luminosity	42
2.3.2. Constraining the inclination angles of AGN	43
<b>3. Results</b>	<b>47</b>
3.1. Sample results	47
3.1.1. Luminosity and spectral study	47
3.1.2. Morphology	48
3.2. Single source results	52
0402-362	52
0426-380	53
0438-436	56
0521-365	59
0537-441	60
0625-354	64
1104-445	72
1313-333	80
2155-304	80
<b>4. Conclusion and outlook</b>	<b>91</b>
<b>Danksagung</b>	<b>93</b>
<b>List of Figures</b>	<b>95</b>
<b>List of Tables</b>	<b>103</b>

*Contents*

---

<b>Bibliography</b>	<b>105</b>
<b>A. Appendix</b>	<b>109</b>
<b>Selbstständigkeitserklärung</b>	<b>113</b>

# 1. Scientific context

## 1.1. Active galactic nuclei

Active galactic nuclei (AGN) are among the most luminous object in our universe, emitting radiation in the whole electromagnetic spectrum. The first AGNs were discovered in the 1940s by [Seyfert \(1943\)](#) in the optical spectrum in the center of spiral galaxies. In the early time of AGN observation the different subclasses of AGN are thought to be completely different astronomical object. Now it is known that all these sources can indeed divided in subclasses but can unified in one AGN model.

The model is illustrated in [Fig.1.1](#) created by [Beckmann & Shrader \(2012\)](#). According to [Antonucci \(1993\)](#) an active galactic nucleus is the very center of a galaxy which is in an active state. Meaning the central super-massive black hole with a masses typically ranging between  $10^7 M_{\odot} \lesssim M \lesssim 10^{10} M_{\odot}$  ([Valtonen et al. \(2008\)](#)) accretes mass. Near the accretion disc, there are several gas clouds, which rotate with speeds of typically  $v \approx 10^4 \text{ km s}^{-1}$  ([Osterbrock & Shuder \(1982\)](#)), so the emission and absorption lines of these clouds are Doppler-broaden. Because of the broad emission lines this region is also called 'broad line region' (BLR). As shown in [Fig.1.1](#) the central region including the black hole, the accretion disk and the BLR is surrounded by a dust torus, which absorbs most radiation arriving the torus because of Mie-scattering of dust particles of different sizes and geometries ([Mie \(1908\)](#)) and absorption and is reradiated in the infrared regime. [Czerny et al. \(2004\)](#) and [Gaskell et al. \(2004\)](#) model these extinction for diferent types of AGN. At larger distances to the accretion disk the so called 'narrow line regions' (NLR) is located above and below the disk. The clouds of this region are moving slower than the clouds of the BLR,  $v \approx (200 - 700) \text{ km s}^{-1}$  ([Dahari & De Robertis \(1988\)](#)), and thus the emission lines are less broaden than in the BLR.

According to [Antonucci \(1993\)](#) some AGN form also plasma jets alongside the rotation axis of the accretion disc . These jets beginning near the black hole and extending in opposite direction alongside the rotation axis, because of conservation of momentum of the whole object. The plasma particles can reach high relativistic energies and the largest measured structures extend up to Mpc-scales, see [Lara et al. \(2001\)](#). Because of the acceleration of the plasma particles in the high magnetic fields in the jets, caused by the charged particles in the accretion disk, the jets are emitting synchrotron emission, which is a broadband emission most prominent in the radio regime. If the produced radio flux is much higher than the optical flux of the source is referred to as radio loud. So [Kellermann et al. \(1989\)](#) introduced the radio loudness  $R_{r-o}$  as the relation between

the radio flux  $S_r$  at  $\nu = 5$  GHz and the optical flux  $S_o$  in the optical B-band

$$R_{r-o} = \frac{S_r}{S_o} \quad (1.1.1)$$

An AGN is called radio quiet if  $0 < R_{r-o} < 1$  and radio-loud for  $R_{r-o} > 10$ . The subclasses of AGN can be categorized by three parameters, which are the radio-loudness, the inclination angle between the line of sight and the rotation axis and for the radio-loud ones also the radio-luminosity of the source.

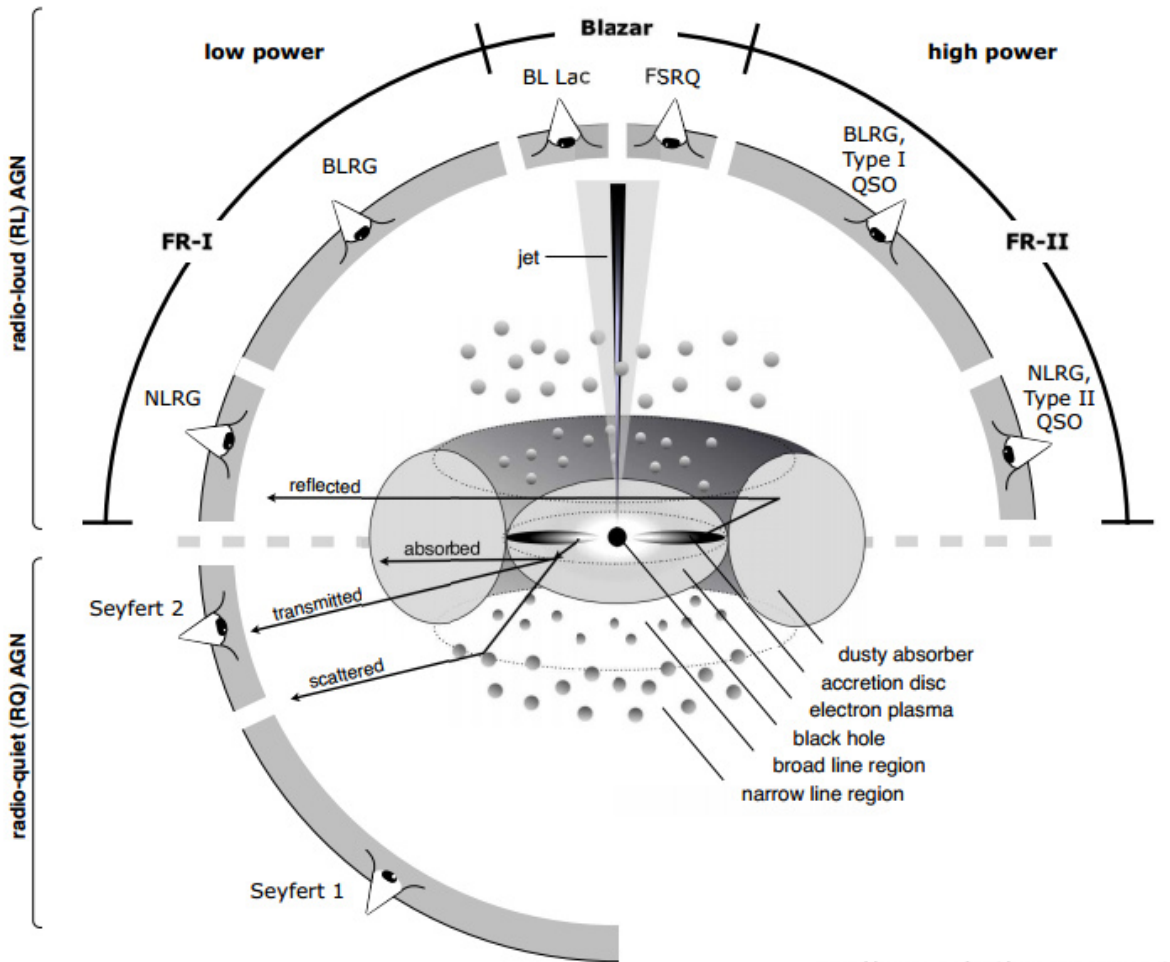
Radio loud AGN are typically hosted by large elliptical galaxies. Objects observed at high viewing angles are called radio galaxies. According to [Osterbrock et al. \(1976\)](#) the radio-galaxies with both kinds of emission and absorption lines are called broad line radio galaxies (BLRGs) and the ones with only narrow lines in the spectrum are called according to [Costero & Osterbrock \(1977\)](#) narrow line radio galaxies (NLRGs). Objects observed at very low inclination angles are called blazars ([Urry & Padovani \(1995\)](#)), where the emitted synchrotron-radiation is dominated by relativistic effects like Doppler boosting, due to this effect, the spectrum of these sources is flat in the radio regime with possible steepening at lower frequencies. Also this kind of AGN can be divided in two classes BL Lac object and flat spectrum radio quasars (FSRQs). In the case of BL Lac objects the most parts of the spectrum is featureless and the radio luminosity is smaller compared to FSRQs. The FSRQs show line-emission and in most cases are more luminous than BL Lacs. According to [Padovani & Giommi \(1995\)](#) Bl Lac objects can be further divided with respect to their synchrotron peak frequency meaning in high-peaked Bl Lac (HBL) and low-peaked Bl Lac (LBL). [Padovani & Giommi \(1995\)](#) describe also that HBLs feature a lower luminosity than LBLs, which can reach luminosity comparable to FSRQs.

## Fanaroff-Riley classification

Because the plasma-jets of radio loud AGN has linear sizes of several mega-parsec these sources can also be distinguished by their radio morphology. [Fanaroff & Riley \(1974\)](#) did this by measuring the complete size of the object  $s$  and the distance  $d$  between the two brightest emission regions outside the central region and calculate the relation between these two quantities

$$f = \frac{d}{s}. \quad (1.1.2)$$

[Fanaroff & Riley \(1974\)](#) called the sources with  $f < 0.5$  Fanaroff-Riley type 1 objects and sources with  $f > 0.5$  Fanaroff-Riley type 2 objects. They found also that the most type 1 objects feature a radio luminosity of  $L_{178\text{MHz}} < 2 \cdot 10^{25} \text{ W Hz}^{-1}$  and type 2 sources  $L_{178\text{MHz}} > 2 \cdot 10^{25} \text{ W Hz}^{-1}$ . The typical detailed morphology of a FR1 object is shown in figure 1.2 and that of a FR2 radio galaxy in Fig.1.3. FR1 galaxies show a bright core and a often double sided jet with a large opening angle in the beginning and a more complex



<http://arxiv.org/pdf/1302.1397v1.pdf>

**Figure 1.1.:** Illustration of the unification model of active galactic nuclei by Beckmann & Shrader (2012). The lower part of the image represents the model of a radio-quiet AGN, with the subclasses Seyfert 1 galaxies and Seyfert 2 galaxies, distinguished by the inclination angle (appearance of broad emission lines in the spectrum). The upper part shows the case of radio loud AGN (objects with prominent particle jet), on the right side the lower luminous objects and on the left side the objects with higher radio luminosity. The objects with low inclination angles are called blazars the objects with high inclination angles are radio galaxies.

plume-like structure in the outer regions, where the jet is destabilized and decelerated by the ambient medium. In this type the surface brightness decreases along the outer parts of the object.

FR2 radio galaxies show mostly only a one sided faint jet with a very small opening angle. The counter jet is not visible because of relativistic Doppler-boosting and deboosting, since the jet is more powerful than these of type 1 and thus highly relativistic. Both jet and counter-jet end in a bright hotspot surrounded by a lobe, which are visible on both sides. Because the jet terminates in the intergalactic medium and the plasma is decelerated rapidly, the emission is not boosted in this area and is appears on both sides with bright emission regions.

## Radiation processes in blazars

In active galactic nuclei several radiation processes are present, beginning with the thermal emission in the host galaxies by stars and clouds, the thermal emission caused by the accretion of mass in the central region around the black hole, which cover energies between optical and x-rays and the emission coming from the plasma jet which is the inverse Compton radiation of the high energetic particles of the plasma and the synchrotron emission caused by the acceleration of the charged plasma particles in the magnetic field of the source. For this study the radiation of interest is the synchrotron emission in the jets which should be summarized here following the description of [Rybicki & Lightman \(1979\)](#). In the second part also the special behavior and occurrence of the synchrotron spectrum of blazars is discussed.

Synchrotron radiation emerges if relativistic charged particles are accelerated in magnetic field. In the case of a single charged particle moving in a magnetic field in the vacuum the only force affecting the particle is the Lorentz force

$$\frac{d\vec{v}_\perp}{dt} = \frac{q}{cm\gamma} \vec{v}_\perp \times \vec{B}. \quad (1.1.3)$$

As seen in the equation only the velocity component  $vecv_\perp$  perpendicular to the magnetic field is effecting the Lorentz force. Assuming circular or a helical motion of the particle with respect to the magnetic field the emitted power of a single charged particle can be calculated according to Larmor's formula to

$$P = \frac{2q^2\gamma^4}{3c^2} (a_\perp^2 + \gamma^2 a_\parallel^2) = \frac{2q^4\gamma^2 B^2}{3c^5 m^2} v_\perp^2. \quad (1.1.4)$$

Because  $P \propto m^{-2}$  only particles with small masses give a high contribution to the total emitted synchrotron power. [Mannheim \(1993\)](#) also includes hadronic contributions, for this thesis however, pure leptonic models are considered. Because the theory of synchrotron radiation considers relativistic particles, the radiation is beamed in the direction of the velocity  $v_\perp$  in the shape of a cone. These cone has an opening angle of  $\theta = \frac{1}{\gamma}$ . As one can see in [Fig.1.4](#) the observer registered a doppler shifted radiation

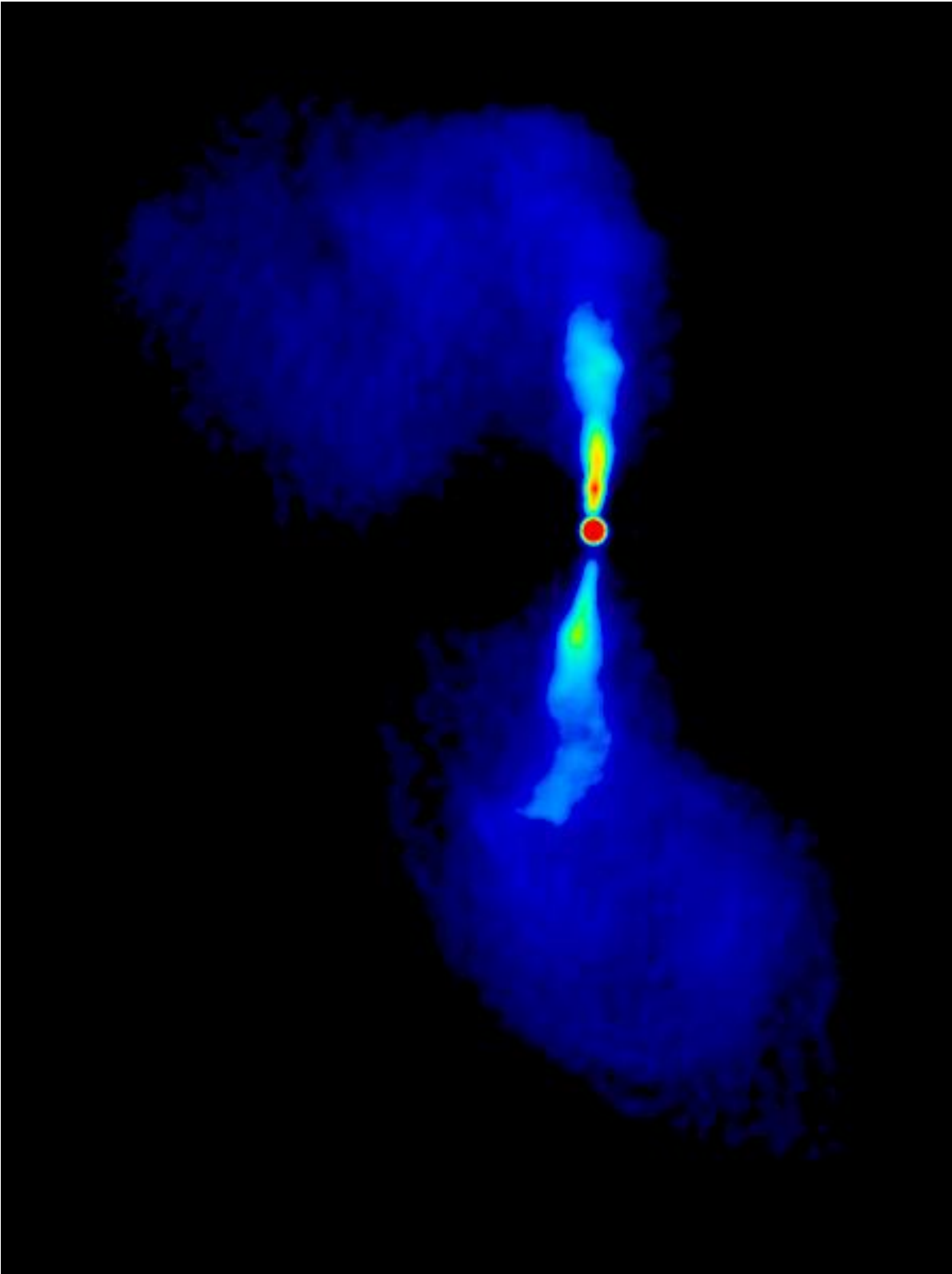


**Figure 1.2.:** The radio illustration of surface brightness distribution of 3C 272 observed at  $\nu = 5$  GHz with the VLA adapted Beckmann & Shrader (2012) shows the source on kiloparsec scales. The radio fluxdensity is color scaled with red, high fluxdensity, and blue, low fluxdensity. 3C 272 belongs to the more low luminous FR1 radio galaxies. <sup>7</sup> The morphology is dominated by a bright radio core. A two sided jet is visible with decreasing surface brightness going to the outer parts of the jets. In the outer parts more complex plumes are visible.

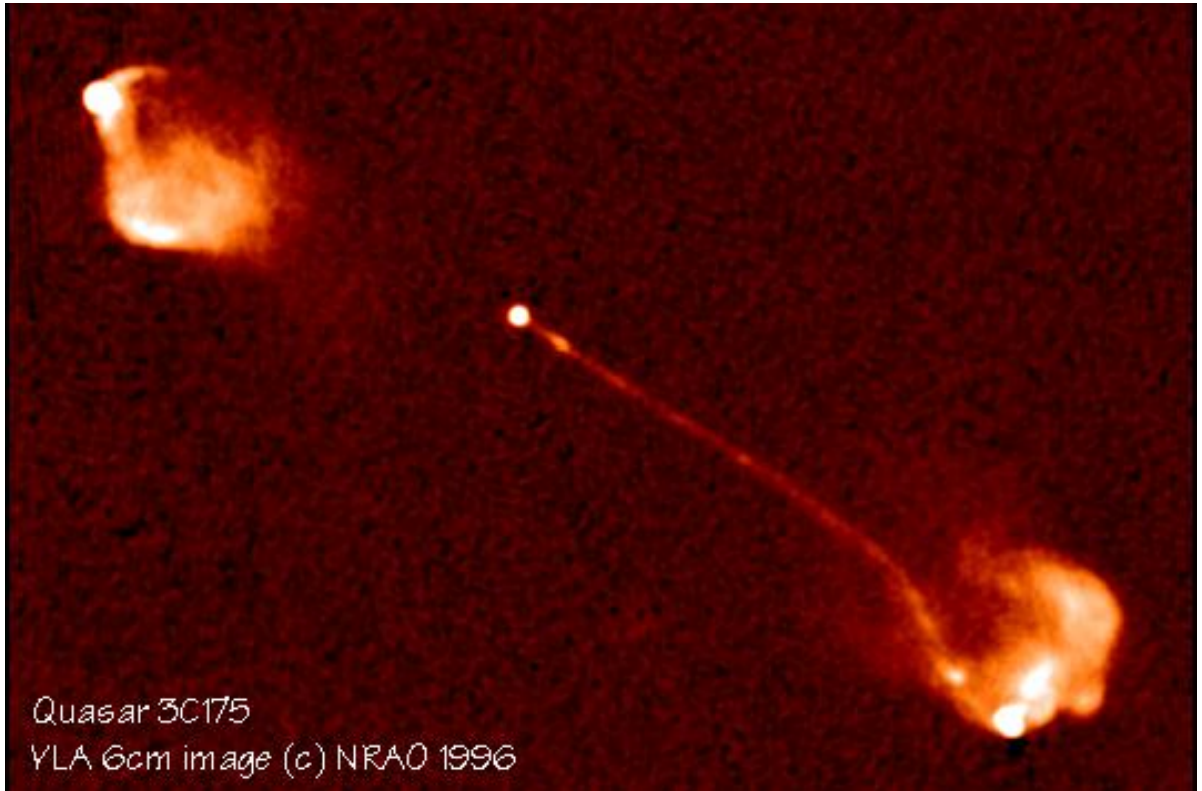


**Figure 1.3.:** The radio illustration of surface brightness distribution of 3C 175 observed at  $\nu = 5$  GHz with the VLA adapted from [Beckmann & Shrader \(2012\)](#) shows the source on kiloparsec scales. The radio fluxdensity is color scaled with white/bright red, high fluxdensity and black/dark red, low fluxdensity. 3C 175 belongs to the high luminous FR2 radio galaxies. The morphology of the source consists of a bright core in the middle, a faint jet in the S-W direction and two hotspots with lobes in S-W and N-E direction, where the jets terminate, because of deceleration by the intergalactic medium.

pulses with a length of  $\tau = \frac{1}{\gamma^2 \omega_L}$ . For this short pulse follows with respect to Heisenbergs uncertainty relation a broad band emission spectrum with a peak at the characteristic frequency of  $\omega_c = \frac{1}{\tau} = \gamma^2 \omega_L$ .

The whole jet of an AGN consists not only of a single particle but of a huge amount of such particles. Meaning not all of the particles move in the same direction and also feature different amounts of kinetic energies. So it is assumed that the velocity direction of the particles is distributed isotropic and the kinetic energies of the electrons are distributed according to a power law with  $n(\gamma) = n_0 \gamma^{-p}$  and with the approximation that all electrons emitting only with their characteristic frequency  $\nu_c = \frac{\omega_c}{2\pi}$ . With this assumptions the total emitted power of a bulk of electrons can be calculated to

$$P_\nu = \frac{2c\sigma_T n_0 U_B}{3\nu_L} \left( \frac{\nu}{\nu_L} \right)^{-\frac{p-1}{2}}. \quad (1.1.5)$$

Here  $\sigma_T = \frac{8\pi q^4}{3m^2 c^4}$  is the Thomson cross section,  $U_B = B^2/8\pi$  the magnetic field energy density and  $\nu_L$  the Larmor-frequency.  $\alpha = \frac{p-1}{2}$  is commonly known as spectral index. This spectral behavior calculated in equation 1.1.5 holds only for electron bulks which are optical thin and almost the whole emitted photons can escape the bulk. If a great amount of the considered radiation at a specific frequency is absorbed by the plasma of an emission region this area is called optical thick for this radiation. This process of absorption of produced synchrotron emission is also called synchrotron self-absorption. The optical thickness  $\tau_\nu$  can be calculated by knowing the absorption coefficient  $a_\nu$  and the travel distance  $d$  by:

$$\tau_\nu = \int_{d_0}^d a_\nu(s) ds. \quad (1.1.6)$$

For  $\tau_\nu > 1$  the medium is called optically thick and for  $\tau_\nu < 1$  optically thin. For the case of the optically thick part of the synchrotron radiation of one region the emitted power changes with an spectral index of  $\alpha = \frac{5}{2}$ , in the optically thin part of the spectrum  $\alpha$  is determined by the power law index  $p$  of the electron distribution as discussed before. So the turnover point of the spectrum is located at  $\tau_\nu = 1$ .

Observing blazars the spectrum of the emitted synchrotron radiation is effected byrelativistic effects and has changed from the intrinsic one to spectrum arriving at the observer. Because the plasma is moving towards the observers direction, the spectrum is blue shifted because of the Doppler effect. According to Cohen et al. (2007) also the observed luminosity changes, because of the moving plasma with

$$L = L_0 \delta^n, \quad (1.1.7)$$

where  $L_0$  is the intrinsic luminosity in the rest-frame of the jet the power law index  $n = \alpha + p$ , with the spectral index  $\alpha$  and the Doppler exponent  $p$ , and the Doppler factor

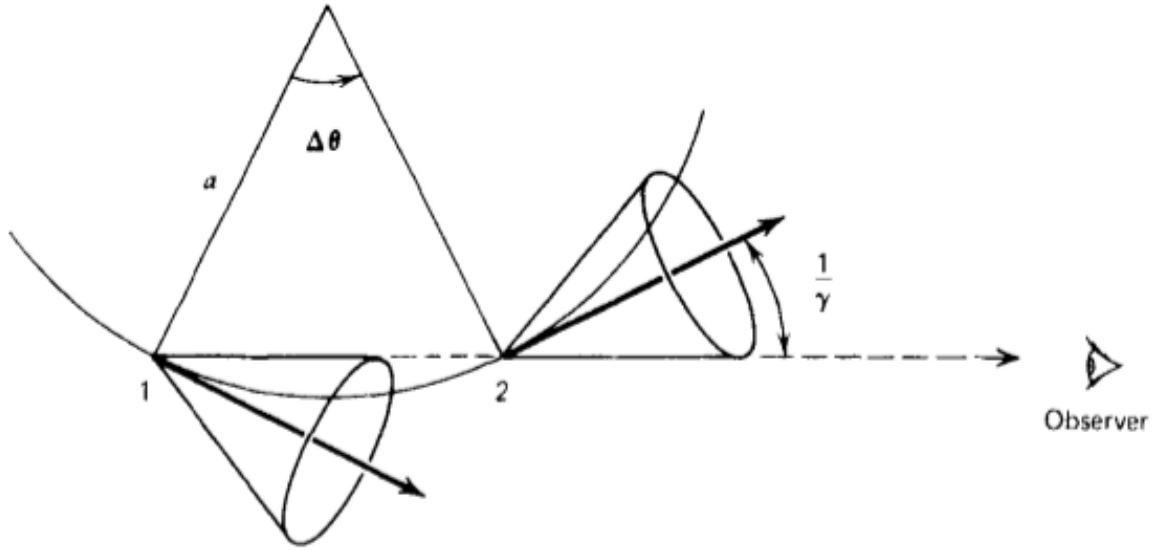


**Figure 1.4.:** Illustration of the beamed synchrotron radiation of a single electron with a relativistic circulation around a magnetic field. The radiation is emitted in a cone with opening angle  $\theta$ . Credits: [Rybicki & Lightman \(1979\)](#).

$$\delta = \gamma^{-1} (1 - \beta \cos \zeta)^{-1} \quad (1.1.8)$$

including the intrinsic Lorentz-factor  $\gamma$  and the intrinsic jet speed  $\beta$ . The difference between the unbeamed and beamed spectrum of one single emission region is shown in Fig.1.5. Because of this effect the luminosity of the jet is boosted and the luminosity of the counter-jet is deboosted, so the jet is brighter than the counter-jet, which is the reason for the counter-jet being invisible for balazars and most FR2s.

According to [Fanti et al. \(1995\)](#) the position of the maximum in a synchrotron spectrum, in which  $\tau_\nu = 1$ , is proportional to the size of the region. In the case of blazars as shown in Fig.1.6 the different regions overlay each other and the resulting spectrum is a superposition of the spectra of all emission regions, resulting in a flat spectrum. Only in the low frequency regime the spectrum can steepen, because in this area the extended not beamed emission prevail the beamed emission of the spectrum.

Because of the low inclination angles of blazars and the relativistic particle motion another geometric effect appears by observing single emission regions at parsec-scales. When tracking single emission regions over time, in some cases these regions appear to move superluminal. This effect is a projection effect and this apparent speed is connected with the intrinsic speed of the jet via the inclination angle  $\zeta$  according to the equation from [Cohen et al. \(2007\)](#):

$$\beta_{\text{app}} = \frac{\beta \sin \zeta}{1 - \beta \cos \zeta} \quad (1.1.9)$$

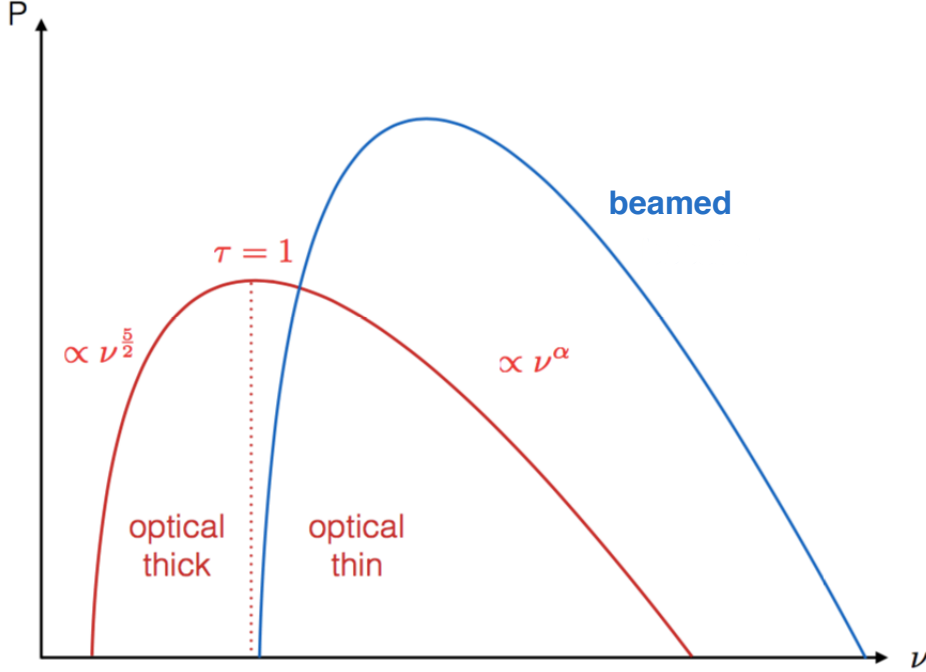


**Figure 1.5.:** Illustration of the difference of a beamed synchrotron emission spectrum (blue) and unbeamed synchrotron emission spectrum (red) of the same electron distribution with spectral index  $\alpha$ . By Burd (2017).

## Unification

With respect to the unification model, BL Lac object should be the beamed and rotated counterparts of FR1 radio galaxies and FSRQs should be the beamed and rotated counterparts of FR2 radio galaxies. Because the beamed emission is biased by the beaming effect the extended luminosities of radio galaxies and blazars can be studied. According to Kharb et al. (2010) and Fanaroff & Riley (1974) the extended luminosity at  $\nu = 1.4$  GHz of FR1 radio galaxies should be  $\log(\frac{L_{\text{ext}}}{\text{W/Hz}}) < 24.5$  and the luminosity of FR2 objects  $\log(\frac{L_{\text{ext}}}{\text{W/Hz}}) > 26$ , with a transient regime in between. The morphology of the two blazar type should be look like the rotated picture of their radio galaxy counterparts.

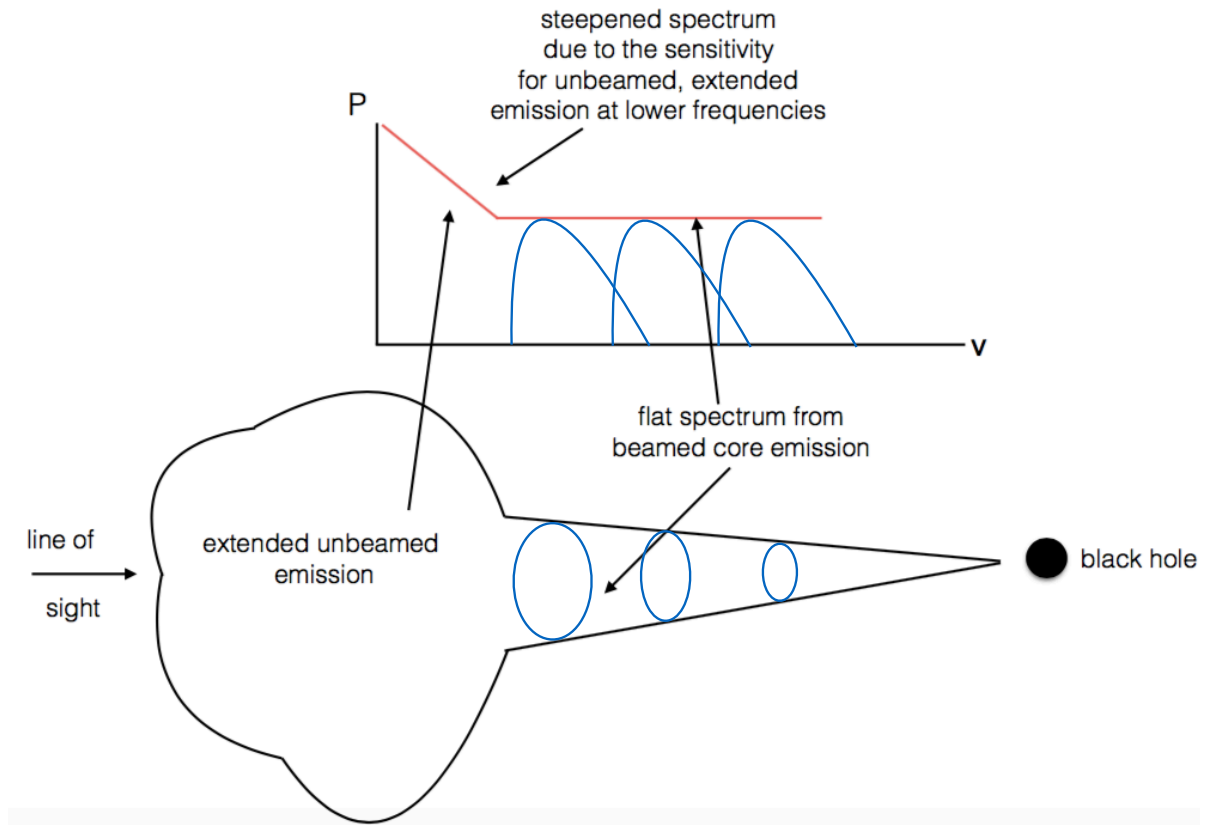


**Figure 1.6.:** Illustration of the composition of a blazar spectrum, consisting of a flat spectrum part caused by the beamed core emission and the steep part of the spectrum caused by the unbeamed extended emission of the source. The flat part of the spectrum is the result of the superposition of the beamed spectra of single emission regions of the jet, peaking at different frequencies. Adapted from [Burd \(2017\)](#).

## 1.2. Radioastronomy

As discussed in the sections before radio loud AGN on kpc-scales are considered for this study. The typical angular resolution required to study kpc-Mpc sized objects is in the arcsec regime..

According to [Burke & Graham-Smith \(2010\)](#) the first radio telescope was build in 1931 by Karl Guthe Jansky, which was not designed as radio-telescope but to identify radio noise disturbing radio telephones. This first telescope consists of an array of several dipole-antennas mounted on a turntable, so the detector was able to receive radiation from different positions in the sky. In this way Jansky discovered the radio emission of the Milky Way especially from the inner center of our galaxy. The first steerable parabolic antenna was build six years later by Grote Reber in Wheaton, Illinois, with a dish-diameter of 9 m.

### Radio-interferometry

With the largest steerable radio-telescopes like the Greenbank ([Prestage et al. \(2009\)](#)) and the Effelsberg ([Hachenberg et al. \(1973\)](#)) telescopes with a diameter of about 100 m, each, achieve only an angular resolution of about 9 arcmin at an observing frequency of 1.4 GHz, which is the main observation frequency in this study, can be achieved. as mentioned above, however, resolution in the order oof arcseconds are required, therefore several telescopes are combined to an interferometer, where the resolution is constrained by the largest distance between two antennas. These baselines can reach distances up to thousands of kilometers or in case of compact radio-arrays of several kilometers, according to which object or aspects of object should be observed. With use of compact arrays the required resolution for this study can be achieved.

To get a better understanding for the calibration and imaging processes in the following chapter, the method of radio-interferometry is explained on the basis of a two element interferometer. The explanations are based on [Burke & Graham-Smith \(2010\)](#), and [Thompson et al. \(2001\)](#), which give an overview on the topic mainly based on the mechanism in the telescopes and the correlator, and based on [Taylor et al. \(1999\)](#), which focuses on the coherence of the incoming electromagnetic wave.

An electromagnetic wave is composed of an electric-field component and a magnetic-field component which are perpendicular to each other and also both are orthonormal with respect to the direction of propagation. The electric-field is assumed to be caused by an harmonic oscillator on an position  $\vec{R}$  which produces a time-variable electric field  $\vec{E}_\nu(R, t)$  and propagates to a new location  $\vec{r}$ . According to Maxwell's equations this electric field causes also a magnetic field perpendicular to it. For simplicity only the procedure of the electric field is discussed here, because the behavior of the magnetic field is almost the same.

The propagation of the electric field to its new position can be described by the propa-

gator  $P(\vec{R}, \vec{r})$  by

$$\vec{E}_\nu(\vec{r}) = \int \int \int P_\nu(\vec{R}, \vec{r}) \vec{E}_\nu(\vec{R}) dx dy dz. \quad (1.2.1)$$

In the procedure explained in the following section some simplifications are made, which should be summarized at first. The first one is to treat the electric field not as a vector field but as a scalar field, meaning only a transverse wave with no polarization is considered. The second assumption is that the radiating object is far away from the observer and so a two dimensional description is sufficient. For this purpose  $\vec{R}$  points not to the object but to a projection of the electric field  $\mathcal{E}_\nu(\vec{R})$  on a sphere with radius  $|\vec{R}|$  someway between the object and the observer. In the third simplification it is assumed that the space between the two locations are empty and now the propagator can be written according to Huygens principle

$$P_\nu(\vec{R}, \vec{r}) = \frac{\exp\left(i2\pi\nu |\vec{R} - \vec{r}|\right)}{|\vec{R} - \vec{r}|}. \quad (1.2.2)$$

These first three assumptions effect especially the propagation of the electric field. The last simplification belongs to the coherence of two electromagnetic waves, meaning that only the radiation from the same position can be coherent, but in every other case the radiation is not spatially coherent. As a consequence the following relation holds for the expectation-value of two electric fields:

$$\langle \mathcal{E}_\nu(\vec{R}_1) \mathcal{E}_\nu^*(\vec{R}_2) \rangle = 0 \quad \forall \vec{R}_1 \neq \vec{R}_2 \quad (1.2.3)$$

With this simplification the electric field of a single propagating wave starting at  $\vec{R}$  and observed at  $\vec{r}$  can be written as the following equation:

$$E_\nu(\vec{r}) = \int \mathcal{E}_{nu}(\vec{R}) \frac{\exp\left(i2\pi\nu |\vec{R} - \vec{r}|\right)}{|\vec{R} - \vec{r}|} dS. \quad (1.2.4)$$

The integration has now changed from a three dimensional to a two dimensional integration over the sphere surface  $S$ .

To characterize the inteference of two waves coming from the same position  $\vec{R}$ , which are observed at positions  $\vec{r}_1$  and  $\vec{r}_2$ , the coherence-function must calculates as

$$V_\nu(\vec{r}_1, \vec{r}_2) = \langle E_\nu(\vec{r}_1) E_\nu^*(\vec{r}_2) \rangle = \int I_\nu(\vec{s}) \exp(-i2\pi\nu \vec{s} \cdot (\vec{r}_1 - \vec{r}_2) / c) d\Omega. \quad (1.2.5)$$

Here  $\vec{s} = \frac{\vec{R}}{|\vec{R}|}$  indicates the unit-vector in  $\vec{R}$ -direction and  $I_\nu(\vec{s}) = \langle \mathcal{E}_\nu(\vec{s}) \mathcal{E}_\nu^*(\vec{s}) \rangle$  is the intensity. Because of the introduction of the sphere according the second simplification, the integration variable is the solid angle  $\Omega$ .

This coherence function must be measured to reconstruct a brightness-distribution from the object the electromagnetic waves came from. To do this, radio interferometers are used. This kind of telescope can not observe at a specific frequency but at a finite bandwidth and not the entire celestial plain can be gathered with the telescopes, so only parts of are sampled. For simplicity it is assumed, that the single antennas of the array are placed coplanar, so that the difference between the two electric fields can be expressed by the space between two telescopes, meaning the baseline of the two antennas usually expressed by amounts of the observation wavelength  $\vec{b}_\lambda = \vec{r}_1 - \vec{r}_2$ . It is also assumed that the radiation only comes from a small area on the sky plain, so that the pointing vector can be written by  $\vec{s} = \vec{s}_0 + \vec{\sigma}$  as shown in figure 1.8. Because  $\vec{\sigma}$  is very small  $\vec{s}$  can be assumed to be parallel to  $\vec{s}_0$ . With this assumption the baseline-vector is also perpendicular to  $\vec{s}_0$  and the coherence function can be written as

$$V_\nu(\vec{b}_\lambda) = \int I_\nu(\vec{\sigma}) \exp(-i2\pi\vec{\sigma} \cdot \vec{b}_\lambda) d\Omega. \quad (1.2.6)$$

The baseline vector is usually given in the orthogonal (u,v,w)-coordinate system as shown in Fig.1.8, also known as spacial frequencies measured in terms of the wavelength. Because the telescopes are assumed to be arranged in a plain it is assumed that  $w = 0$ . The vector  $\vec{\sigma}$ , which points from the phase center to the emission region in the sky-plain can be expressed with the direction cosines of  $\vec{s}$ :  $l, m, n$ . So equation 1.2.6 can be written as

$$V_\nu(u, v) = \int \int I_\nu(l, m) \exp(-i2\pi(ul + vm)) dl dm. \quad (1.2.7)$$

The problem arises, explained before, that the array consists of only a small amount of antennas and not the whole u,v-plain can be covered by the telescopes. So a sample-function  $S_\nu(u, v)$  must be defined. This function is zero, where the u,v-plain is not covered by antenna baselines. The Fourier-transform of this sampling function is the point spread function or also known as the synthesized beam of the array, which is also a quantity to calculate the angular resolution of the array:

$$B_\nu(l, m) = \int \int S_\nu(u, v) \exp(-i2\pi(ul + vm)) du dv. \quad (1.2.8)$$

So by knowing this function, a first so called dirty image can be calculated by the convolution with the sky brightness distribution. Besides the (u,v)-coverage also the shape and the bandwidth of the single telescopes must be taken into account. With the function  $\mathcal{A}_\nu(l, m)$ , the effective area of the telescope, including refraction effects of the telescopes are taken into account, meaning how the telescope detects radiation incoming

from several directions. This assumption leading to the so called complex visibility function:

$$V_\nu(u, v) = \iint \mathcal{A}_\nu(l, m) I_\nu(l, m) \exp(-i2\pi(ul + vm)) dl dm. \quad (1.2.9)$$

This function is measured for every baseline pair by correlating every voltage signal of one antenna with every other as shown in Fig.1.7, technical delay  $\tau_t$  is chosen to be the same as the geometrical  $\tau_g$  one, that only interference pattern near the phase center is registered. To get a better (u,v)-coverage, the antennas are spread over an area for example as Y-formation and because of long observation times the coverage is also better by taking the earth rotation into account.

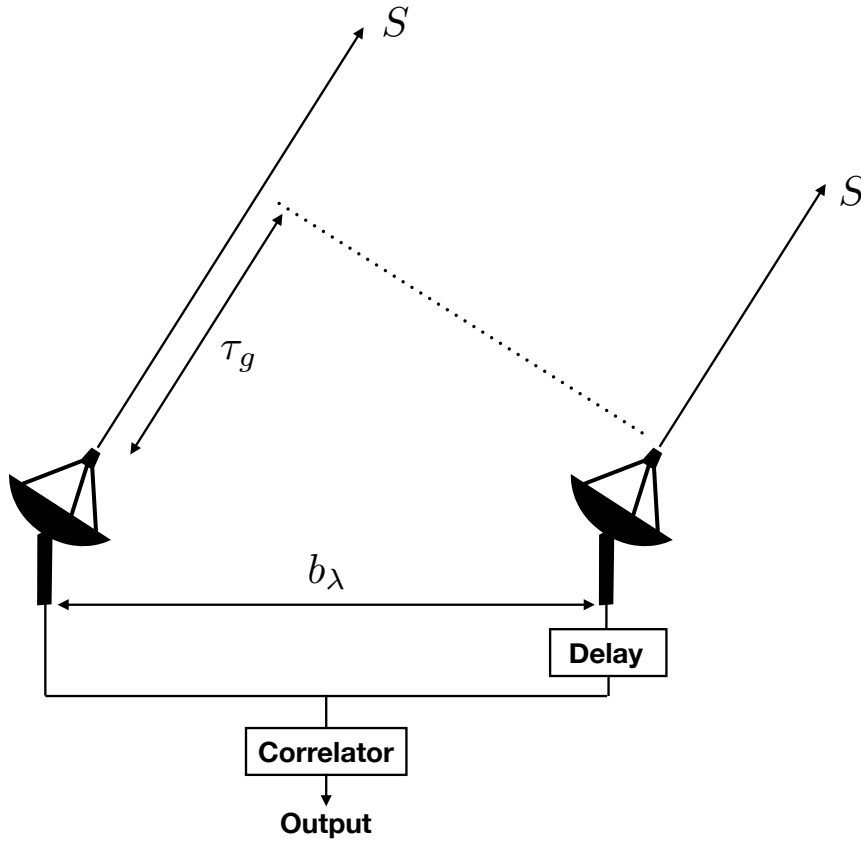


**Figure 1.7.:** Scheme of a two element interferometer, with two single-dish telescopes pointing in the direction of  $S$  with baseline  $b_\lambda$  and geometrical time-delay  $\tau_g$  between the two telescopes. Also an instrumental delay and the correlator is shown.

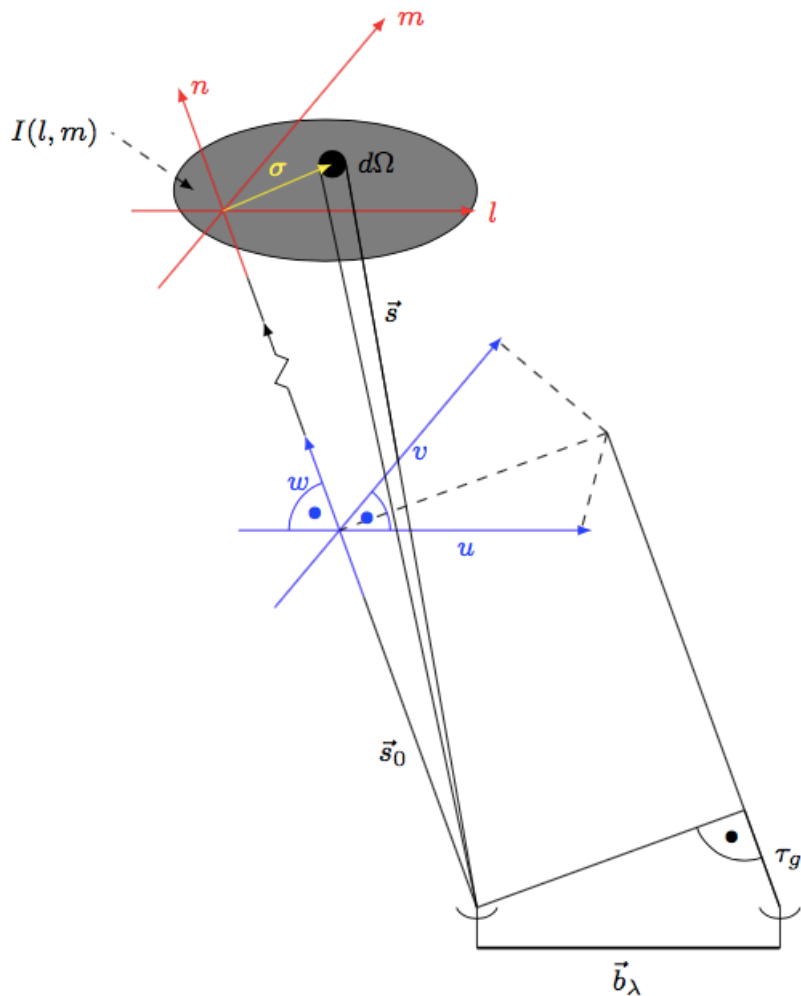


**Figure 1.8.:** Sketch of the different coordinate-systems used to explain radio interferometry of two antennas with spacing of one baseline  $b_\lambda$ . The radiation arrives at the right antenna with a geometrical delay of  $\tau_g$  according to the left reference antenna. The grey emission area from which the radiation of the object comes from is given in coordinates  $l, m, n$  and the baselines of the array is represented by the  $u, v, w$  coordinated. Figure by Burd (2017).

## Important radio arrays

In this study data of mainly three radio arrays are used. Because the arrays differ in construction, technical features and area of application, an overview of every used telescope is given.

### Very Large Array

The main part of this study makes use of archive data of the Karl Guthe Jansky very large array former known as **Very Large Array** (VLA). The array is located in the desert of New Mexico, United States of America and belongs to the national radio astronomy observatory (NRAO). As described by [Thompson et al. \(1980\)](#) the array started its operation in 1980. The array consist of 27 identical constructed single dish radio telescopes with a diameter of 25 m each. The telescopes are arranged in a Y-shaped form. Each telescope is mounted on a wheeled platform, such that each antenna can be moved in and outward on the rails along the Y-shaped arms, as it is shown in [Fig.1.9](#). Because of the movability of each antenna, the VLA posses four main configurations A,B,C and D, with maximal baselines from 1 km (D-configuration) to 36 km (A-configuration). The configuration change within a cycle of about 1.5 years. In a small time range between two main configuration also observations with transitional configurations, where some of the telescope are still in the first configuration and some already in the second configuration, take place. The array can observe at different frequency bands in the radio spectrum. Because the detectors for the single frequency bands have changed over the time also the frequency range changed. The largest modification was done between 2001 and 2012 ([Perley et al. \(2011\)](#)), where the great amount of detectors and the correlator and computation system were modernized and also the data processing was shifted from a 'aips-friendly' to a 'casa-friendly' data structure. After the changes the array was renamed to Karl G. Jansky Very Large Array respectively the short form of the name changed from VLA (before 2012) to EVLA (beginning at 2012). Now the frequency ranges between 1 GHz and 50 GHz, with maximal resolutions between 1.4 arcsec and 40 mas. To get a better idea of the change of the detector system and therefore for the coverage of frequency within the time of operation, in [Tab.1.1](#) the different detectors are shown with their frequency band and range, their resolution at the different telescope configuration and the time period of use in the telescope. The old telescope configuration was able to observe at two different observation modes with a maximal bandwidth of 50 MHz the continuum and the spectral line mode at all four stokes parameter. When the continuum mode was used, the signal over the whole bandwidth was correlated, when the spectral line mode was used, the whole bandwidth was subdivided in up to 256 frequency channels and these channels are correlated separately. With respect to [Perley et al. \(2011\)](#) the new EVLA configuration is able to observe with a maximal bandwidth of 8 GHz for each polarization with up to 16384 channels.



**Figure 1.9.:** Image of the whole VLA at D-configuration with maximal baselines of 1.03km. *Credits: Image courtesy of NRAO/AUI*

**Table 1.1.:** VLA-bands with their frequency-range, the time of operation and the angular resolution for the four main configurations A-D.

band	frequency range [GHz]	$\theta_A$ [arcsec] <sup>3</sup>	$\theta_B$ [arcsec] <sup>4</sup>	$\theta_C$ [arcsec] <sup>5</sup>	$\theta_D$ [arcsec] <sup>6</sup>	operation time
L <sup>1</sup>	1.0-2.0	1.3	4.3	14	46	1980-
S <sup>1</sup>	2.0-4.0	0.65	2.1	7.0	23	1980-
C <sup>1</sup>	4.0-8.0	0.33	1.0	3.5	12	1980-
X <sup>1</sup>	8.0-12.0	0.20	0.60	2.1	7.2	1980-
Ku <sup>1</sup>	12.0-18.0	0.13	0.42	1.4	4.6	1980-
K <sup>1</sup>	18.0-26.5	0.089	0.28	0.95	3.1	1980-
Ka <sup>2</sup>	26.5-40.0	0.059	0.19	0.63	2.1	2012-
Q <sup>2</sup>	40.0-50.0	0.043	0.14	0.47	1.5	2012-

<sup>1</sup> [Thompson et al. \(1980\)](#);    <sup>2</sup> [Perley et al. \(2011\)](#);

<sup>3</sup> Angular resolution VLA configurations A at the middle frequency of the range;

<sup>4</sup> Angular resolution VLA configurations B at the middle frequency of the range;

<sup>5</sup> Angular resolution VLA configurations C at the middle frequency of the range;

<sup>6</sup> Angular resolution VLA configurations D at the middle frequency of the range;

### Australia Telescope Compact Array

The **Australia Telescope Compact Array** (ATCA) is a compact radio array at the Paul Wild Observatory near the city of Narrabri in New South Wales, Australia, and belongs to the Australia Telescope National Facility. With respect to [Frater et al. \(1992\)](#) it consists of six 22 m single dish antennas. Five of the antennas can be moved on a one-dimensional 3 km long rail on the east-west direction with an accuracy of 35 mm. The sixth dish is located 3 km westwards of the end of the rail and can be moved on a 75 m long track with an accuracy of 2 mm. In this configuration the maximal baselines of this array is 6 km. Because of the one dimensional shape the resolution in north-south direction is not as good as in east-west direction. The antennas includes 11 detectors to cover a frequency range between 100 MHz and 116 GHz. According to [Wilson et al. \(2011\)](#) the bandwidth varies between 0.5 MHz and 256 MHz in the old configuration before 2011 and up to 2048 MHz in the new detector-configuration. For the high frequencies above 40 GHz only the inner 15 m of the dishes are suitable to detect this radiation, because the outer parts are not solid and are vaporized to rough to detect this radiation. The maximal resolution with the largest baseline of 6 km ranges from 2 arcmin at 100 MHz and 0.2 arcsec at 50 GHz. For the highest frequency band of up to 116 GHz (W-band) only smaller configurations are possible and the angular resolution is of about 2 arcsec.

### TANAMI

The TANAMI (**T**racking **A**ctive galactic **N**uclei with **A**ustral **M**illiarcsecond **I**nterferometry)-program is a VLBI-observation program, which monitors active galactic nuclei at the southern hemisphere at 8.4 GHz and 22 GHz. The single telescopes are not designed for VLBI like the Very Large Baseline Array (VLBA) on the northern hemisphere, operated by different organizations and are scattered over the entire southern hemisphere, as shown in [Fig.1.10](#) and [Tab.1.2](#), also including ATCA. The telescopes differ in size and frequency range, but all antennas include a 8.4 GHz and a 22 GHz receiver. In [table 1.2](#) the telescopes are listed with their diameters and positions. The maximal baselines are up to several thousands kilometer and so the typical angular resolution is of about 1 mas. The TANAMI-sample includes AGN with an declination below  $-30^\circ$ , radio flux over 2 Jy at 5 GHz from the catalog of [Stickel et al. \(1994\)](#) and a flat radio spectrum between 2.7 GHz and 5 GHz. 43 AGN from [Ojha et al. \(2010\)](#) and 39 AGN from [Müller et al. \(2017\)](#) are actual published.

**Table 1.2.:** Every actual radio telescope of the TANAMI project is listed with its name, the diameter and the location of the antenna.

name	diameter [m]	location
ATCA <sup>1</sup>	$5 \times 22$	Narrabri, New South Wales, Australia
Ceduna <sup>1</sup>	30	Ceduna, South Australia, Australia
Hartebeesthoek <sup>2</sup>	26	Hartebeesthoek, South Africa
Hobart (Mt. Pleasant Antenna) <sup>1</sup>	26	Hobart, Tasmania, Australia
Mopra <sup>1</sup>	22	Coonabarabran, New South Wales, Australia
O'Higgins <sup>3</sup>	9	O'Higgins, Antarctica
Parkes <sup>1</sup>	64	Parkes, New South Wales, Australia
Tidbinbilla (DSS43) <sup>4</sup>	70	Tidbinbilla, Australian Capital Territory, Australia
Tidbinbilla (DSS35) <sup>4</sup>	34	Australian Capital Territory, Australia
TIGO <sup>3</sup>	6	Concepcion, Chile

<sup>1</sup> operated by Commonwealth Scientific and Industrial Research Organisation (Australia);

<sup>2</sup> operated by National Research Foundation (South Africa);

<sup>3</sup> operated by Bundesamt für Geodäsie (Germany);

<sup>4</sup> operated by Canberra Deep Space Communication Complex (Australia);

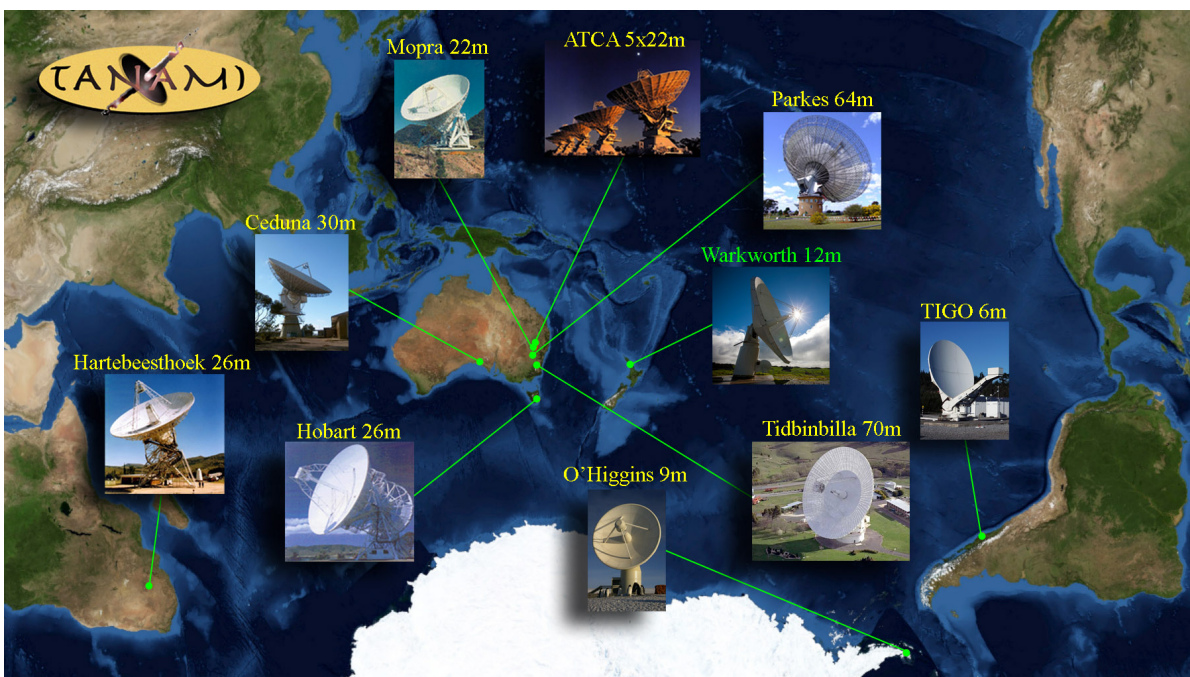


**Figure 1.10.:** Illustration of the locations of the different telescopes and subarrays of the TANAMI-project. *Credits by M. Kadler and J. Wilms*



## 2. Analyzing blazars on kpc-scales

### 2.1. Data-processing

All data, which is presented in this study, is raw data from the VLA- and ATCA-archive, meaning the data provided by the archives is correlated already, but no basic calibration and imaging is done so far. In the following the basic calibration and imaging processes are explained, which are used for the radio data in this study.

#### 2.1.1. Basic calibration

At the beginning the calibration is explained and at the end also some deviations calibrating different kinds of VLA-data and ATCA-data. The considered radio arrays observe objects at a well defined frequency and bandwidth over time. The signal traverse a bandpass-filter and is sampled in several frequency channels. The telescope measures at each channel and polarization an amplitude, which is proportional to the fluxdensity, and the phase of visibilities. Because the antennas itself only measure voltages which proportional to the fluxdensity but not the fluxdensity itself. In the case of extended sources with unknown structure also the absolute phase can not be measured. So the amplitudes and phases must be calibrated in some way. The flux calibration is done by observing additional to the target source a radio source with a known and almost not variable fluxdensity and also the distribution of the fluxdensity in the source must be known; for the simplest case the calibrator object should be an unresolved point-source. Also the phases must be calibrated by observing a nearby point-like calibrator source. Because the phases change a lot when the telescope looks at different angles through the atmosphere the telescope switches during the observation frequently between the target-source and the phase-calibrator. The phase-calibrator should be point-like, because then it could be assumed that the arriving wave-fronts are almost coherent. At last step also the bandpass for the several channels must be calibrated with a source, for which spectral behavior for the bandwidth is familiar.

### General calibration in AIPS

In the common case each fluxdensity, phase and bandpass must be calibrated. In this stude the software package AIPS<sup>1</sup> is used. To perform a first fluxdensity and phase calibration one channel, which is not polluted due to radio frequency interference (RFI), is split from the rest of the bandwidth. With SETJY the fluxdensity of the flux-calibrator is calculated by the model of Perley & Butler (2013) according to the observed frequency and the known spectral index of the source. In the next step the fluxdensity-distribution respectively the visibilities of the flux-calibrator must be adjusted by a theoretical model. In the most cases the calibrator sources are point-like, so a point-source model is fitted along the data of the calibrator with the task 'CALIB'. The model is saved in a solution-table and after this the also the visibilities of the phase calibrator is modeled with a point source and is saved ether in a different table . To adjust the fluxscale of the phase calibrator the model of the flux calibrator is applied on the source. To complete the calibration of the single channel the two solution tables are merged to a calibration table. To get all channels to almost the same level the bandpass must be calibrated. Before the calibration the bandpass shape is determined by the bandpass used in the receiver of the single telescopes and has in the simplest approximation a rectangular shape with variations in the plateau regime. To calibrate the bandpass a bright stable source with known spectral index is used, in most cases the flux calibrator and the bandpass shape is fitted with a polynomial function with the task 'BPASS'. The solution is saved in a bandpass table. Now the bandpass solutions are applied on all channels. In the ideal case the bandpass shape is now flat. Both the bandpass and calibration solutions are applied on the target source. In the last step the visibility data is averaged over all channels and is now prepared for the imaging process.

### Calibration of VLA-data

VLA-observations can be done in mainly two different ways. The first one is to observe one object in the so called continuum-mode. In the continuum mode the whole bandwidth is treated as one big frequency channel and is not split in several single channels as explained before. So the whole bandwidth is correlated as once. So when calibrating these kind of datasets no bandpass calibration must be done because only one channel is available. The second kind of observation is the spectral-line-mode. In case of this observation method the whole bandwidth is split in several channels, which are correlated separably. But for flux and phase calibration also a 'channel 0' is available, which was averaged over the inner two thirds of the channels and correlated separably. In this case the so called 'channel 0' is used as channel for flux and phase calibration like explaint in the section before. The other steps in the calibration process do not differ from the common process.

---

<sup>1</sup>Astronomical Imaging Processing System (AIPS): <http://www.aips.nrao.edu>

## Flagging

Sometimes the delivered data is corrupted in different ways. One cause of corruption can be that some channels of the observed bandwidth is polluted RFI meaning, that some nearby man-made object emits at the respective channel frequency. Also the correlator can yield problems at certain timesteps, yielding sudden drops of the signal to zero amplitudes. Also there can appear perturbations in the correlation process, where at some time-periods the data of all baselines are corrupted and show the same features as the letter ones. These data-points can be flagged, so that these data-points are not recognized for the next steps in the calibration process.

### 2.1.2. Hybrid-imaging

After the basic calibration process the single source data is ready to be reduced in this way to get a map of the fluxdensity-distribution in the end of a so called 'imaging'-process. To explain the imaging process with the difference-mapping program difmap, which is used for this study some theoretical background is presented for a better understanding of the imaging process by itself.

#### The clean algorithm

The CLEAN algorithm introduced by Högbom (1974) and mathematical described by Schwarz (1978) is an iterative process, which improves the reconstruction of radio-interferometry data. The description of the CLEAN-algorithm will be orientated mainly on the work of Högbom (1974). As explained in chapter 1.2 the radio-interferometer-data is taken by correlating data of different radio telescopes. The so created interference-pattern respectively the observed visibilities are the convolution of the brightness-distribution of the observed object on the sky with the characteristics of the array configuration. Because the  $u,v$ -plain is not covered continuous but sampled because of several non regular distributed baselines and time-increments, the reconstruction of the brightness-distribution of the source via a simple deconvolution is difficult and in most cases the resulting maps are polluted because of several sidelobes of the telescope array.

The first principal is that the Fourier-transformation of the measured visibilities  $W(u, v)$  times a weighting-function is proportional to the convolution of the real brightness  $B(l, m)$  on the sky multiplied by the primery beam  $P(l, m)$  of the telescope-configuration with the synthesized beam  $G(l, m)$ , which is shown in the following equation:

$$(P(l, m) \cdot B(l, m)) * G(l, m) \propto \int_{-\infty}^{\infty} \int_{-\infty}^{\infty} W(u, v) \cdot g(u, v) e^{i2\pi(lu+mv)} du dv \quad (2.1.1)$$

The synthesized beam is given by the normalized Fourier-transformation of the weight-

function as follows:

$$G(l, m) = C \int_{-\infty}^{\infty} \int_{-\infty}^{\infty} g(u, v) e^{i2\pi(lu+mv)} du dv \quad (2.1.2)$$

Here is C is a constant, calculated through normalization. When the u,v-plane is not covered regularly the weight-function on the not sampled positions must be set to zero and so the weight-function is a step-function with most steps are zero in a very irregular way. So the Fourier-transform of this is a synthesized beam with a main-beam and a pattern of a lot of sidelobes, which are difficult to handle. So if a map is calculated according to the Fourier-transform of equation 2.1.1 the map is also polluted by the dominated sidelobes of the beam and the map is almost useless. The in this way obtained map is also called the 'dirty-map' (DM) and the beam 'dirty-beam' (DB). If the DM is calculated with the weight-function of 1 for all visibilities it is also called the principal solution.

So the DB and DM can be written symbolic as the following:

$$g \xrightarrow{FT} DB \quad (2.1.3)$$

$$W \cdot g \xrightarrow{FT} DM \quad (2.1.4)$$

If it can be assumed that the real brightness-distribution on the sky is composed of several point-sources now the DM can be used to find these point-sources on the position in the DM of highest flux and than a DB with main-lobe on the position of highest flux and same amplitude can be saved and subtracted from the map. In the case of only one point-source in the field of view this source can then be represented by a Gaussian point-source-model with the same full-width-half-maximum as the primary maximum of the DB. But in most cases the whole map contains several point-sources and the maximum in the DM can also be created by the superposition of several sidelobes, so to find the 'real' first maximum of the point-source with highest amplitude the correlation-function between DM and DB meaning the convolution of these two parameter must be considered:

$$W \cdot g^2 \xrightarrow{FT} DM * DB \quad (2.1.5)$$

In the simplest case of the principle-solution the weighting-function is equal unity in the case of sampled uv-data and zero in the case of the unsampled baselines meaning the DM is equal to the convolution of DM and DB and only the DM must be considered. But with  $g \neq 1$  still the following relation is true

$$DM = DM' * DB' \quad (2.1.6)$$

Here the dash indicates dirty map and beam, which would be calculated with weight-function  $g' = \sqrt{g}$ . And so the computation can be treated in a similar way. So to reconstruct a brightness distribution the following process can be used. In step I) DM and DB are calculated according to equations 2.1.1 and 2.1.2. At step II) on the position of the maximum with a amplitude  $I_0$  on the DM the DB is subtracted with the amplitude of the maximum times a loop-gain-factor  $\gamma$  ( $\gamma I_0$ ). Then in step II) step II) is repeated with the values for  $I_0$  and DM of at the end of the previous iteration-step as long as the calculated maximum is about the same level than the noise of the DM. After this iterative process in step IV) all considered maxima of the step III) before are returned together with their loop gain factors to the last map in the shape of the clean beam (CB) resulting in the so called 'clean-map' (CM). So after the last step the map is reconstructed as a superposition of point-sources and the remaining noise and also the most parts of image relics should be vanished.

### Self-calibration

In the imaging process it is possible to calibrate the data based on a established model, which could done before by the CLEAN-algorithm. For this process the so called closure-phases and fringe-amplitudes are used to calibrate the phases and amplitudes and their related errors. To explain the closure-relations it is important to explain the idea of the complex visibilities. The complex visibilities are created for each baseline by correlating the signals of the two considered antennas. The true visibilities  $V_{ij}^{\text{true}}$  for one baseline, meaning for a possible ideal antenna pair with no errors to be recognized, is composed like this:

$$V_{ij}^{\text{true}} = A_{ij}e^{i\varphi_{ij}} \quad (2.1.7)$$

Here  $A_{ij}$  indicate the amplitude and  $\varphi_{ij}$  the phase. In the observation of a source the complex visibilities are sample over increments of time, so the amplitudes and phases are also functions of time. For simplicity this time dependencies are not shown in the equations here. The real observed complex visibilities depend besides the true visibilities also on some gain and phase errors introduced by the considered antennas itself and the correlation-process. The calculation of the real observed visibilities is shown in equation 2.1.8 :

$$\begin{aligned} V_{ij}^{\text{obs}} &= g_i g_j^* G_{ij} V_{ij}^{\text{true}} \\ &= a_i a_j G_{ij} e^{i(\delta_i - \delta_j)} A_{ij} e^{i\varphi_{ij}} \\ &= a_i a_j G_{ij} A_{ij} e^{i(\varphi_{ij} + \delta_i - \delta_j)} \end{aligned} \quad (2.1.8)$$

Here  $g_i$  and  $g_j$  are the complex gain errors caused by the single telescopes. This two functions consists itself of the two amplitude errors  $a_i$  and  $a_j$  and the phase errors  $\delta_i$

and  $\delta_j$ .  $G_{ij}$  is a gain-factor introduced by the correlation of the two telescopes.

**Closure-phases** In the phase measurement  $\phi_A$  the real-phase  $\varphi_A$  of an antenna is polluted by an phase-shift  $\delta_A$ , which is caused by technical effects in the detector of the antenna. This error is different in every telescope of the array. In the same way also the correlated measured phase  $\phi_{AB}$  of the baseline of two telescopes A and B is composed of the a real phase  $\varphi_{AB}$  and the errors of the two considered antennas  $\delta_A$  and  $\delta_B$ :

$$\phi_{AB} = \varphi_A - \varphi_B + \delta_A - \delta_B = \varphi_{AB} + \delta_A - \delta_B \quad (2.1.9)$$

To get over this single telescope errors, according to [Jennison \(1958\)](#) the phases of three baselines of three telescopes can be summed as shown in figure 2.1. The single phases of the three baselines can be read in the following:

$$\phi_{AB} = \varphi_{AB} + \delta_A - \delta_B \quad (2.1.10)$$

$$\phi_{BC} = \varphi_{BC} + \delta_B - \delta_C \quad (2.1.11)$$

$$\phi_{CA} = \varphi_{CA} + \delta_C - \delta_A \quad (2.1.12)$$

The sum of the three phases is called closure-phase of these three antennas:

$$\begin{aligned} \theta_{ABC} &= \phi_{AB} + \phi_{BC} + \phi_{CA} \\ &= \varphi_{AB} + \delta_A - \delta_B + \varphi_{BC} + \delta_B - \delta_C + \varphi_{CA} + \delta_C - \delta_A \\ &= \varphi_{AB} + \varphi_{BC} + \varphi_{CA} \end{aligned} \quad (2.1.13)$$

In equation 2.1.13 for the closure-phases only the real-fringe-phases are included and the specific errors for the single telescopes are gone. So the closure-phases of several antennas are conserved quantities. With the help of these closure-phases and an established CLEAN-model the phases of all visibilities and their errors can be changed in this way that the closure-phases are conserved and the phases are in the end more aligned on the established model ([Jennison \(1958\)](#)). This procedure is also called phase-self-calibration.

**Closure-amplitudes** There is a similar procedure for the visibility-amplitudes to calculate a conserved quantity to do self-calibration also for amplitudes. The closure amplitude  $A_{ijkl}$  is a conserved quantity of a circle of not three but four baselines. In the following computation according to [Jennison \(1958\)](#) it is shown that also the closure amplitude is a conserved quantity:

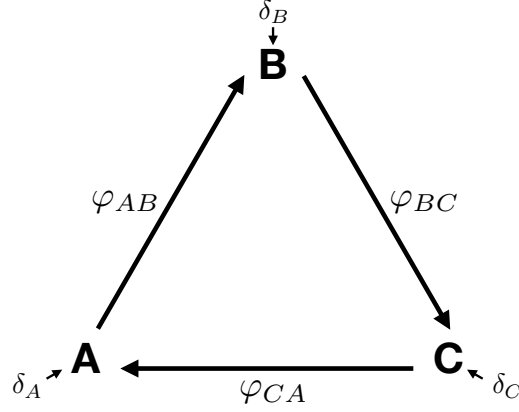


**Figure 2.1.:** Illustration for the explanation of the closure phases. A, B, C represent three telescopes of the considered array, the arrows the signal flux between the antennas.  $\varphi_{AB}$ ,  $\varphi_{BC}$  and  $\varphi_{CA}$  are the phases of two considered telescopes.  $\delta_A$ ,  $\delta_B$  and  $\delta_C$  represent the errors introduced by every single telescope.

$$\begin{aligned}
 A_{ijkl} &= \frac{A_{ij}^{\text{obs}} A_{kl}^{\text{obs}}}{A_{ik}^{\text{obs}} A_{jl}^{\text{obs}}} \\
 &= \frac{a_i a_j G_{ij} A_{ij}^{\text{true}} a_k a_l G_{kl} A_{kl}^{\text{true}}}{a_i a_k G_{ik} A_{ik}^{\text{true}} a_j a_l G_{jl} A_{jl}^{\text{true}}} \\
 &= \frac{A_{ij}^{\text{true}} A_{kl}^{\text{true}} G_{ij} G_{kl}}{A_{ik}^{\text{true}} A_{jl}^{\text{true}} G_{ik} G_{jl}} \\
 &= \frac{A_{ij}^{\text{true}} A_{kl}^{\text{true}}}{A_{ik}^{\text{true}} A_{jl}^{\text{true}}} K_{ijkl}
 \end{aligned} \tag{2.1.14}$$

The only external factors that are remaining are the crossmultiplying gain factors combined in  $k_{ijkl}$ . These factors are set by the correlator-system and assumed to be very stable and constant so the closure-amplitude can be normalized

$$A'_{ijkl} = \frac{A_{ij}^{\text{true}} A_{kl}^{\text{true}}}{A_{ik}^{\text{true}} A_{jl}^{\text{true}}} \tag{2.1.15}$$

and is now independent of any external error. By using a little trick it is also possible to get a closure-relation for the amplitudes only with tree baseline. In this case the lack of one baseline is completed by correlating one antenna with itself. In the same way as described in the section before the closure-amplitudes of the baselines of an observation can also be used to do a self-calibration for the amplitudes of the observed visibilities. Also here a CLEAN model is necessary to do this calibration.

For the process of hybrid imaging several cycles of CLEAN and selfcalibration are applied on the visibility data to establish the final clean image of a source.

### **2.1.3. Modelfitting**

Modelfitting is used to determine the size, the position and the flux of an emission-region of a radio source. After imaging a radio-interferometer dataset, the raw data is now calibrated through several phase and amplitude self-calibration cycle. In the final image the data-set is modeled by several clean components, which represents each a single point-source and with convolution with the clean beam become a representation of the brightness-distribution of the considered object. Because in this concept greater emission-regions are modeled by more then one component another way must be found to describe one emission region preferably by one model component to the size, position and flux.

## 2.2. Sample-selection

With respect to the unification scheme of AGN, as described in Sec.1.1, BL Lac objects are the beamed and rotated counterparts of FR1-radiogalaxies and FSRQs the beamed and rotated counterparts of FR2-radiogalaxies. To test this assumption [Kharb et al. \(2010\)](#) studied a sample of blazars on the northern hemisphere. The sample contains 135 radio-loud AGN of the VLBI-observation-program MOJAVE<sup>2</sup>, which were observed with the 'Very Large Array' (VLA) at 1.4 GHz to study the kiloparsec structure and luminosity of these sources. In the study they find some deviations from the unification scheme of AGN. They found 6 BL Lac objects with FR2 luminosities and 4 of these show also hotspots. 5 of the BL Lac's have luminosities in the regime between FR1 and FR2, 2 of these show also hotspots. 7 BL Lac objects feature extended luminosities in the FR1 regime, also 3 of these show hotspots. They found also 22 FSRQs with extended luminosities of  $24.5 < \log(L_{\text{ext}}/(Ws^{-1})) < 26$ . The study suggests that the unification scheme is an oversimplification.

The study of [Kharb et al. \(2010\)](#) contains AGN on the northern hemisphere, but it is also interesting to extend the sample with sources at the southern hemisphere.

To get a clear defined sample for the study, the sources of the TANAMI sample were compared with the sources observed with the VLA at 1.4 GHz. To get a good sensitivity only sources with a minimal integration time of 8 minutes are considered. For the sample the six  $\gamma$ -loudest object are chosen and for comparison also 3  $\gamma$ -quiet objects are selected.

The  $\gamma$ -loudness of the sources is calculated in the following according to [Lister et al. \(2011\)](#) and [Linford et al. \(2012\)](#). The  $\gamma$ -loudness is defined as ratio of  $\gamma$ - and radio-luminosity:

$$G = \frac{L_{\gamma}}{L_R} \quad (2.2.1)$$

According to [Lister et al. \(2011\)](#) the  $\gamma$ -luminosity can be computed as

$$L_{\gamma} = \frac{4\pi D_L^2 S_{\gamma}}{(z+1)^{2-\Gamma}} \quad (2.2.2)$$

Here  $D_L$  is the luminosity-distance,  $z$  the redshift of the source  $S_{\gamma}$  the  $\gamma$ -flux between  $0.1 \text{ GeV} < S < 100 \text{ GeV}$  and  $\Gamma$  the  $\gamma$ -photonindex of the observed bandwidth. The values of  $S_{\gamma}$  and  $\Gamma$  of each source are taken from the second source catalog of the Fermi large area telescope by [Nolan et al. \(2012\)](#). The radio-luminosity is defined as the following:

---

<sup>2</sup>MOJAVE (Monitoring Of Jets in Active galactic nuclei with VLBA Experiments) is a monitoring program of AGN with the very large baseline array at 15 GHz. The sample contains AGN with VLBI-flux greater than 1.5 Jy. ([Lister et al. 2013](#))

$$L_R = \frac{4\pi D_L^2 S_R \nu}{z + 1} \quad (2.2.3)$$

Here  $S_R$  indicates the radio fluxdensity and  $\nu$  the observation frequency. The flux values are taken from observations at  $\nu = 1.4$  GHz as shown in Tab.2.1. Combining the equation for  $L_\gamma$  and  $L_R$  the formula for the  $\gamma$ -loudness becomes

$$G = \frac{S_\gamma}{S_R} (z + 1)^{\Gamma-1} \quad (2.2.4)$$

Each source is shown together with its AGN-class, redshift,  $\gamma$ -flux,  $\gamma$ -photonindex, radio-flux and  $\gamma$ -loudnes in table 2.1. The radio flux data is taken from the ATCA-observation catalog of 202 southern AGN by Tingay et al. (2003) or of the VLA all sky survey by Condon et al. (1998). The sample consists now of 9 AGN.

**Table 2.1.:** All sources of the sample ordered by  $\gamma$ -loudness, with name, the AGN class, redshift  $z$ , fermi  $\gamma$ -flux  $S_\gamma$  between  $100 \text{ MeV} < E_\gamma < 100 \text{ GeV}$ , the photon-index  $\Gamma$  in this energy range, radio fluxdensity  $S_R$  at  $\nu = 1.4$  GHz and the  $\gamma$ -loudnes  $G$ . The upper part contains the  $\gamma$ -loudest sources of the TANAMI sample observed with the VLA and the lower part the three  $\gamma$ -quiet sources for comparison.

source	class	$z$	$S_\gamma [10^{-12} \frac{\text{erg}}{\text{s} \times \text{cm}^2}]^9$	$\Gamma^9$	$S_R [\text{Jy}]$	$G [10^3]$
0426-380	Q	1.11 <sup>1</sup>	286.0	2.04	1.09 <sup>10</sup>	44.4
2155-304	B/Q	0.116 <sup>2</sup>	282.8	1.84	0.490 <sup>11</sup>	44.3
0402-362	Q	1.417 <sup>3</sup>	83.4	2.51	1.01 <sup>10</sup>	22.6
0537-441	Q	0.894 <sup>4</sup>	368.3	2.09	2.89 <sup>10</sup>	18.3
1313-333	Q	1.21 <sup>5</sup>	31.3	2.31	1.13 <sup>10</sup>	5.59
1104-445	Q	1.598 <sup>6</sup>	17.1	2.67	2.44 <sup>10</sup>	2.47
0521-365	B	0.055338 <sup>3</sup>	65.9	2.42	4.71 <sup>10</sup> 15.62 <sup>11</sup>	0.325-1.08
0625-354	G	0.054594 <sup>7</sup>	17.2	1.93	2.37 <sup>11</sup>	0.544
0438-436	Q	2.863 <sup>8</sup>	n.a.	n.a.	4.53 <sup>10</sup>	n.a.

<sup>1</sup> Heidt et al. (2004); <sup>2</sup> Falomo et al. (1993); <sup>3</sup> Jones et al. (2009);  
<sup>4</sup> Peterson et al. (1976); <sup>5</sup> Jauncey et al. (1982); <sup>6</sup> Peterson et al. (1979);  
<sup>7</sup> Quintana & Ramirez (1995); <sup>8</sup> Morton et al. (1978); <sup>9</sup> (Nolan et al. 2012);  
<sup>10</sup> Tingay et al. (2003); <sup>11</sup> Condon et al. (1998);

**0402-362 (PKS 0402-362)** is classified as FSRQ according to [Healey et al. \(2007\)](#). The spectrum is flat in the radio regime with no significant steepening at the low-frequencies. In VLBI studies by the US naval observatory, shown in Fig.2.7, a bright radio core is visible with a jet evolving in the northern direction up to a core-distance of about 12 mas.

**0426-380 (PKS 0426-380)** was classified as FSRQ by [Healey et al. \(2007\)](#) and is according to [Nolan et al. \(2012\)](#) and table 2.1 the  $\gamma$ -loudest source of the sample. In the VLBI image by [Müller et al. \(2017\)](#) of the source in Fig.2.7 the source shows a bright radio-core and an emission region in the eastern direction up to a core-distance of about  $d_{\text{core}} = 4$  mas on parsec-scales.

**0438-436 (PKS 0438-43)** The flat spectrum radio quasar was classified first by [Healey et al. \(2007\)](#). In the VLBI image observed by the TANAMI-project ([Ojha et al. \(2010\)](#)), shown in Fig.2.7, a bright core and several emission regions, belonging to a jet like structure, extending up to a cor-distance of about  $d_{\text{core}} \approx 35$  mas.

**0521-365 (PKS 0521-36)** is difficult to classify in the standard-model of AGN. An spectrum analysis, conducted by [Véron-Cetty & Véron \(2006\)](#) the galaxy to be classified as Seyfert 1 galaxy with broad emission lines. But the object features also a jet in the north-western direction in the optical regime ([Falomo 1994](#)) and the radio regime, first discribed by [Liu & Xie \(1992\)](#). With respect to the optical luminosity analyzed by [Sbarufatti et al. \(2005\)](#) the source is also classified as BL Lac. VLBI studies ([Ojha et al. 2010](#)) measure a jet pointing in the north-eastern direction up to  $d_{\text{core}} \approx 70$  mas as seen in Fig.2.7 . In the optical regime [Falomo \(1994\)](#), shown in figure 2.2, observe a kilo-parsec jet pointing in the same direction (N-W) as visible in the VLBI image. They found also a bright spot (component C) at a distance of about 2 arcsec from the ending of the jet, but [Falomo \(1994\)](#) could make no statement, if this spot belongs to 0521 – 436 or is a sepearte object. [Gopal-Krishna & Wiita \(2000\)](#) observed the source at  $\nu = 15.3$  GHz with the VLA, as shown in Fig.2.3, and identify one hotspot in the south-eastern direction, so they classified the source as a hybrid Fanaroff-Riley object.

**0537-441 (PKS 0537-441)** is typically classified as a BL Lac object because of the lack of optical emssion lines. But in the study of [Peterson et al. \(1976\)](#) a Mg-II -line could be identified and the redshift could be calculated to  $z = 0.894$ , meaning it could also be classified as FSRQ. Because of the measurement of the Mg-II line the amplitude of the Lyman- $\alpha$  line can be calculated. But [Maraschi et al. \(1985\)](#) did not find a Lyman- $\alpha$  line at the expected position in the spectrum. In the study [Maraschi et al. \(1985\)](#) also found a spectral behavior in the UV-range more typical for a BL Lac object and they conclude that 0537 – 441 is transitory object between FSRQ and BL Lac, switching

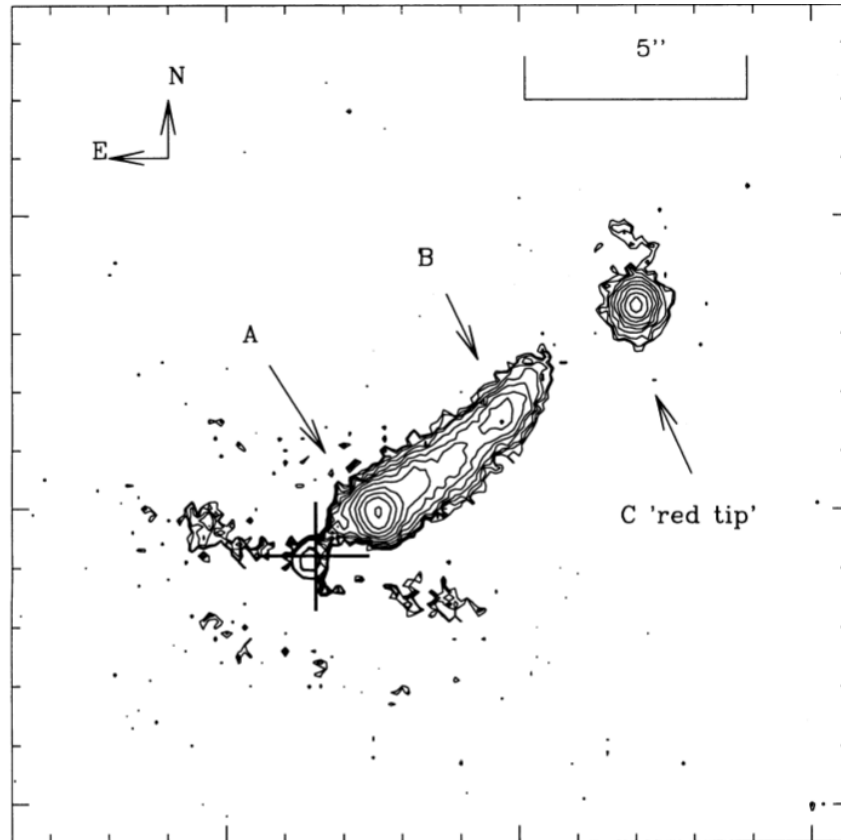


**Figure 2.2.:** Optical image of 0521-365 observed with the ESO NTT at the optical R-band by Falomo (1994). The host galaxy was filtered and is located at the black cross in the image. A jet extending beginning at component 'A' up to component 'B' in N-W direction with a length of about 6 arcsec. Alongside the jet axis at a separation of about 1 arcsec from the end of the jet is also a bright red tip visible (component 'C'), which could be caused by a background galaxy.

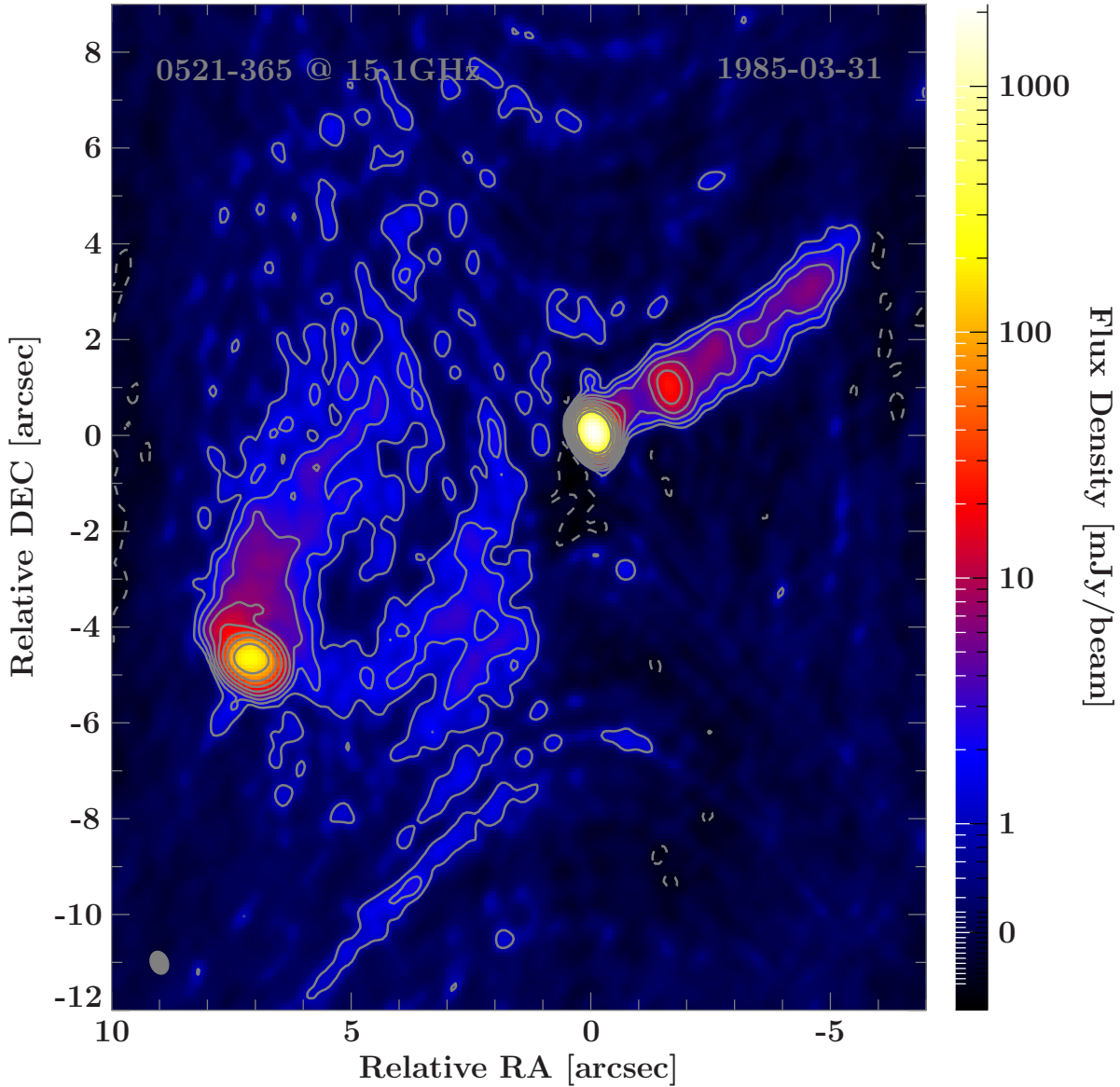


**Figure 2.3.:** VLA image of 0521-365 at 15.1 GHz in A-B configuration by Keel (1986) reimaged. RMS: 0.30 mJy, map-peak: 2.16 Jy, beam:  $(0.490 \times 0.368)$  arcsec at  $20.9^\circ$ . Smallest contourlevel at three times RMS for positive and negative fluxdensities. The other contours changing exponential with base 2 in the positive fluxdensity regime. A one-sided jet in north-western direction is visible together with a hotspot and lobe in south-eastern direction.

between the two states and was in the BL Lac state at the observation by [Maraschi et al. \(1985\)](#).

The emission of the object is variable across the electromagnetic spectrum, with a timescale of  $\tau \approx 2$  yr ([Komesaroff et al. \(1984\)](#)) at  $\nu = 5$  GHz, and in EGRET within months ([Hartman et al. \(1999\)](#)) and is the second brightest object on the southern FERMI-LAT sky ([Abdo et al. \(2009\)](#)). To explain these high fluctuations in flux throughout the electromagnetic spectrum and the change between appearance and disappearance of emission and absorption lines, two studies by [Stickel et al. \(1988\)](#) and [Lewis & Ibata \(2000\)](#) discussed, whether 0537-441 is influenced by gravitational lensing. According to [Lewis & Ibata \(2000\)](#) the fluctuations could be caused by the microlensing effect of stars of a foreground-galaxy. But neither one of the studies could significantly detect a foreground galaxy yet, which could be associated with a gravitational lens for 0537-441. Only a nearby galaxy not in the field of view with almost the same redshift as 0537-441. TANAMI observations, see Fig.2.7 from [Ojha et al. \(2010\)](#), show a bright core and a jet extending to the north-eastern direction up about 4 mas from the core with a following bend to the south-eastern direction up to 5 mas from the core

**0625-354 (PKS 0625-35)** is classified by [Wills et al. \(2004\)](#) according to the optical spectrum as BL Lac object. The parsec-scale structure of the source at  $\nu = 8.4$  GHz in Fig.2.7 obtained by [Ojha et al. \(2010\)](#), show a one-sided jet in south-eastern direction, with an extension up to  $d_{\text{core}} = 95$  mas. At  $\nu = 2.4$  GHz in the study of [Venturi et al. \(2000\)](#), analyzing data taken by the large baseline array (LBA), there is even a diffuse component at a core-distance of about  $d_{\text{core}} = 200$  mas visible. [Venturi et al. \(2000\)](#) also constrain the apparent jet speed on parsec scale to  $0.47 < \beta_{\text{app}} < 0.74$  by tracking jet components in the parsec scale jet.

**1104-445 (PKS 1104-445)** The source was first classified as FSRQ by [Healey et al. \(2007\)](#). The VLBI-map by [Ojha et al. \(2010\)](#) in Fig.2.7 shows a jet component in north-eastern direction at a core-distance of  $d_{\text{core}} = 3$  mas. Because of a component size of  $\theta_{\text{maj}} > 8$  mas [Ojha et al. \(2010\)](#) suggest that the jet features a large projected opening angle, whereas [Shen et al. \(1997\)](#) suggest a bending of the jet. [Trüstedt \(2013\)](#) measures the apparent jet speed to be  $\beta_{\text{app}} = 57.67 \pm 9.58$  by tracking components of the VLBI jet.

**1313-333 (PKS 1313-333)** The source is classified as FSRQ first by [Healey et al. \(2007\)](#) and [Nolan et al. \(1996\)](#) find 1313-333 to be the possible counterpart of the EGRET gamma-ray source 3EG J1314-3431. They also show, that the source features a high variability in the high radio frequencies ( $\nu = 90$  GHz and  $\nu = 230$  GHz) at timescales of months to years, where the fluxdensity varies between  $1 \text{ Jy} \lesssim S_{\nu} \lesssim 3 \text{ Jy}$ . In the TANAMI image by [Ojha et al. \(2010\)](#) in Fig.2.7 a jet extending in western direction up to about  $d_{\text{core}} \approx 10$  mas is visible.

**2155-304 (PKS 2155-304)** is a well known  $\gamma$ -ray and x-ray source, detected with EGRET by Vestrand et al. (1995) and in the TeV regime with H.E.S.S. by Aharonian et al. (2005) and is the second  $\gamma$ -loudest source of the sample. The H.E.S.S. study detect a variability of month in which the  $\gamma$ -flux of the source varies between 40% and 60% Crab-nebula equivalents. They detect also some features in the  $\gamma$ -spectrum, which could be caused by intrinsic processes in 2155-304 or could be the consequence of absorption by the cosmic microwave background. In July 2006 H.E.S.S. (Aharonian et al. (2007)) detect also a  $\gamma$ -ray outbursts with a flux maximum of seven times the Crab-nebula equivalent at  $E = 200$  GeV, at timescales between  $200 \text{ s} \lesssim t \lesssim 600 \text{ s}$ . According to the maximal time-scale and size of the emission region comparable with the Schwarzschild-radius the Doppler-factor could be constrained to be  $\gamma > 100$ . Previous x-ray studies by Chiappetti et al. (1999) and Kataoka et al. (2000) constrain the Doppler factor to  $20 \lesssim \delta \lesssim 30$  using the variabilities in the x-ray spectra. According to Healey et al. (2007) the spectrum in the radio regime is flat and the source is classified as flat spectrum radio source. According to optical studies by Véron-Cetty & Véron (2006) and x-ray studies according to Piner & Edwards (2004) the source is classified as BL Lac object.

On parsec scales 2155-304 features a bright core with a jet extending in south-eastern direction up to a core-distance of about  $d_{\text{core}} \approx 10$  mas, which is shown in the TANAMI image in Fig.2.7 taken from the study of Ojha et al. (2010). Pandey-Pommier et al. (2016) presented images of GMRT observations of 2155 – 304, taken at  $\nu = 235$  MHz and  $\nu = 610$  MHz to analyze the kiloparsec structure of the object. The 235 MHz image is shown in Fig.2.4 and the 610 MHz image in Fig.2.5. Both images show a typical FR1 like structure, with a complex extended emission in eastern and western direction from the bright radio core, which can assumed to be the two lobes of the jet and counter-jet. The overall size of the source is about  $s = 200$  arcsec, which is conform with the size obtained from the VLA observations of Ulvestad & Antonucci (1986), presented reimaged in figure 2.6. All three kiloparsec images show almost the same size of the source, but with the difference, that only the 610 MHz image in Fig.2.5 can really resolve the lobe structure of the source, whereas the other two images show only a halo around the core. Zooming in the more inner region of the source, Seeg (2017) analyzed the jet bending on kiloparsec scales using GMRT observation data at  $\nu = 1.4$  GHz and VLA data observed with A-configuration at  $\nu = 4.8$  GHz analyzed also in this study and C-configuration by Ulvestad & Antonucci (1986). Seeg (2017) detect that the jet crosses the line of sight. Because the study of Seeg (2017) emerges also in cooperation with analysis for this study the details are discussed in section 3.2 in detail, with further analysis with VLA A-configuration data observed at  $\nu = 1.4$  GHz and ATCA data observed at the same frequency, to compare the two studies.

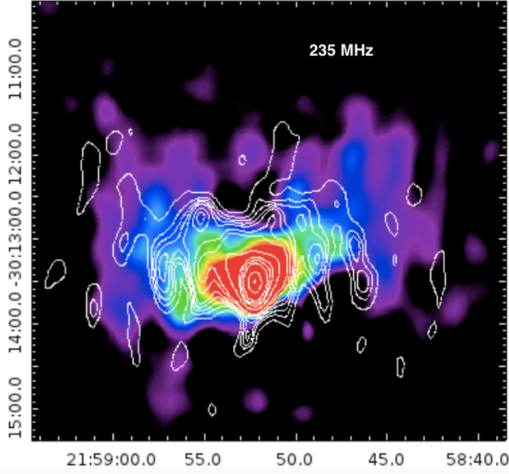


**Figure 2.4.:** 235 MHz image of 2155-304 observed by the GMRT; the source shows a typical FR1 structure. Credits by [Pandey-Pommier et al. \(2016\)](#)

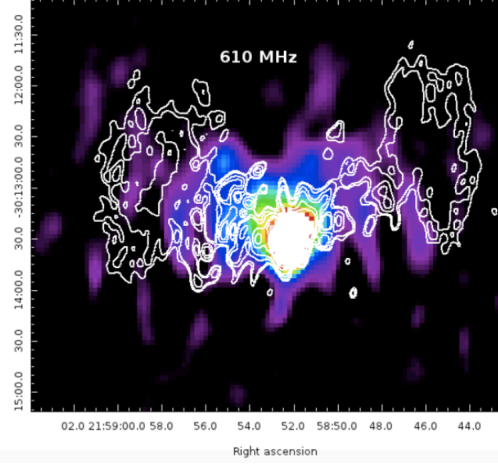


**Figure 2.5.:** 610 MHz image of 2155-304 observed by the GMRT; the source shows a typical FR1 structure. Credits by [Pandey-Pommier et al. \(2016\)](#)

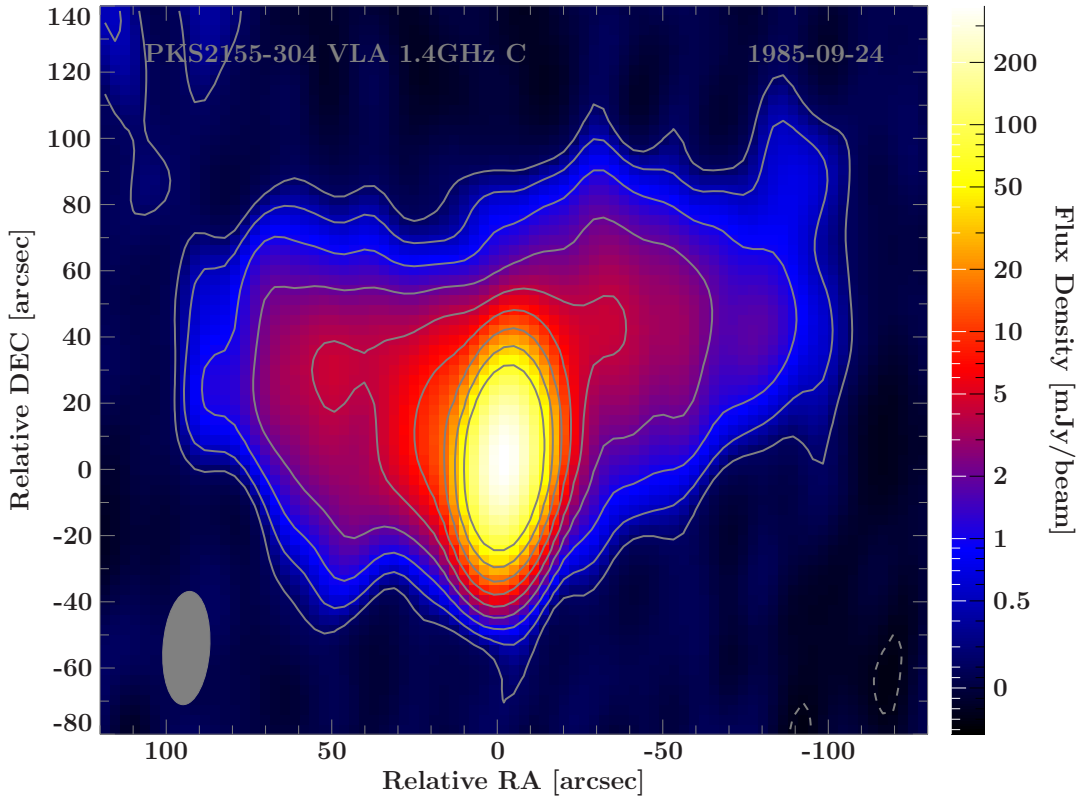


**Figure 2.6.:** VLA C-configuration image of 2155-304 at 1.5 GHz first described by [Ulvestad & Antonucci \(1986\)](#); the data are new calibrated and reimaged for this study.

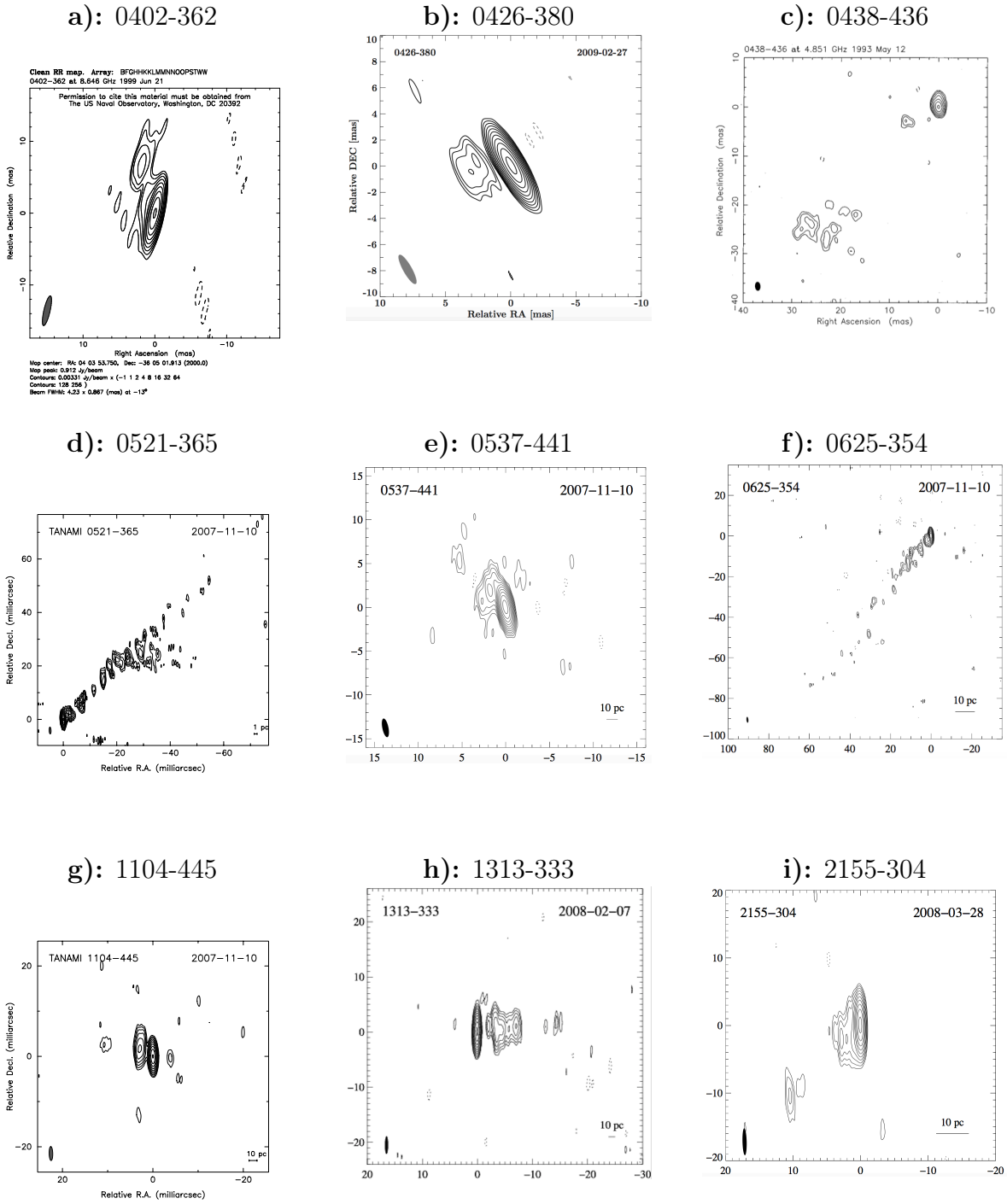


**Figure 2.7.:** VLBI images of all sources of the sample. All images except the image **c)**, was observed at  $\nu = 8.4$  GHz. Image **c)** of 0438-436 was observed at  $\nu = 4.8$  GHz. Images **d)**-**i)** are obtained from TANAMI observations of [Ojha et al. \(2010\)](#), image **b)** from TANAMI studies of [Müller et al. \(2017\)](#) and images **a)** and **c)** are taken out of the U.S. Naval Observatory archive. Jet directions: **a)**: N; **d)**: N-W; **h)**: W; **c)**, **f)** and **i)**: S-E; **b)** and **g)**: E; **e)**: N-E with possible jet bending anticlockwise.

## 2.3. Analysis methods for blazars

### 2.3.1. Extended radio-luminosity

To calculate the extended luminosity of the single sources the extended flux of the source must be determined. This done by measuring the overall flux  $S_{\text{oa}}$  and the flux of the radio-core  $S_{\text{core}}$  and the difference between these two values can assumed to be the extended radio-flux

$$S_{\text{ext}} = S_{\text{oa}} - S_{\text{core}}. \quad (2.3.1)$$

To measure the whole flux of the source the final clean image of the desired object is opened in DIFMAP and window is placed around the source and the program calculates the whole fluxdensity of all components in this window.

Calculating the core flux is a little bit more difficult. To determine the core-fluxdensity is to use the method of modelfitting explained in section 2.1.3. The flux is measured by modelfitting the core with an unresolved sperical Gaussian model-component. The boundary  $\theta_{\text{lim}}$  bedween a resolved and an unresolved model-component is given according to Kovalev et al. (2005) by

$$\theta_{\text{lim}} = \theta_{\text{maj}} \sqrt{\frac{4 \ln(2)}{\pi} \ln \left( \frac{\text{SNR}}{\text{SNR} - 1} \right)} \quad (2.3.2)$$

$\theta_{\text{maj}}$  represents the major axis of the clean image and  $\text{SNR}$  is the signal to noise-ratio of the considered component:

$$\text{SNR} = \frac{S_{\text{core}}}{\sigma_{\text{core}}} \quad (2.3.3)$$

with the fluxdensity  $S_{\text{core}}$  of the component and  $\sigma_{\text{core}}$  the radio noise nearby the considered component.  $S_{\text{core}}$  is measured by the modelfit and the noise is measured nearby the core of the source byThe core component is typically modeled with an unresolved Gaussian component in the phase center, Therefore the extended flux is the overall source flux minus the core flux. Now the extended luminosity of the object can be calculated according to Condon (1988) by knowing the redshift  $z$  and the spectral-index  $\alpha$  of the source and the Hubble-constant  $\mathcal{H}$

$$L_{\nu} = \frac{4\pi S_{\nu} c z}{\mathcal{H}^2 (z + 1)^{1+\alpha}} \quad (2.3.4)$$

The Hubble-constant is assumed to be  $\mathcal{H} = 71 \frac{\text{km}}{\text{s Mpc}}$  in this calculation. For comparison purpose with FR1 and FR2-radio galaxies the logarithm of the radio-luminosity  $\log(L_{\nu})$  is considered.

### 2.3.2. Constraining the inclination angles of AGN

Burd (2017) established a method to constrain the angle to the line of sight of a radio-jet by measuring the projected opening angle  $\zeta'$  of the observed jet and comparing it with a large sample of deprojected opening angles of observed radio-galaxies. The model uses the projection effect by observing a radio-jet. For the model it is assumed, that the jet is not bent and opens conical, because the assumption of a Blandford & Königl (1979) jet model. The model is illustrated in figure 2.8. As shown in part **a)** of the figure the radio source has an overall length  $s$ , but observing the source under an inclination angle  $\vartheta$  the only observable length is the projected length  $s'$ , which are connected by equation **a)** in the figure.

In part **b)** of figure 2.8 the intrinsic opening of the jet is shown and  $s$  can be connected with the diameter of a jet feature  $b$  and the intrinsic opening angle  $\zeta$  via equation **b)** in figure 2.8. In part **c)** the projected case of the jet opening is illustrated as seen by the observer. Because the projected length of the object gets smaller, but the size  $b$  of the observed emission region does not change by the projection the projected opening angle  $\zeta'$  gets bigger and  $s'$  is related to  $b$  and  $\zeta'$  with equation **c)** in the figure. Combining these three equations the inclination-angle can be constrained by

$$\vartheta = \arcsin \left( \frac{\tan \left( \frac{\zeta}{2} \right)}{\tan \left( \frac{\zeta'}{2} \right)} \right). \quad (2.3.5)$$

Because only  $\zeta'$  but not  $\zeta$  can be measured for a radio jet,  $\zeta$  is obtained by examine great samples of radio-galaxies with respect to statistical analysis of the jet opening-angle. This statistical analysis is done for a sample of FR1 radio-galaxies by Parma et al. (1987) and for FR2 radio-galaxies by Jeyakumar & Saikia (2000) separately.

In the case of FR1 radio-galaxies the opening angles of 55 radio-galaxies were measured by Parma et al. (1987) in the way, that the jet was modeled with several spherical Gaussian components. The opening angle for each single source was calculated by taking the average of all opening angles calculated for every model component of the source. These angles are sorted in categories of the length of  $\Delta\zeta = 2^\circ$ , the resulting data is plotted in a histogram 2.10 and is fitted by a Gaussian distribution with a most probable value of  $\zeta_{\text{mp}} = 10.9^\circ$ . The maximal opening angle is  $\zeta_{\text{max}} = 33.4^\circ$  and the minimal one  $\zeta_{\text{min}} = 3.4^\circ$ .

For the FR2 radio-galaxies Jeyakumar & Saikia (2000) calculated the opening angles by model fitting the hotspots of the radio galaxy and calculating the cone opening angle by connecting the two hotspots with a double cone shape. The opening angles of the 27 sources of Jeyakumar & Saikia (2000) are sorted in bins of  $\Delta\zeta_d = 1^\circ$ . The histogram of these data in figure 2.11 is also fitted with a Gaussian distribution and so the most probable value is  $\zeta_{>1} = 2.5^\circ$ , the maximal value  $\zeta_{\text{max}} = 19.6^\circ$  and the minimal value is  $\zeta_{\text{min}} = 1.4^\circ$ .

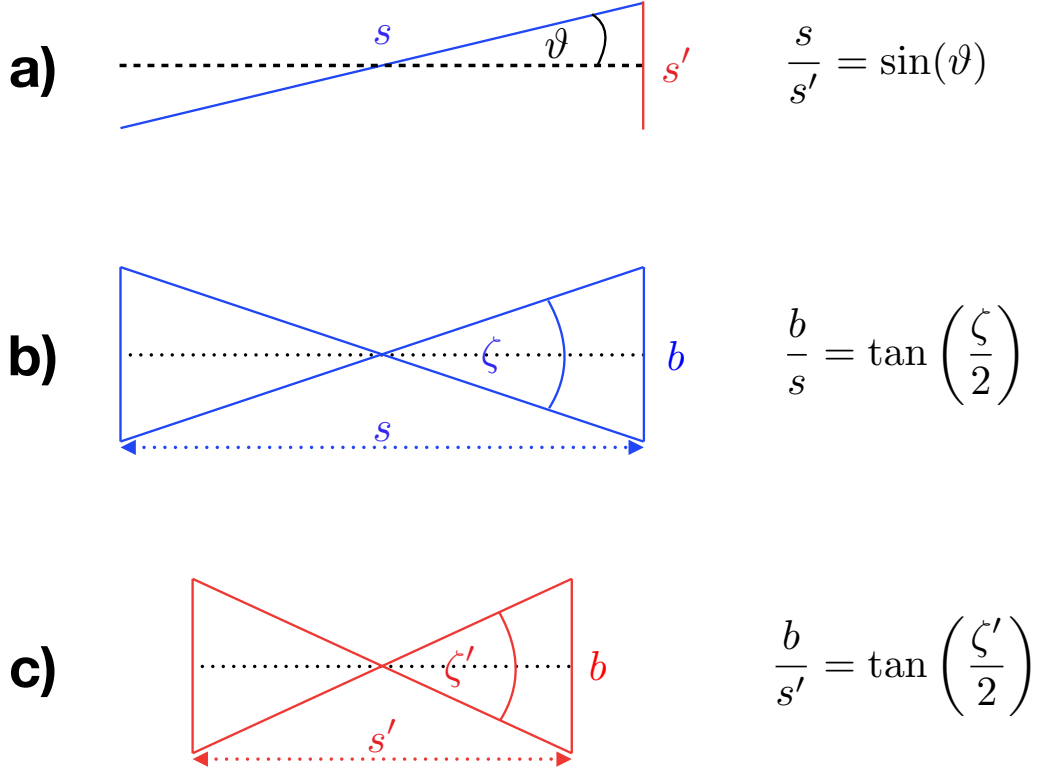


**Figure 2.8.:** Illustration of the calculation of the inclination-angle using the projected  $\zeta'$  and the deprojected opening angle  $\zeta$  of a radio-jet. **a):** Relation between the projected  $s'$  and deprojected length  $s$  and the inclination angle  $\vartheta$  of the jet. **b):** Relation between  $s$ , the deprojected opening angle  $\zeta$  and the diameter of the jet  $b$ . **c):** Relation between  $s'$ , the projected opening angle  $\zeta'$  and the diameter of the jet  $b$ . Adapted from [Burd \(2017\)](#)

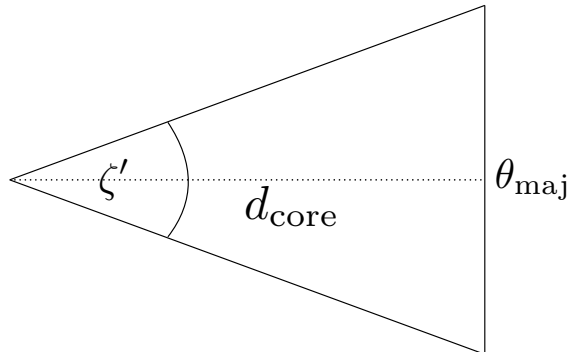


**Figure 2.9.:** Illustration of the measurement of the projected opening angle  $\zeta'$ . The Relation between the core-distance  $d_{\text{core}}$  and the major axis  $\theta_{\text{maj}}$  is used compute the projected angle.

To measure the projected opening angle of a radio-jet on kilo-parsec scales emission regions of the source which can be related to the jet or hotspots, which are related to mark the end of a radio-jet, are modelfitted. In the modelfitting process the core-distance  $d_{\text{core}}$  and major axis, meaning the full width half maximum (FWHM) of the emission region  $\theta_{\text{maj}}$  is calculated. With these two quantities the projected opening angle can be calculated according to figure 2.9 with

$$\zeta' = 2 \arctan \left( \frac{\theta_{\text{maj}}}{2 d_{\text{core}}} \right). \quad (2.3.6)$$

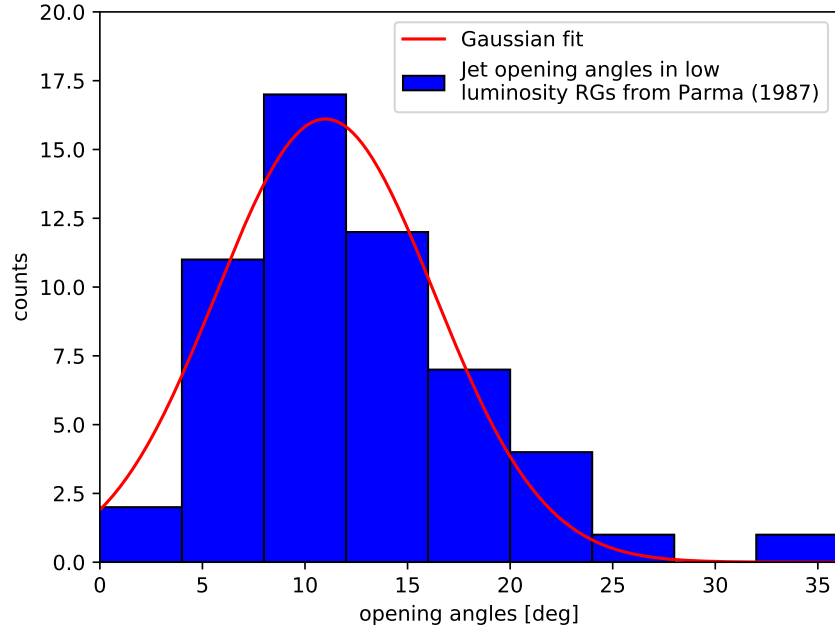


**Figure 2.10.:** Histogram for the distribution of opening angles of 55 FR1 radio galaxies according to [Parma et al. \(1987\)](#) with a binning of  $\Delta\zeta = 4^\circ$  and a minimal value of  $\zeta_{\min} = 3.4^\circ$  and a maximal of  $\zeta_{\max} = 33.4^\circ$ . The data are fitted with a Gaussian function to get the most probable opening angle  $\zeta_{\text{mp}} = 10.9^\circ$ , adapted from [Burd \(2017\)](#).

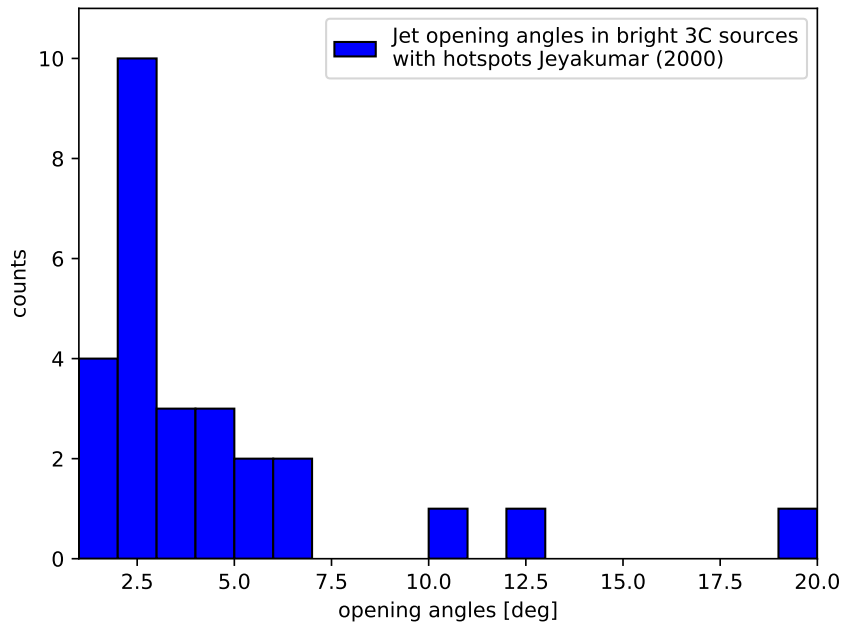


**Figure 2.11.:** Histogram for the distribution of opening angles of 27 FR2 radio galaxies according to [Jeyakumar & Saikia \(2000\)](#) with a binning of  $\Delta\zeta = 1^\circ$  and a minimal value of  $\zeta_{\min} = 1.4$  and a maximal of  $\zeta_{\max} = 19.6$ . The data are fitted with a Gaussian function to get the most probable opening angle  $\zeta_{\text{mp}} = 2.5^\circ$  adapted from [Burd \(2017\)](#).

# 3. Results

At first the results effecting the most parts of the sample are discussed and then the peculiarities of the single sources are discussed.

## 3.1. Sample results

### 3.1.1. Luminosity and spectral study

The dependencies of  $L_{\text{core}}$ ,  $L_{\text{ext}}$ ,  $\beta_{\text{app}}$  and  $z$  are studied for the nine sources sample. The four quantities are shown in table 3.1 for each source and are plotted against each other in Fig.3.1-3.4. The maximal apparent jet speed ( $\beta_{\text{app}}$ ) is only available for seven of the nine sources of the sample. For the sources 0426-380 and 0438-436 no studies with respect to the apparent speed exist, yet. Because of relativistic beaming effects discussed in section 1.1 the apparent maximal jet-speed can be written depending on the core-luminosity according to equations 1.1.7-1.1.9. The combination of these equations lead to the relation between apparent jet speed and observed core-luminosity:

$$\beta_{\text{app}} = \sqrt{2\gamma \left(\frac{L}{L_0}\right)^{1/p} - \left(\frac{L}{L_0}\right)^{2/p} - 1} \quad (3.1.1)$$

To compare the results of this study with the previous study by [Kharb et al. \(2010\)](#), the parameters are chosen in the same way like in fit by [Kharb et al. \(2010\)](#) to  $\gamma = 52$ ,  $p = 2$  and  $L_0 = 5 \cdot 10^{24} \text{ W Hz}^{-1}$ . Because  $\gamma$  and  $L_0$  are maximal values the resulting curve should be an envelope function to the measured values  $L$  and  $\beta_{\text{app}}$ . The envelope-function together with all available values for  $L$  and  $\beta_{\text{app}}$  are shown in Fig.3.1. All pair of values are laying under the envelope function with respect to their errors. [citekharb2010](#) showed that there is no sharp line between Bl Lacs and FSRQs. In this study Bl Lac objects show core luminosities below  $\log_{10}(L_{\text{core}}/\text{W Hz}^{-1}) = 25.5$  and posses speeds below  $\beta_{\text{app}} = 5$ , on the contrary the FSRQs show  $\log_{10}(L_{\text{core}}/\text{W Hz}^{-1}) > 26.9$  and  $\beta_{\text{app}} > 20$ , but this is the consequence of the small sample size. The luminosity and speed seem to be correlated, which is reasonable with respect to beaming effects.

Taking a look at the data in Fig.3.2 for the relation between  $\beta_{\text{app}}$  and  $L_{\text{ext}}$ , also mark-off between the two classes is visible, but also no significant correlation between extended luminosity and apparent speed is observable.

In Fig.3.3 the connection between  $L_{\text{core}}$  and  $L_{\text{ext}}$  is illustrated. It seems that  $L_{\text{ext}}$  raises with higher  $L_{\text{core}}$ , which is what physical is expected, because when the power of the

jet-engine gets higher also the extended emission should get higher, because if more energy fuels the inner jet also more energy reaches the outer parts of the object.

In Fig.3.4 the extended luminosity seems to be correlated with the redshift, this is a selection effect, because the selected objects have fluxdensities in almost the same magnitude but with different redshifts  $0 \lesssim z \lesssim 3$ . Meaning at the same fluxdensity with raising redshift also the luminosity gets higher. In the same figure also the extended luminosity limits for FR1 and FR2 objects at  $\nu = 1.4$  GHz are included according to Kharb et al. (2010). As expected according to the unification model for AGN all  $L_{\text{ext}}$  of FSRQs lay in the regime of the FR2 objects, whereas  $L_{\text{ext}}$  of the BL Lac objects lay in the intermediate regime between FR1 and FR2 objects. One BL Lac, 0521-365, with  $L_{\text{ext}} = 26.04$ , lays direct on the border to the FR2 objects, which is a special case and is discussed later on.

The spectra of all sources, presented in the appendix in figures 3.7-3.33, except the ones of 0521-365 and 625-354, which are dominated by extended emission, are flat in most parts of the radio regime, which is consistent with the low amount of extended emission and the domination of the beamed emission of the core in these sources. The fluxdensities measured in this study are all consistent with the existing parts of the spectra taken from NED<sup>1</sup>.

#### 3.1.2. Morphology

The two BL Lac objects 0625-354 and 2155-304 show a FR1 like structure, the FRSQ 1104-445 show two hotspots, which could be assumed to be true beamed and rotated counterparts of FR1 respectively FR2 galaxies. In all objects of the sample except for 0521-665, 0625-354 and 1104-445 jet bending occurs between the parsec scales and kilo-parsec scales. Only one source, 2155-304, is a FR1 object, where this is more common, because of the lower jet-power explained in Fig.3.30 later on.

The BL Lac 0521-365 and the FSRQ 0402-362 show also not two but only one hotspot. In case of 0521-365 the source show also a jet on the other side.

---

<sup>1</sup>NASA/IPAC Extragalactic Database: <https://ned.ipac.caltech.edu>

**Table 3.1.:** The classification the redshift  $z$ , the apparent speed  $\beta_{\text{app}}$ , the core-luminosity  $L_{\text{core}}$  and the extended luminosity  $L_{\text{ext}}$  is shown for each source of the sample.

source	class	$z$	$\beta_{\text{app}}$	$\log_{10}(L_{\text{core}}/\text{W Hz}^{-1})$	$\log_{10}(L_{\text{ext}}/\text{W Hz}^{-1})$
0402-362	Q	1.417 <sup>1</sup>	$(26, 0 \pm 10.2)^9$	27.25	26.69
0426-380	Q	1.11 <sup>2</sup>	n.a.	26.92	26.31
0438-436	Q	2.863 <sup>3</sup>	n.a.	28.34	27.87
0521-365	B	0.055338 <sup>1</sup>	$(< 0.36)^{10}$	25.22	26.04
0537-441	Q	0.894 <sup>4</sup>	$(53.7 \pm 23.1)^9$	27.58	26.64
0625-354	G	0.054594 <sup>5</sup>	$(4.31 \pm 1.04)^{11}$	24.82	25.33
1104-445	Q	1.598 <sup>6</sup>	$(57.67 \pm 9.58)^{11}$	27.78	26.67
1313-333	Q	1.21 <sup>7</sup>	$(22.7 \pm 5.0)^9$	27.15	26.63
2155-304	B/Q	0.116 <sup>8</sup>	$(0.93 \pm 0.32)^{12}$	24.89	24.59

<sup>1</sup> Jones et al. (2009); <sup>2</sup> Heidt et al. (2004); <sup>3</sup> Morton et al. (1978);

<sup>4</sup> Peterson et al. (1976); <sup>5</sup> Quintana & Ramirez (1995); <sup>6</sup> Peterson et al. (1979);

<sup>7</sup> Jauncey et al. (1982); <sup>8</sup> Falomo et al. (1993); <sup>9</sup> Piner et al. (2007); <sup>10</sup> Rösch (2016);

<sup>11</sup> Trüstedt (2013); <sup>12</sup> Piner et al. (2008);

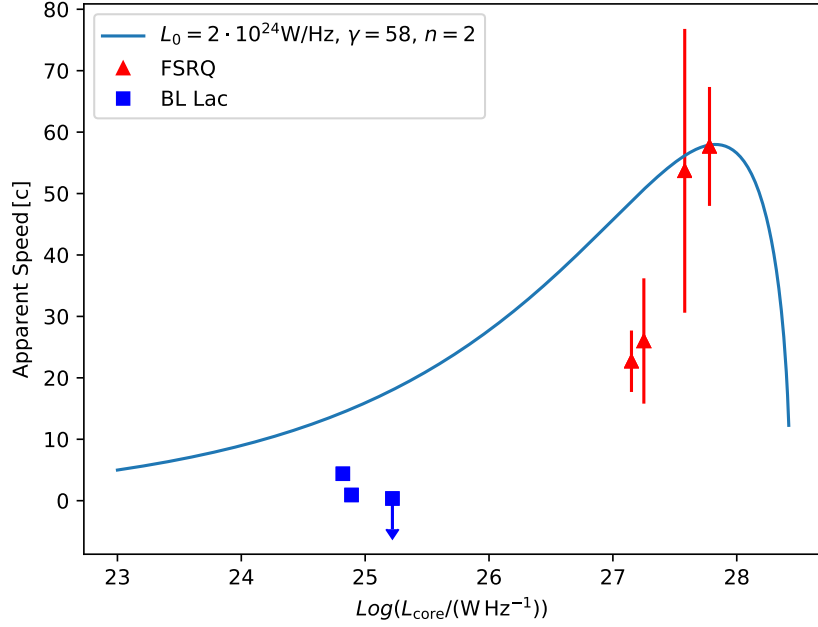


**Figure 3.1.:** Apparent jet speed as function of the core-luminosity, shown in logarithmic scale. FSRQs in red and BL Lac in blue. The references of the single apparent speeds are shown in table 3.1. The envelope function in blue is calculated according to equation 3.1.1.

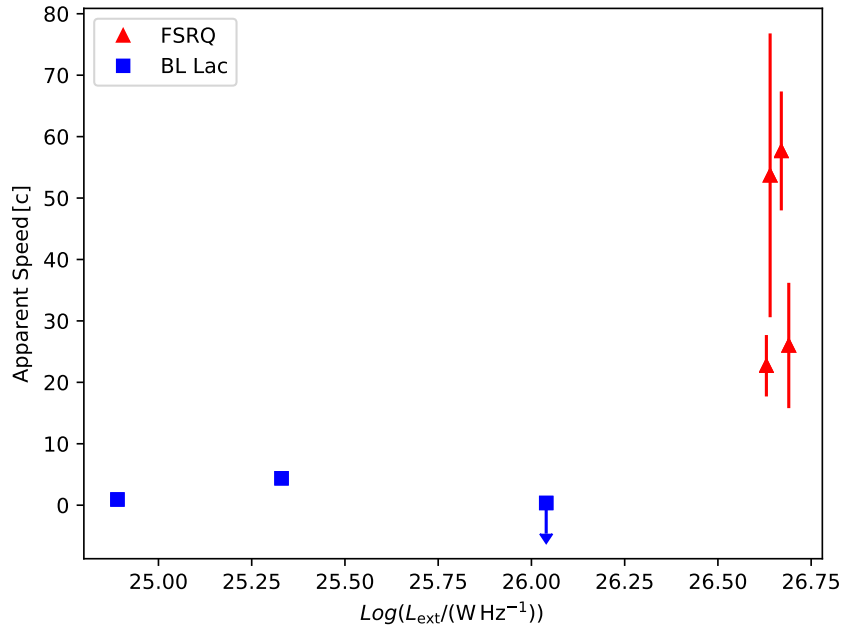


**Figure 3.2.:** Apparent jet speed as function of the extended luminosity, shown in logarithmic scale. FSRQs in red and BL Lac in blue. The references of the single apparent speeds are shown in table 3.1.1s.

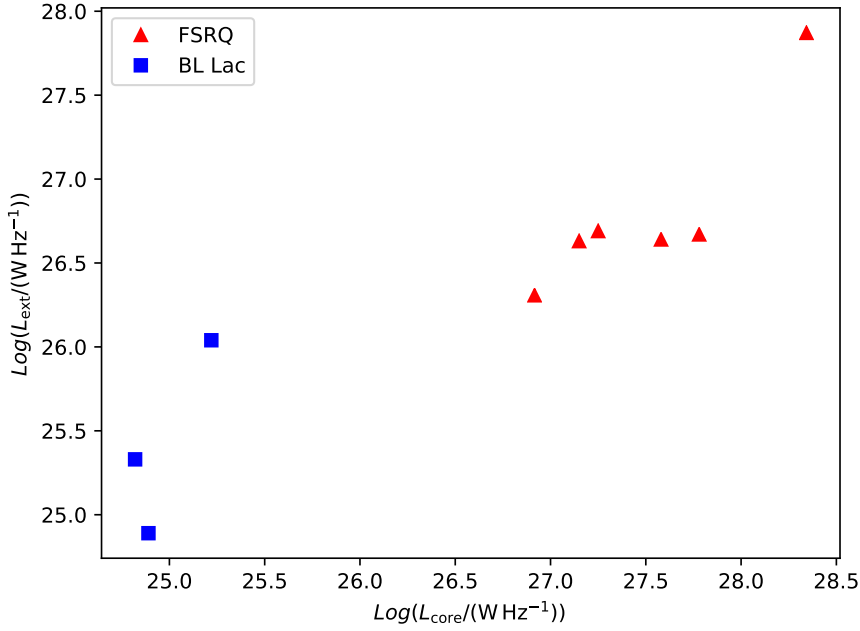


**Figure 3.3.:** Extended luminosity as function of the core-luminosity, both shown in logarithmic scale. FSRQs in red and BL Lac in blue

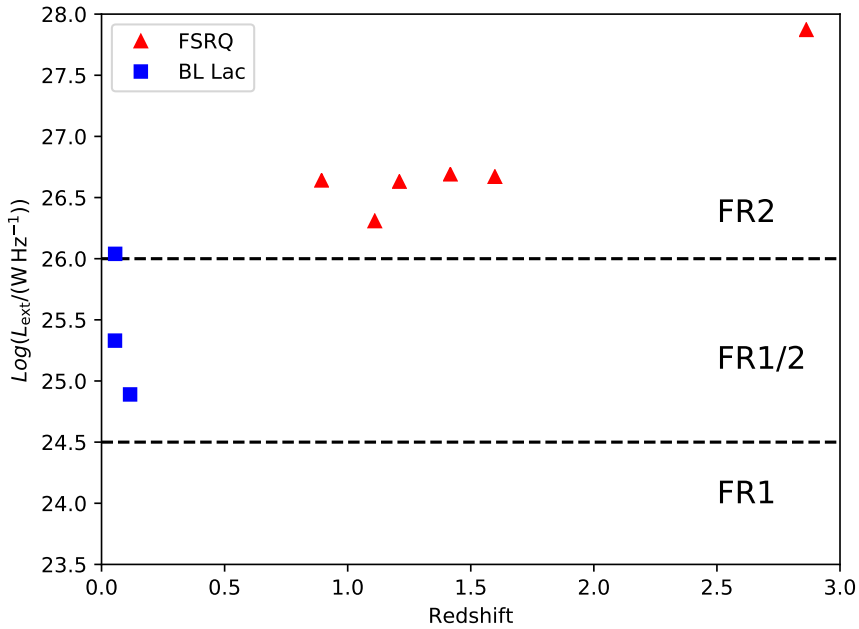


**Figure 3.4.:** Extended luminosity, in logarithmic scale, as function of the redshift. FSRQs in red and BL Lac in blue. The lower dashed line indicates the upper limit for the extended luminosity of FR1-objects and the upper line the lower limit of FR2-objects at  $\nu = 1.4$  GHz according to [Kharb et al. \(2010\)](#)

## 3.2. Single source results

### 0402-362

On kilo-parsec scales, observed with the VLA in A-configuration at 1.5 GHz, 0402-362 shows a bright core and a bright emission region in the south as shown in Fig.3.5. To get an evidence if the southern region could be a hotspot, the region is modefitted with a Gaussian model-component. With a FWHM  $\theta_{\text{maj}} = 846$  mas, which corresponds to a diameter of  $d \approx 7.26$  kpc. Comparing this value with common hotspot sizes of Jeyakumar & Saikia (2000), the size of the supposed hotspot is consistent with typical FR2 hotspot sizes. Another way to test the hotspot-hypothesis is to examine the spectral-index of this emission region, for this purpose also an observation at  $\nu = 4.8$  GHz with the VLA at A-configuration is studied, which results in the image in Fig.3.6. In this image also the hotspot-like feature in the south is visible. Between the two data-sets a spectral-index-map is calculated and is shown in Fig. and is 3.7. For the calculation of spectral index maps the image with smaller beam size is recovered with the larger beam and then the spectral index is calculated pixel by pixel. In the inner core-region of 0402-362 a declining trend of the spectral index can be seen towards the east, which could be a consequence of high core-flux variations over the seven years between the two observations. On kpc-scales this fluctuations should only effect the core-flux but not the extended flux, because fluctuations in the core need a much longer time-range to evolve in the outer parts of the source. The southern emission region shows a steep negative spectrum  $-1 \lesssim \alpha \lesssim -2$ , which is compatible with synchrotron-cooling for hotspots. The problem according to the unification scheme of AGN is that only one hotspot, but no two hotspots, is visible. A solution for the presence of only one hotspot could be that the counter-hotspot is possibly covered behind the core, because of a small misalignment of the two jets. So through projection-effects a misalignment of only a few degrees is enough to explain the covered second hotspot. An indication of the misalignment is that the jet on parsec-scale points in the opposite direction as the possible hotspot on kilo-parsec-scales, meaning the jet crosses the line of sight, but is bended only a few degrees because of projection effects. To calculate the possible misalignment between jet and counter-jet the angle to the line of sight for the jet and counter-jet must be constrained. The inclination angle is constrained as discussed in section 2.3.2. With a core-distance of  $d_{\text{core}} = 11.57$  arcsec and a major-axis of  $\theta_{\text{maj}} = 0.85$  arcsec of the hotspot the projected opening angle can be calculated to  $\zeta' = 4.19^\circ$ . With this value the inclination angle for the most probable and the smallest opening angle of Jeyakumar & Saikia (2000) can be calculated to  $\vartheta_{\text{mp1}} = 36.62^\circ$  and  $\vartheta_{\text{min1}} = 19.51^\circ$ . For a misalignment angle approximation it is assumed that the counter-hotspot has the same size as the measured hotspot and has a maximal core-distance of the beam-size in this direction of  $d_{\text{core}} = 3.51$  arcsec. So for the counter-hotspot the projected opening angle for the counter-jet can be calculated to  $\zeta' = 13.75^\circ$ . So the most probable inclination-angle becomes  $\vartheta_{\text{mp2}} = 10.43^\circ$  and the smallest  $\vartheta_{\text{min2}} = 5.82^\circ$ . The misalignment angle is calculated by taking the difference

between counter-hotspot and hotspot. The misalignment lays between  $\alpha_{\text{mp}} = 26.20^\circ$  and  $\alpha_{\text{min}} = 13.70^\circ$ , which is consistent with jet-counterjet misalignments in radio galaxies.

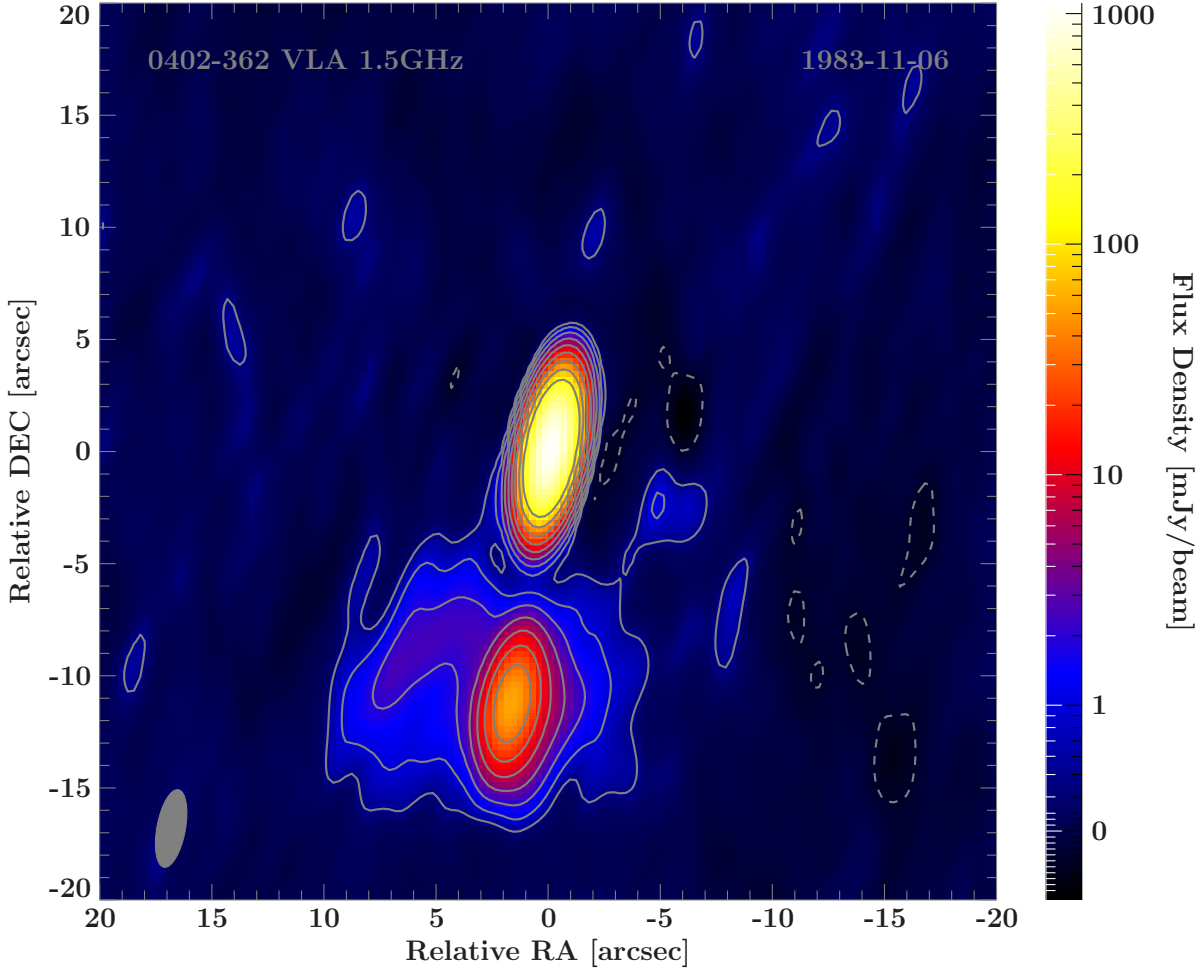


**Figure 3.5.:** VLA image of 0402-362 observed at 1.5 GHz in A-configuration. RMS: 0.16 mJy, map-peak: 1.11 Jy, beam:  $(3.51 \times 1.26)$  arcsec at  $-10.5^\circ$ . Smallest contourlevel at three times RMS for positive and negative fluxdensities. The other contours changing exponential with base 2 in the positive fluxdensity regime. A bright core and a bright hotspot-like emission region up to  $d_{\text{core}} \approx 15$  arcsec in southern direction is visible.

## 0426-380

Looking at the VLA image in Fig.3.8 0426-380 feature a bright core and an extension in the north-western direction up to a core-distance of about  $d_{\text{core}} \approx 5$  arcsec. The source can be modelfitted with one core-component and two jet components. The modelfit-data for the source is summarized in Tab.3.2. The second jet-component with  $S = 2.33$  mJy

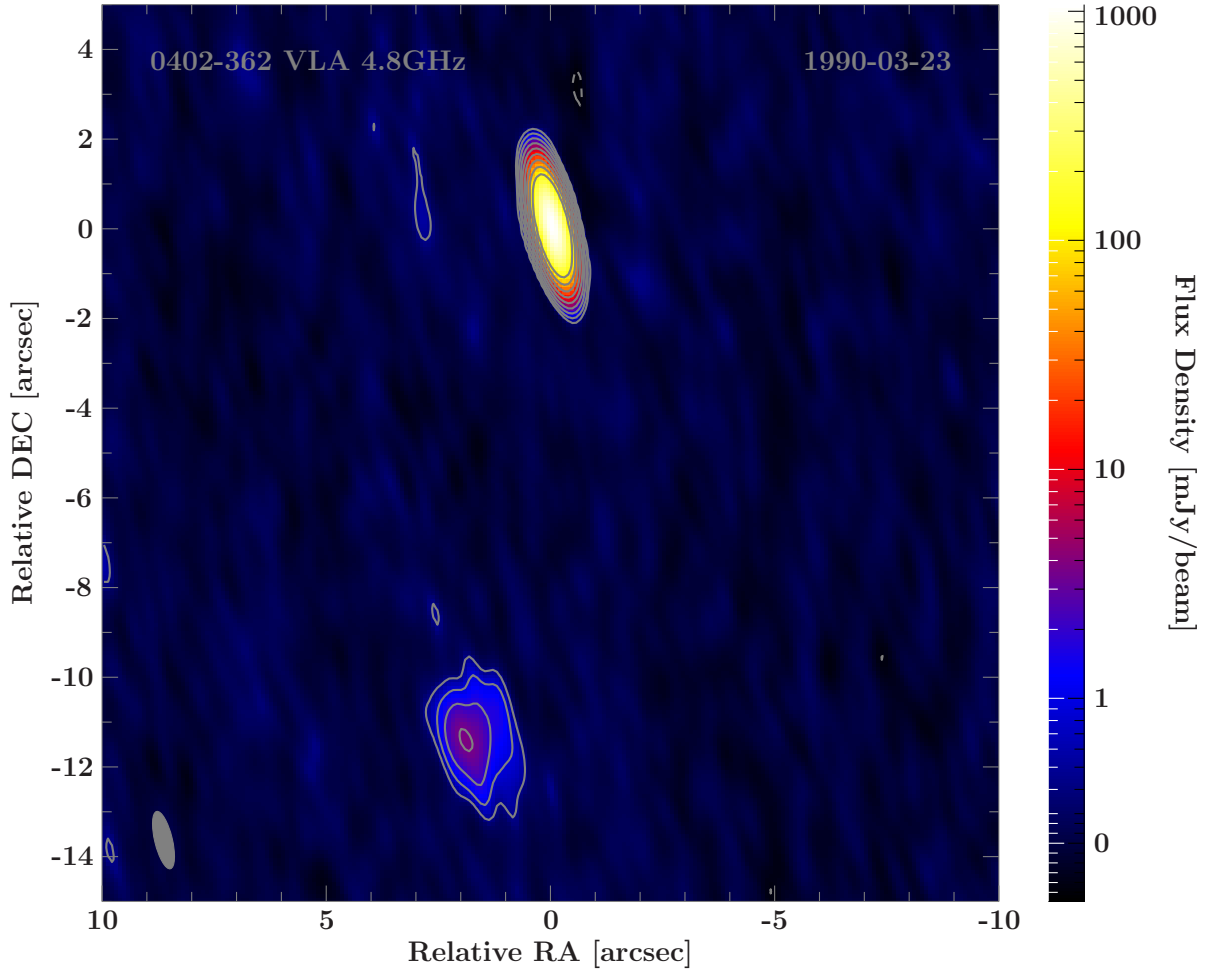


**Figure 3.6.:** VLA image of 0402-362 observed at 4.8 GHz in A-configuration. RMS: 0.15 mJy, map-peak: 1.07 Jy, beam:  $(1.31 \times 0.393)$  arcsec at  $13.5^\circ$ . Smallest contourlevel at three times RMS for positive and negative fluxdensities. The other contours changing exponential with base 2 in the positive fluxdensity regime. A bright core and a bright hotspot-like emission region at  $d_{\text{core}} \approx 12$  arcsec in southern direction is visible.

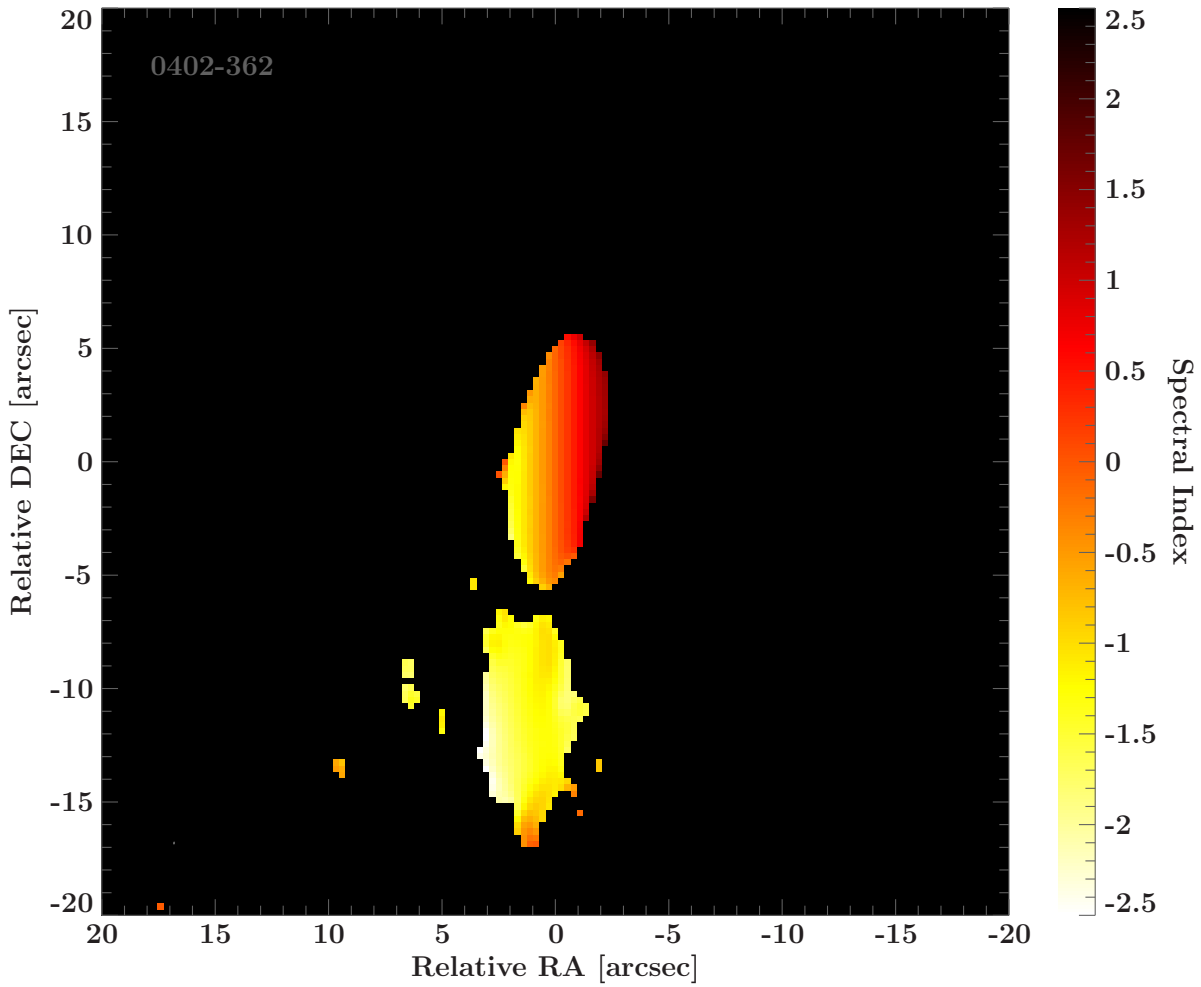


**Figure 3.7.:** 3-sigma spectralindex-map between the images 1.4GHz in figure 3.5 and 4.8GHz in figure 3.6. Flat core region with changing between positive and negative spectralindices because of different observation times. Steepening in the hotspot like structure down to  $\alpha \approx -1.5$

of flux is smaller than the first one. For an estimation of the inclination angle the first jet-component is used. For this component the projected opening angle can be calculated to  $\varphi_p = 21.58^\circ$ . Assuming a FR2 like structure of the source because of the FSRQ-classification, the inclination angle can be constrained for the most probable and the minimal deprojected opening angle of the study of Jeyakumar & Saikia (2000) to be  $\vartheta_{mp} = 6.57^\circ$  and  $\vartheta_{min} = 3.68^\circ$ , which is consistent with canonical values for blazar inclination angles. Recognizing the model-components of the kilo-parsec jet in Tab.3.2 the parsec and kilo-parsec jets are missaligned with an angle of  $\phi_{mis} \approx 130^\circ$  in the sky-plane, meaning the jet is bent. Because of projection effects and a low inclination angle of the source the real bending of the jet is much smaller. It is not possible to calculate the bending angle, because the jet could be bent in several 3 dimensional direction. It is only possible to constrain the bending angle, if the jet crosses the line of sight and only one bending direction is considered as in the case of 0402-362.

**Table 3.2.:** Summary of the model-components of 0426-380. For each component the name (Comp.) the fluxdensity  $S_\nu$ , the core-distance  $d_{core}$ , the position-angle  $\theta$  and the major-axis  $\theta_{maj}$  is shown. The table is split in two parts. The first row shows the modelfit for the core with an unresolved component. The other rows shows the object modeled with 3 model-components including one core-component

Comp.	$S_\nu$ [mJy]	$d_{core}$ [mas]	$\theta$ [°]	$\theta_{maj}$ [mas]
core <sub>1</sub>	661.34	7.36	169.57	78.87
core <sub>2</sub>	663.86	5.18	177.93	123.08
jet <sub>1</sub>	66.65	2755.91	-24.44	1050.51
jet <sub>2</sub>	2.33	4446.11	-40.09	366.09

### 0438-436

In the kiloparsec-scale image in Fig.3.9 observed by the VLA, the visible jet extends up to about  $d_{core} \approx 5$  arcsec. So between the parsec-scale jet in Fig.2.7 and kiloparsec-jet there is a misalignment of an angle of about  $\Delta\phi \approx 90^\circ$ , meaning the jet is bend in some way between these two regimes. In reality the jet isn't bent with an angle of  $\Delta\phi \approx 90^\circ$ , the angle is much smaller. The large angle appears because of projection effect, caused because the jet is pointed towards the observer with an low inclination angle.

The jet on kiloparsec-scales can be modelfitted with one component with  $S_\nu = 33$  mJy,  $d_{core} = 3.85$  arcsec,  $\theta_p = -157.59^\circ$  and  $\theta_{maj} = 737.87$  mas. With this model-parameters the projected opening angle of the jet can be calculated to  $\varphi_p = 10.94^\circ$  and so with the

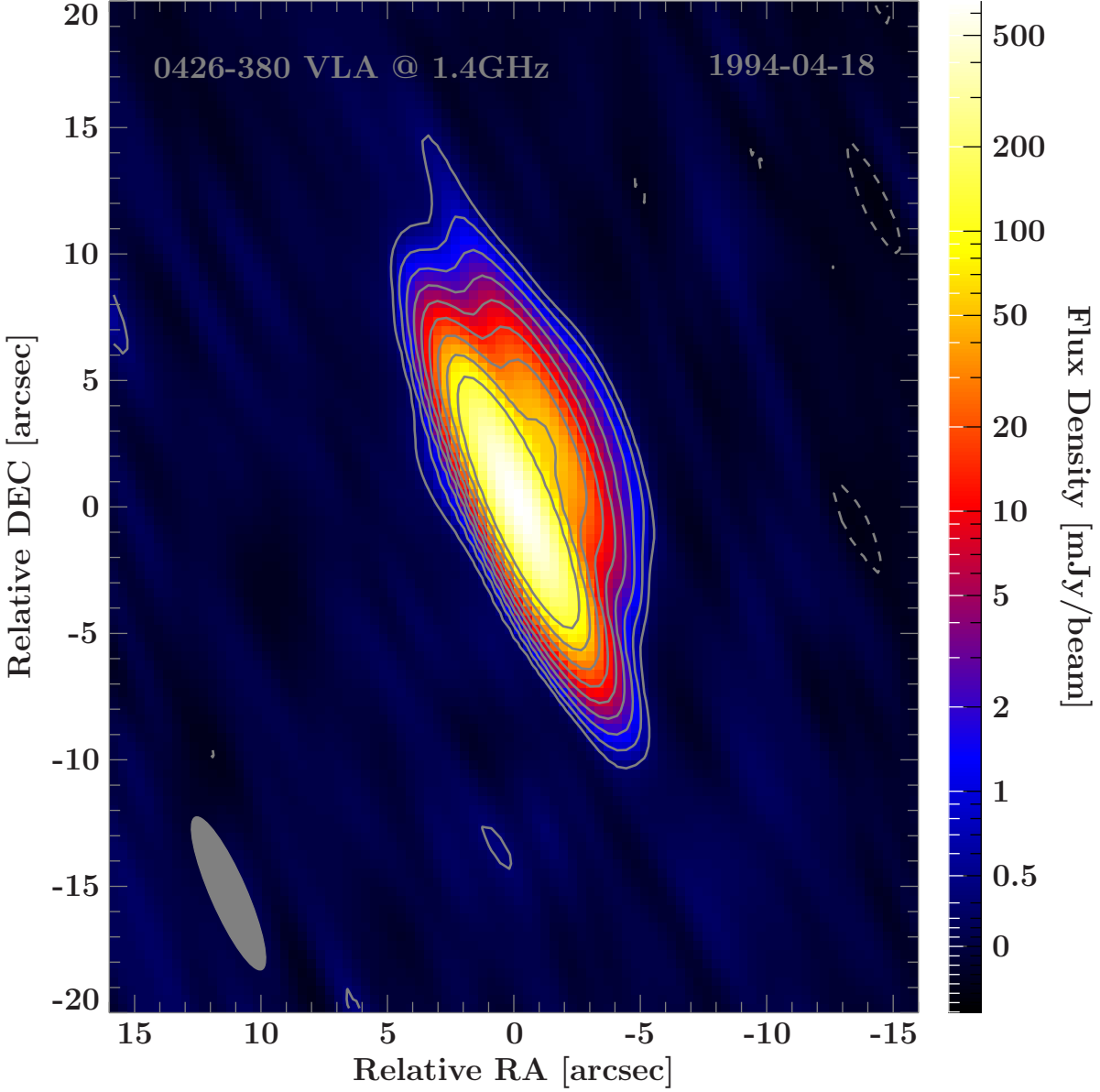


**Figure 3.8.:** VLA image of 0426-380 observed at 1.5 GHz in A-configuration. RMS: 0.14 mJy, map-peak: 0.663 Jy, beam:  $(6.57 \times 1.41)$  arcsec at  $23.6^\circ$ . Smallest contour level at three times RMS for positive and negative fluxdensities. The other contours changing exponential with base 2 in the positive fluxdensity regime. A bright core is visible and a jet extending up to  $d_{\text{core}} \approx 5$  arcsec in north western direction.

assumption of a FR2-like object the inclination angle can be computed to  $\vartheta_{mp} = 13.17^\circ$  for the most probable and to  $\vartheta_{min} = 7.33^\circ$  for the minimal value. The luminosity at  $\nu = 1.4$  GHz in the FR2-regime according to [Kharb et al. \(2010\)](#) together with the low opening angle also in the projected case is an evidence for a beamed and rotated FR2 galaxy.

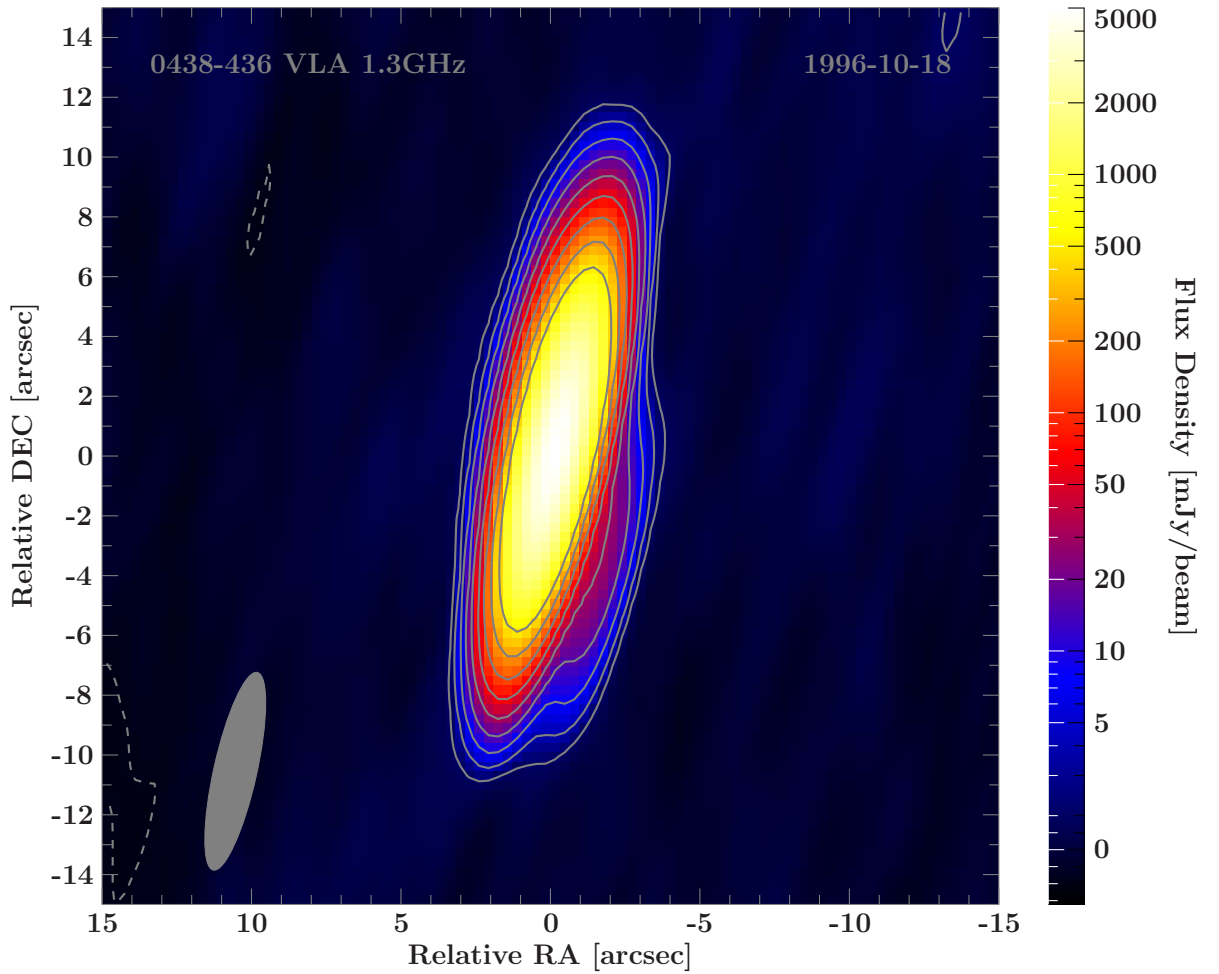


**Figure 3.9.:** VLA image of 0438-436 observed at 1.5 GHz in A-configuration. RMS: 0.64 mJy, map-peak: 5.02 Jy, beam:  $(6.77 \times 1.43)$  arcsec at  $-12.6^\circ$ . Smallest contour level at three times RMS for positive and negative fluxdensities. The other contours changing exponential with base 2 in the positive fluxdensity regime. A bright core is visible and a jet extending up to  $d_{core} \approx 3$  arcsec in south western direction.

## 0521-365

The kilo-parsec scale image observed with the VLA at  $\nu = 1.4$  GHz presented in Fig.3.10 shows almost the same morphology as in the 15 GHz image presented in Sec.2.2 in Fig.2.3. Meaning there is a hotspot present in the south eastern direction, for which the fluxdensity of  $S_\nu = 2.660$  at  $\nu = 1.4$  GHz excites the fluxdensity  $S_\nu = 1.241$  Jy of the core, and a jet extending in north-western direction. Additional to the morphology in the 15 GHz image the image at  $\nu = 1.4$  GHz shows also a halo around the hole structure, which is due to the fact that the telescope is more sensitive to the extended emission at lower frequencies explained in Sec.1.1. Comparing with the VLBI morphology in Fig.2.7 and the optical study by Falomo (1994) presented Fig.2.2 the jet points in the same direction, but the bright spot visible in the optical study at a small distance aligned to the jet doesn't appear here, meaning this emission region isn't a hotspot or part of the jet and do not belong to the object and is a separate object such as a background or nearby galaxy or a foreground star. Between the two VLA-images at  $\nu = 1.4$  GHz and  $\nu = 15$  GHz a spectral-index map is calculated and is shown in Fig.3.11. Some artifacts in the spectral-index map could be arise due to the fact, that here the image with the smaller beam-size ( $\nu = 15$  GHz) is convolved with the same much larger beam of the second image ( $\nu = 1.4$  GHz) to get the same amount of pixels. A better solution is to create a tapered image of the 15 GHz dataset by weighting down the long-baseline data, which leads to similar beam-size already in the imaging process as the 1.4 GHz image and lead to a more reliable spectral map. This will be done in further work on this topic. As expected the radio core is flat, the hotspot has a spectral index of about  $\alpha \approx -0.5$ , which can be explained by synchrotron cooling. At the northern part of the hotspot and between the core and the hotspot the spectrum is steeper up to  $\alpha \approx -1.6$  typical for lobe emission. The emission between core and hotspot must be treated with caution, because of possible artifacts due to the spectral-index calculation. It seems, that the decelerated gas from the hotspot drifts away in northern direction, which could arise due to the motion to a cluster medium of the whole object. In neither of the images presented here a hotspot on the jet-side appears. One explanation of this asymmetry could be the influence by nearby galaxies such in a galaxy-cluster as discussed by Schellenberger et al. (2017). An argument for this assumption is that another galaxy is visible near the end of the jet of the source, but for which the redshift is not measured yet. But an argument against this conclusion is, that no interaction region is visible, were the jet is decelerated. Another option to explain the asymmetry is an asymmetric jet model like the flip-flop model by Rudnick & Edgar (1984). Yet another theory could be, that the jet is bend, such that the hotspot is hide behind the radio-core. An indication for this theory is that in the spectral-index map the core is surrounded by a region with spectral-index  $\alpha \approx -0.5$ . To test this theory a spectral-index map with a tapered 15 GHz image must be created for reason of artifacts and the core-flux must be subtracted from the images to test if there is emission around the core.

With the modelfit of the south-eastern hotspot at  $\nu = 15.1$  GHz of 0521-365, getting

a major axis of  $\theta_{\text{maj}} = 0.61$  arcsec and a core-distance of  $d_{\text{core}} = 8.55$  arcsec a projected opening angle of  $\varphi_{\text{p}} = 4.11^\circ$  can be calculated. With information the inclination angle can be constrained using the intrinsic opening angles of radio-galaxies with hotspot by [Jeyakumar & Saikia \(2000\)](#). The most probable value then is  $\vartheta_{\text{mp}} = 37.50^\circ$  and the minimal one  $\vartheta_{\text{min}} = 19.93^\circ$ .

This result leads to the assumption, that the source is an intermediate object between a blazar and a radio galaxy. Also the spectrum of 0521-365 shown in [Fig.3.12](#) is not flat but steep in the whole radio regime, not flat in the high frequency regime as assumed for blazars. Calculating the extended luminosity of the source to be  $\log(L_{\text{ext}}/(\text{W Hz}^{-1})) \approx 26$ , which is in the FR2 regime, this and the small projected opening angle and the hotspot of the source leads to the assumption that the object could more be a FR2 than a FR1 like object or a hybrid object. A problem for the FR2 assumption is that the apparent speed calculated by [Rösch \(2016\)](#) to be  $\beta_{\text{app}} < 0.36$  and is not high-relativistic as assumed for FR2 objects. A solution for this discrepancy could be the so called spine-sheaf-model summarized by [Attridge et al. \(1999\)](#). In this model it is assumed that a spine in the inner part of the jet moves much faster than the outer sheaf of the jet. This effect causes only the slower outer sheaf typically to be observed in VLBI observations, but not the movement of the inner spine of the jet. But the much faster spine can cause high luminosities in the outer parts of the jet, for example when the plasma of the spine is shocked when colliding with the ambient medium resulting in a hotspot.

## 0537-441

For this study three data-sets are analyzed. The first two sets are obtained from an observation in 1987, observed at  $\nu = 1.4$  GHz and  $\nu = 4.8$  GHz simultaneous with the VLA in A-configuration. The second set contains data of an observation in 1998 with ATCA at its 6 km-configuration at  $\nu = 1.4$  GHz. Both observations are convenient to study the morphology at kilo-parsec scales. With the three images in [Fig.3.13](#) - [Fig.3.15](#), the source can be studied at different frequencies and resolutions, to study the envelopment of the morphology from the inner to the outer parts of the source. In the lowest resolution image at  $\nu = 1.4$  GHz with ATCA in [Fig.3.15](#) the source shows a bright radio core with a flux of  $S_{\text{core}} = 2.8$  Jy and an emission region extending in the south up to  $d_{\text{core}} \approx 50$  arcsec. The model for this southern region, together with the model of the core and all other important emission region of the two VLA images are summarized in [Tab.3.3](#). The whole source at the ATCA observation contains flux of  $S_{\text{source}} = 3.0$  Jy. Zooming further in the inner parts of the object, which is shown in the VLA image at  $\nu = 1.4$  GHz in [Fig.3.14](#) observed 11 years before, the core contains a fluxdensity of  $S_{\text{core}} = 4.2$  Jy, which is about 52% more than at the ATCA observation, but is consistent with the high variability of the source mentioned in [Sec.2.2](#). Besides the bright core two other emission regions are visible. The first one evolves in the north-western direction from the core up to  $d_{\text{core}} \approx 5$  arcsec the other one is located further out in the south-western direction. It seems that the jet is bend clock-wise. Comparing the image

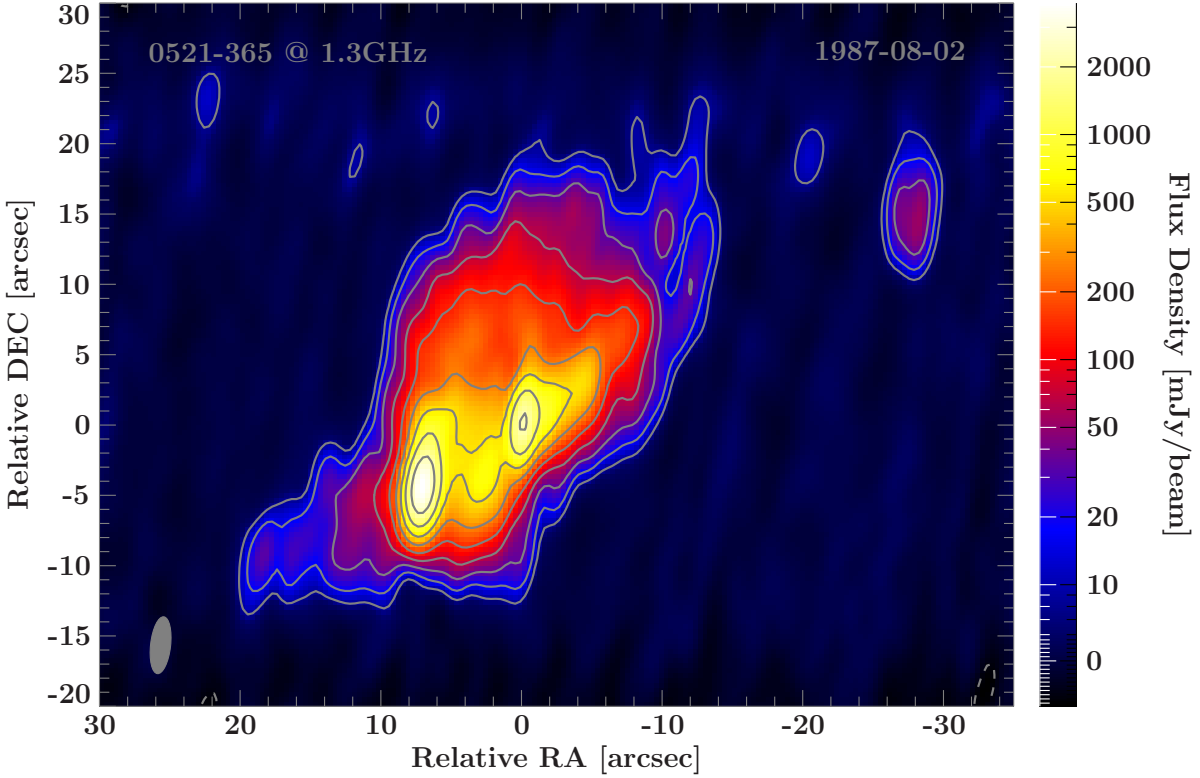


**Figure 3.10.:** VLA image of 0402-362 observed at 1.3 GHz in A-configuration. RMS: 2.8 mJy, map-peak: 3.84 Jy, beam:  $(4.05 \times 1.42)$  arcsec at  $-6.44^\circ$ . Smallest contourlevel at three times RMS for positive and negative fluxdensities. The other contours changing exponential with base 2 in the positive fluxdensity regime. A bright core is visible, a jet extending in north-eastern direction and a bright spot at  $d_{\text{core}} = 8.4$  arcsec in southern direction is visible. Also an extension in south-western direction identifiable. The source is surrounded by a bright halo. The overall size of the source alongside the jet is about  $s \approx 35$  arcsec

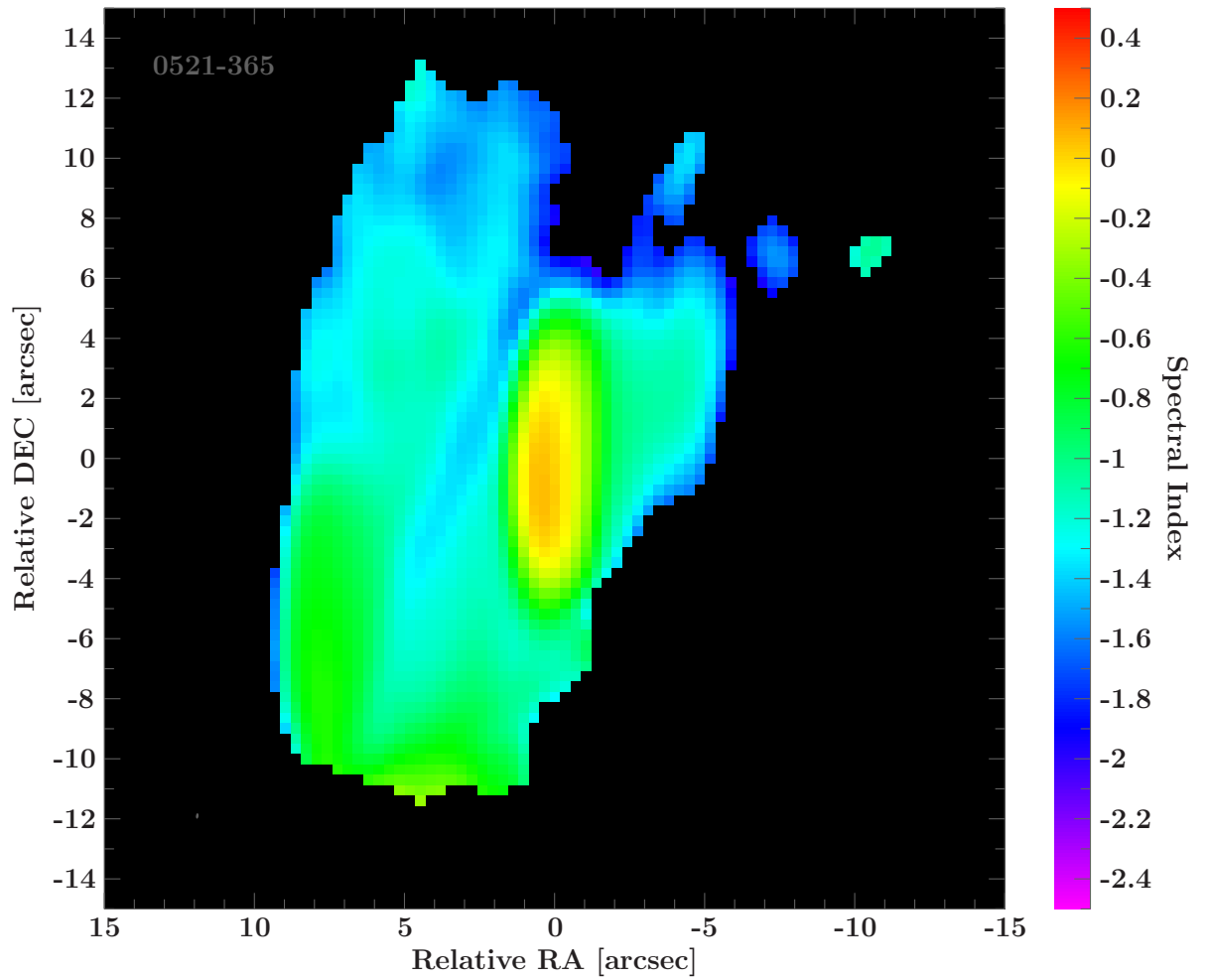


**Figure 3.11.:** Spectral map of 0521-365 between the VLA 1.5 GHz observation of figure 3.10 and the VLA 15 GHz observation of figure 2.3. Flat core region. Steepening in the hotspot down to  $\alpha \approx -0.6$  and in the jet and lobe down to  $\alpha \approx -1.5$ .

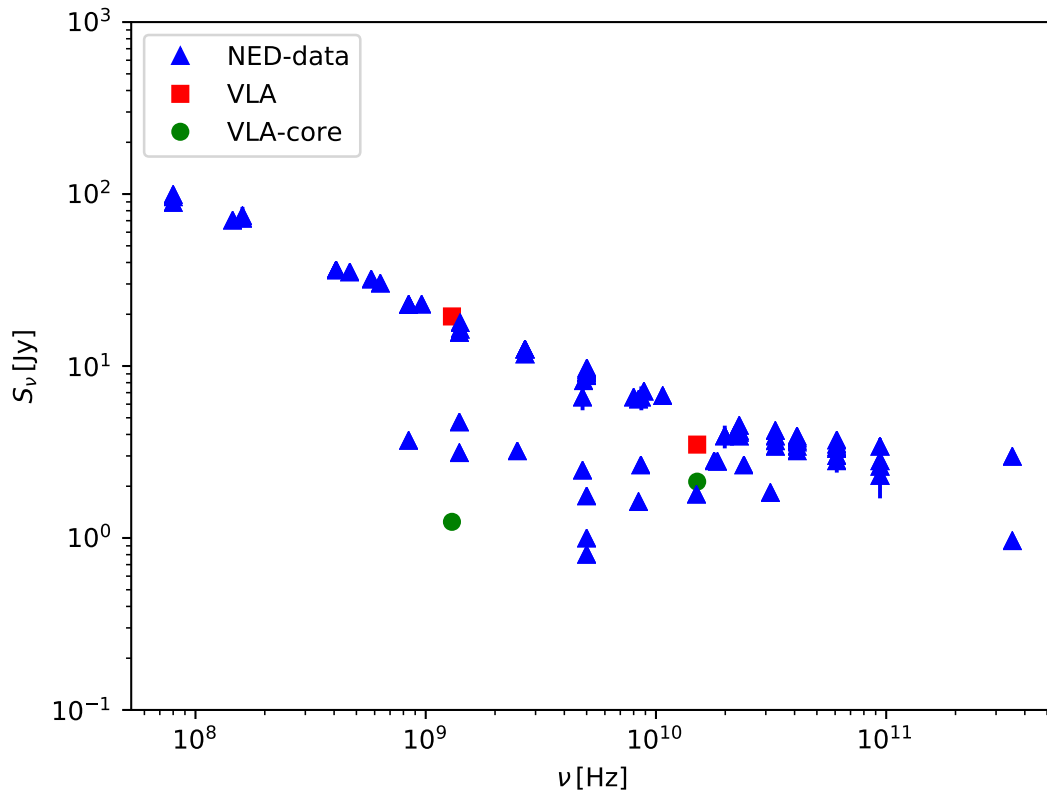


**Figure 3.12.:** Radio-spectrum of 0521 – 365 with the flux data of the NASA/IPAC Extragalactic Database (NED) as blue triangles and the flux measurements due to the analysis of the VLA image at  $\nu = 1.4$  GHz in figure 3.10 as red square and the core-fluxdensity as green circles.

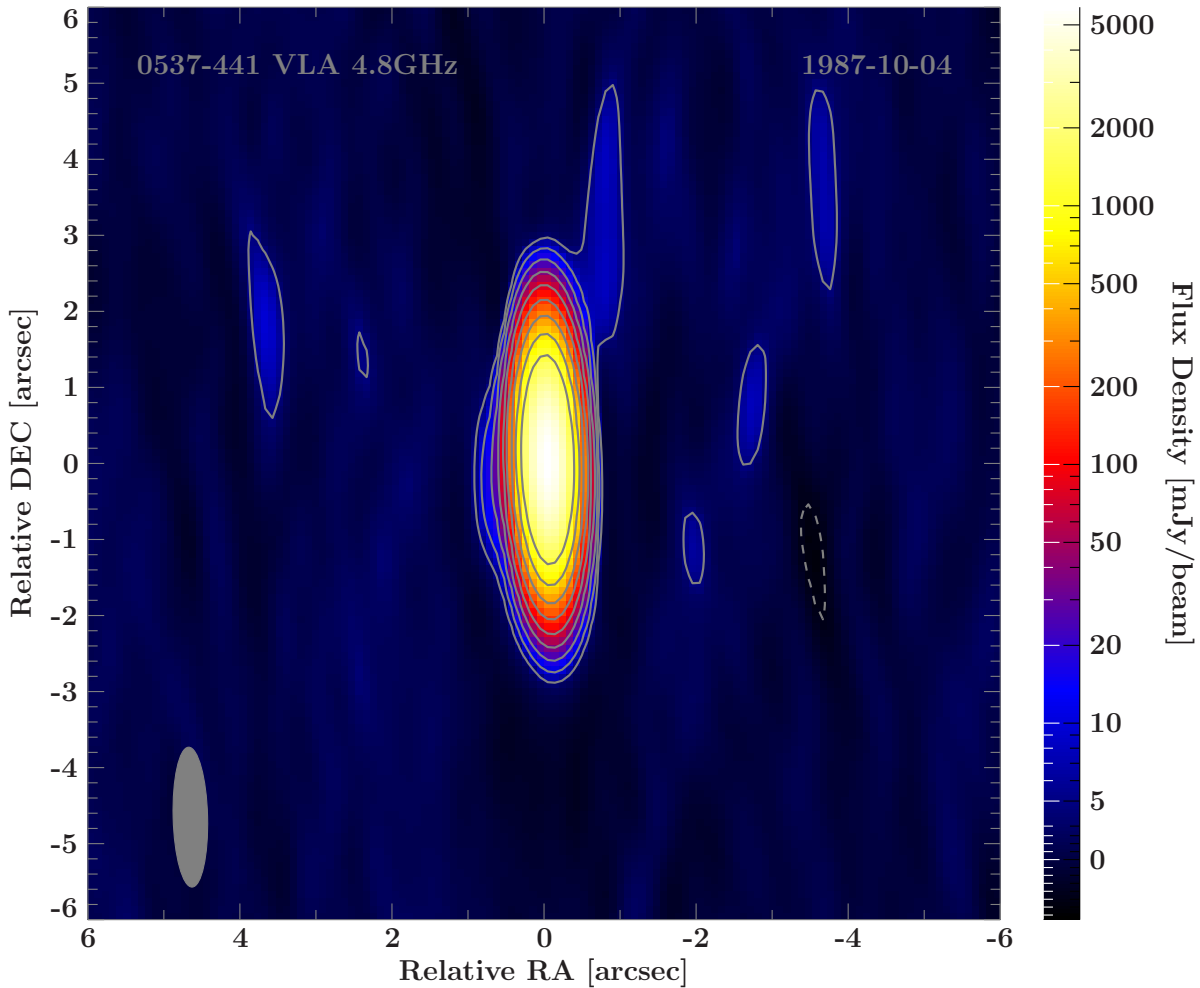
with the one obtained from the ATCA-observation no southern emission region is recognizable. But build up a tapered image with the VLA data to get an image with almost the same beam-size as in the ATCA-image the southern emission region is visible yet, which is shown in Fig.3.16. The region is now visible, because of the larger beam-size and the single components overlay with each other. The model for the core and the three extended emission regions are outlined in Tab.3.3.

Fig.3.13 contains the data of the VLA observation at  $\nu = 4.8$  GHz. Here only a bright core is visible, and a small extension in the eastern direction of the source. The other emission regions, visible at the 1.4 GHz observation, are also not visible because of the smaller beam-size of the image and the expected steep spectrum of the extended emission. In Fig.3.17 the spectral-index-map between the two VLA observations is presented. It is shown that the spectrum is steep in the two western emission regions just as the emission region in the east, exceptional with synchrotron-cooling. In the core region the spectrum is flat and in the west next to the core the spectrum is steep but with positive spectral index.

Comparing the morphology also with the TANAMI VLBI-observations in Fig.2.7, the jet seems highly bent with an almost helical structure. As discussed in Sec.2.2, 0537-441 changes between BL Lac and FSRQ status, according to the extended luminosity of  $\log_{10}(L_{\text{ext}}/(\text{W Hz}^{-1})) = 26.6$ , the object lays in the FR2-regime and should be according to the unification model more typical for FSRQs. The radio-spectrum plotted in Fig.3.18 is flat with high scattering in the higher frequency, which is consistent with the variability. The measured flux values are consistent with former spectrum obtained by NED. The flat spectrum is typical for high Doppler boosted jets in blazars. Also the high apparent jet-speed measured by Piner et al. (2007) of  $\beta_{\text{app}} = 53.7 \pm 23.1$  leads to to the assumption of a low inclination angle.

## 0625-354

In the images of figure 3.19 and 3.20, observed with the VLA with B-C-configuration at  $\nu = 1.4$  GHz and  $\nu = 4.8$  GHz, 0625-354 show a FR1-like morphology on kiloparsec-scales, whereas the source shows in the optical regime a BL Lac like spectral behavior as discussed in Sec.2.2. In the VLA image at  $\nu = 4.8$  GHz a kiloparsec-jet in the same direction as in the parsec-scale image in Fig.2.7 is visible. At a core-distance of about  $d_{\text{core}} \approx 20$  arcsec the jet opens rapidly in FR1-like complex structure. On the other side the counter-jet isn't significantly visible up to a core-distance of about  $d_{\text{core}} = 20$  arcsec because of Doppler-boosting effects, only emission of the counter lobe, then the jet opens in the same way like on the other side. The extension of the lobe and counter lobe of the jets reach distances of about  $d_{\text{core}} \approx 100$  arcsec on both sides. Both VLA observations are done simultaneous and in Fig.3.21 also a spectral-index map is shown. In the core-region the spectral index is about  $\alpha \approx 0$ , meaning the spectrum is flat, because of relativistic beamed synchrotron emission. In the outer parts the spectral index decrease down to  $\alpha \approx -1.5$ . The spectral indices in the outer parts lay in the typical regime



**Figure 3.13.:** VLA image of 0537-441 observed at 4.8 GHz in A-configuration. RMS: 1.6 mJy, map-peak: 6.10 Jy, beam:  $(1.84 \times 0.453)$  arcsec at  $1.44^\circ$ . Smallest contour level at three times RMS for positive and negative fluxdensities. The other contours changing exponential with base 2 in the positive fluxdensity regime. A bright core is visible and an extension in eastern direction.

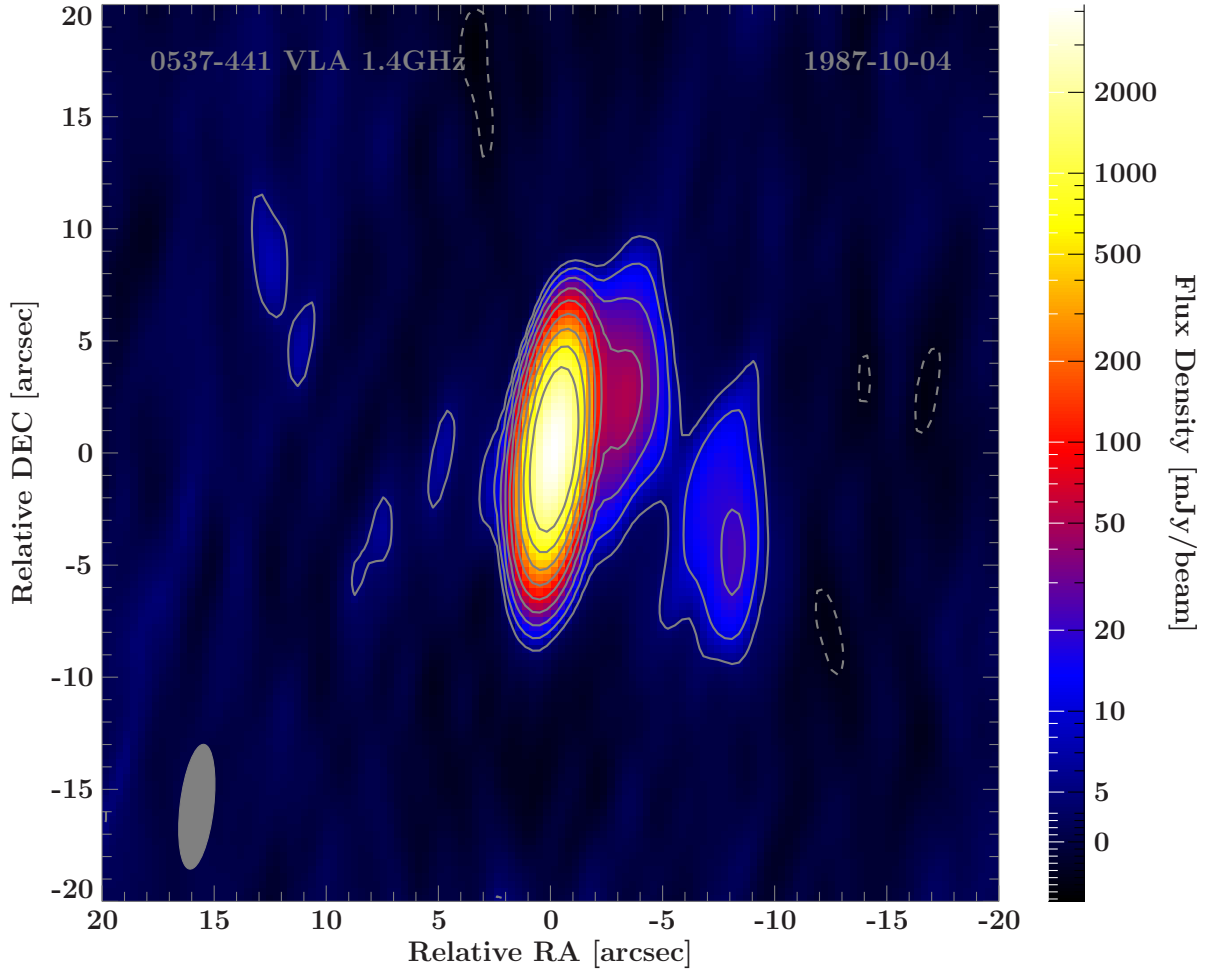


**Figure 3.14.:** VLA image of 0537-441 observed at 1.5 GHz in A-configuration. RMS: 2.0 mJy, map-peak: 4.22 Jy, beam:  $(5.56 \times 1.49)$  arcsec at  $-6.42^\circ$ . Smallest contourlevel at three times RMS for positive and negative fluxdensities. The other contours changing exponential with base 2 in the positive fluxdensity regime. A bright core is visible and a jet extending up to  $d_{\text{core}} \approx 5$  arcsec in north western direction, with a bending in southern direction up to  $d_{\text{core}} \approx 10$  arcsec

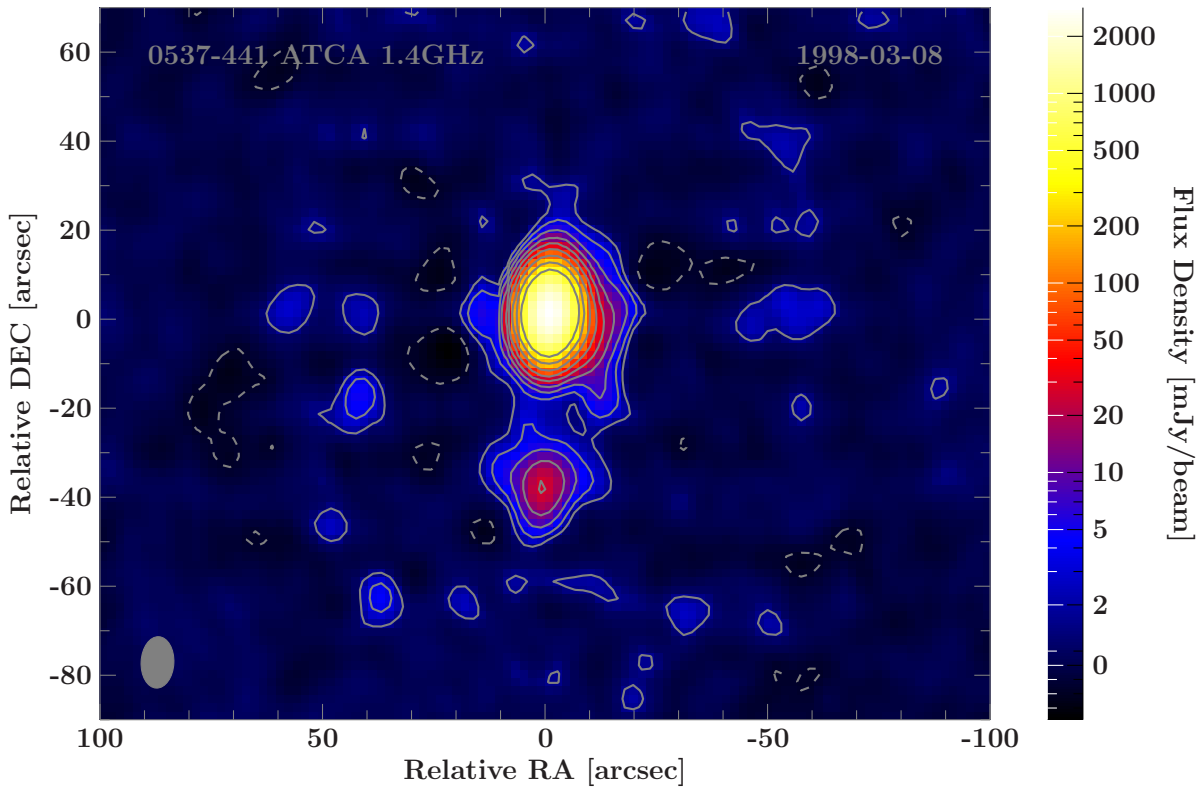


**Figure 3.15.:** ATCA image of 0537-441 observed at 1.5 GHz in standard 6 km configuration. RMS: 0.84 mJy, map-peak: 2.84 Jy, beam:  $(11.5 \times 7.36)$  arcsec at  $-2.85^\circ$ . Smallest contourlevel at three times RMS for positive and negative fluxdensities. The other contours changing exponential with base 2 in the positive fluxdensity regime. A bright core is visible and an emission region up to  $d_{\text{core}} \approx 50$  arcsec in southern direction.

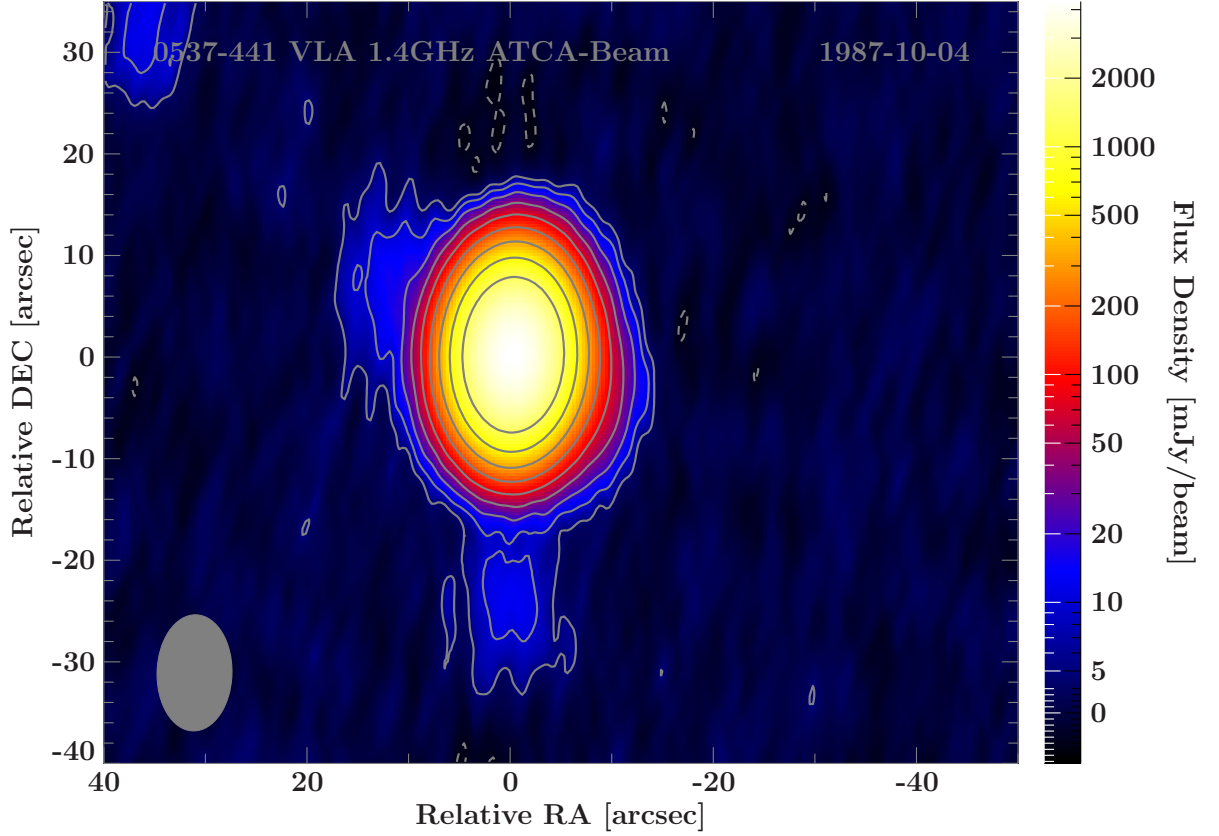


**Figure 3.16.:** Tapered VLA image of 0537-441 observed at 1.5 GHz in A-configuration. RMS: 1.6 mJy, map-peak: 6.10 Jy, beam:  $(11.5 \times 7.36)$  arcsec at  $-2.85^\circ$ . Smallest contourlevel at three times RMS for positive and negative fluxdensities. The other contours changing exponential with base 2 in the positive fluxdensity regime. A bright core is visible and an emission region up to  $d_{\text{core}} \approx 35$  arcsec in southern direction and on in north eastern direction up to  $d_{\text{core}} \approx 20$  arcsec

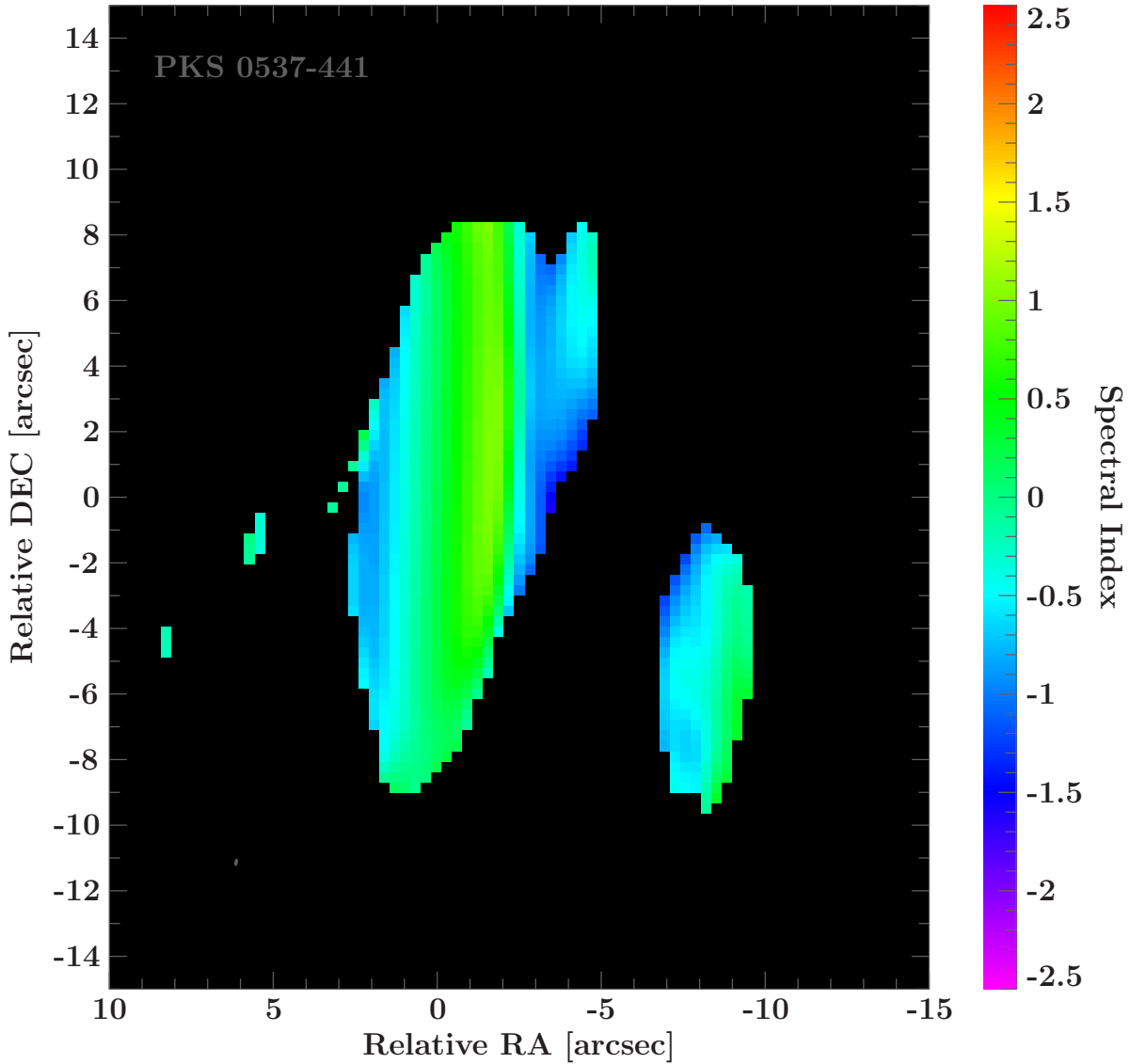


**Figure 3.17.:** Spectral map of 0537-441 between the VLA 1.5 GHz observation of figure 3.14 and the VLA 4.8 GHz observation of figure 3.13. Flat core region with changing between positive and negative spectral indices because of different observation times. Steepening in the outer regions down to  $\alpha \approx -1.5$ .

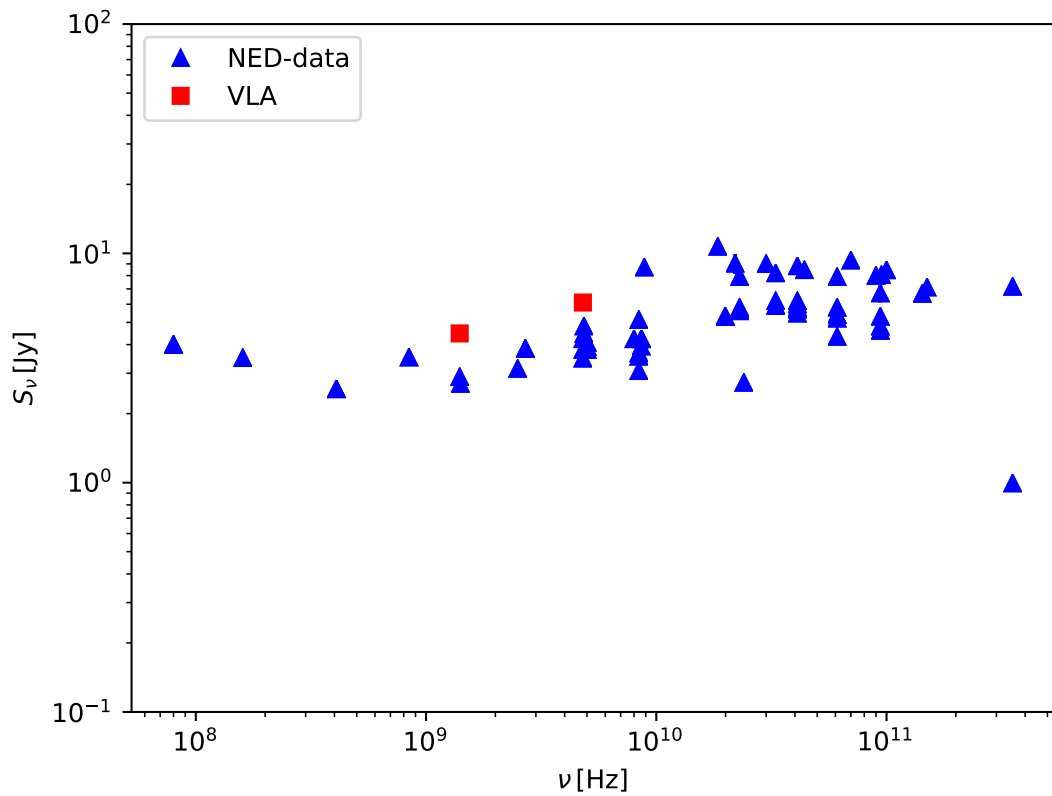


**Figure 3.18.:** Radio-spectrum of 0537 – 441 with the flux data of the NASA/IPAC Extragalactic Database (NED) as blue triangles and the flux measurements due to the analysis of the VLA images at  $\nu = 1.5$  GHz in figure 3.14 and at  $\nu = 4.8$  GHz in figure 3.13 as red squares.

**Table 3.3.:** Summary of the model-components of 0537 – 441. For each component the name (Comp.) the fluxdensity  $S_\nu$ , the core-distance  $d_{\text{core}}$ , the position-angle  $\theta$  and the major-axis  $\theta_{\text{maj}}$  is shown. The table is split in two parts. The first two rows shows the modelfit for the ATCA image. The other rows shows the object modeled with 4 extended model-components and the model for the unresolved core for the 1.4 GHz VLA observation.

Comp.	$S_\nu$ [mJy]	$d_{\text{core}}$ [arcsec]	$\theta$ [°]	$\theta_{\text{maj}}$ [arcsec]
core	2774.0	0	49.34	0.178
S	32.8	38.77	177.86	3.65
core	4219.2	0	80.87	0.028
E	16.5	1.354	87.53	1.691
N-W	96.7	4.187	-50.28	2.169
S-W	63.8	8.328	-117.30	3.478
S	16.7	24.006	179.85	4.840

of optical thin synchrotron emission according to Sec.1.1. The spectral index steepens going to the outer party because of synchrotron cooling of the plasma electrons. Because the lobe-emission in the outer parts is visible on both jet-sides the speed of the particles in these areas can be assumed not to be highly relativistic, which is in good resonance with observed jet-speeds at parsec-scales discussed in Sec.2.2, which is typical for FR1 morphology.

In the eastern emission region the jet, propagating in south-eastern direction, is visible and can be model-fitted. The jet emission is delimited according to the lobe emission, by comparing it with the area on the the counter-jet side, where no significant jet-emission is detectable. The area can be modeled with four Gaussian component summarized in Tab.3.4, together with the related apparent opening angles. Assuming a conical jet, the mean opening angle of the jet can be calculated to  $\varphi = (31.1 \pm 3.4)^\circ$ . Based on the FR 1 morphology the inclination angle of the source can be constrained, using the FR 1 statistic. The minimal inclination angle can be calculated to  $\vartheta_{\text{min}} = 6.13^\circ$  and the most probable one to  $\vartheta_{\text{mp}} = 20.06^\circ$ . The maximal inclination angle can not be constrained and can reach values up to  $\vartheta_{\text{max}} = 90^\circ$ , because the maximal opening angle of the statistic is greater than the measured one. Venturi et al. (2000) measure a maximal inclination angle between  $43^\circ < \vartheta < 61^\circ$ , which is consistent with the results above. This leads to the assumption that 0625-354 is a transitory object between FR1 radio-galaxy and BL Lac object, resulting in the FR1-like morphology, where the lobe and counter-lobe can still be separated, but the optical spectrum according to Wills et al. (2004) is more BL

Lac like whereas the radio spectrum shown in Fig.3.22 is steep and more typical for a radio galaxy.

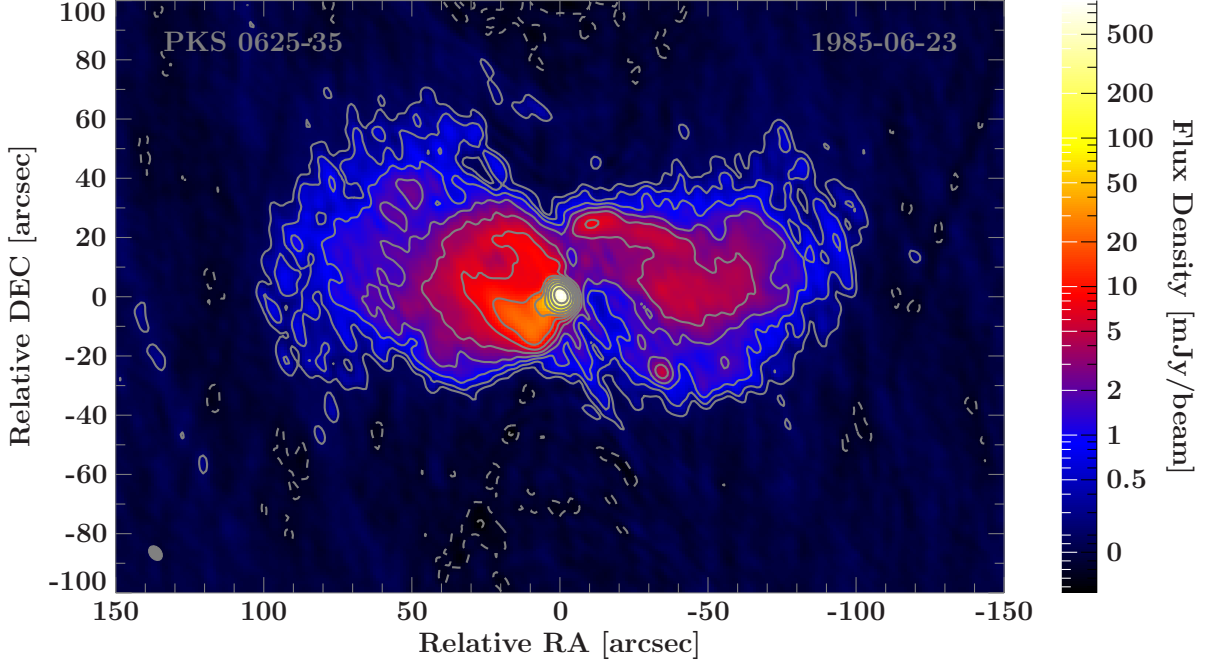


**Figure 3.19.:** VLA image of 0625-354 observed at 4.9 GHz in C-configuration. RMS: 0.13 mJy, map-peak: 0.844 Jy, beam:  $(5.45 \times 3.94)$  arcsec at  $39.2^\circ$ . Smallest contourlevel at three times RMS for positive and negative fluxdensities. The other contours changing exponential with base 2 in the positive fluxdensity regime. A bright core is visible and a FR1 like extended emission with an overall size of  $s \approx 200$  arcsec.

## 1104-445

The obtained VLA image in figure 3.23 show a jet extending in N-E-direction, same direction as visible in the parsec scale image in Fig.2.7, up to 5 arcsec, show then a gap and ending with a hotspot-like structure at a core-distance of  $d_{\text{core}} = 20$  arcsec. At kiloparsec-scales also on the south-western-direction a hotspot-like emission region is visible at a distance of  $d_{\text{core}} = 7.73$  arcsec. The N-E hotspot is modelfitted with one component and the one in the S-W direction with two. The models are summarized in Tab.3.5. Knowing the redshift of the source also the sizes of the hotspots can be computed to be  $s_{\text{N-E}} = 7.97$  kpc and  $s_{\text{S-W}} = 6.43$  kpc. These sizes lare consistent with hotspot sizes of FR2 radio galaxies studied by Jeyakumar & Saikia (2000). According to the opening angles of these hotspots the inclination angles could be constrained. These values are summarized together with the projected opening angles also in Tab.3.5. As shown in the table the inclination angle of the counter-hotspot is much smaller than the

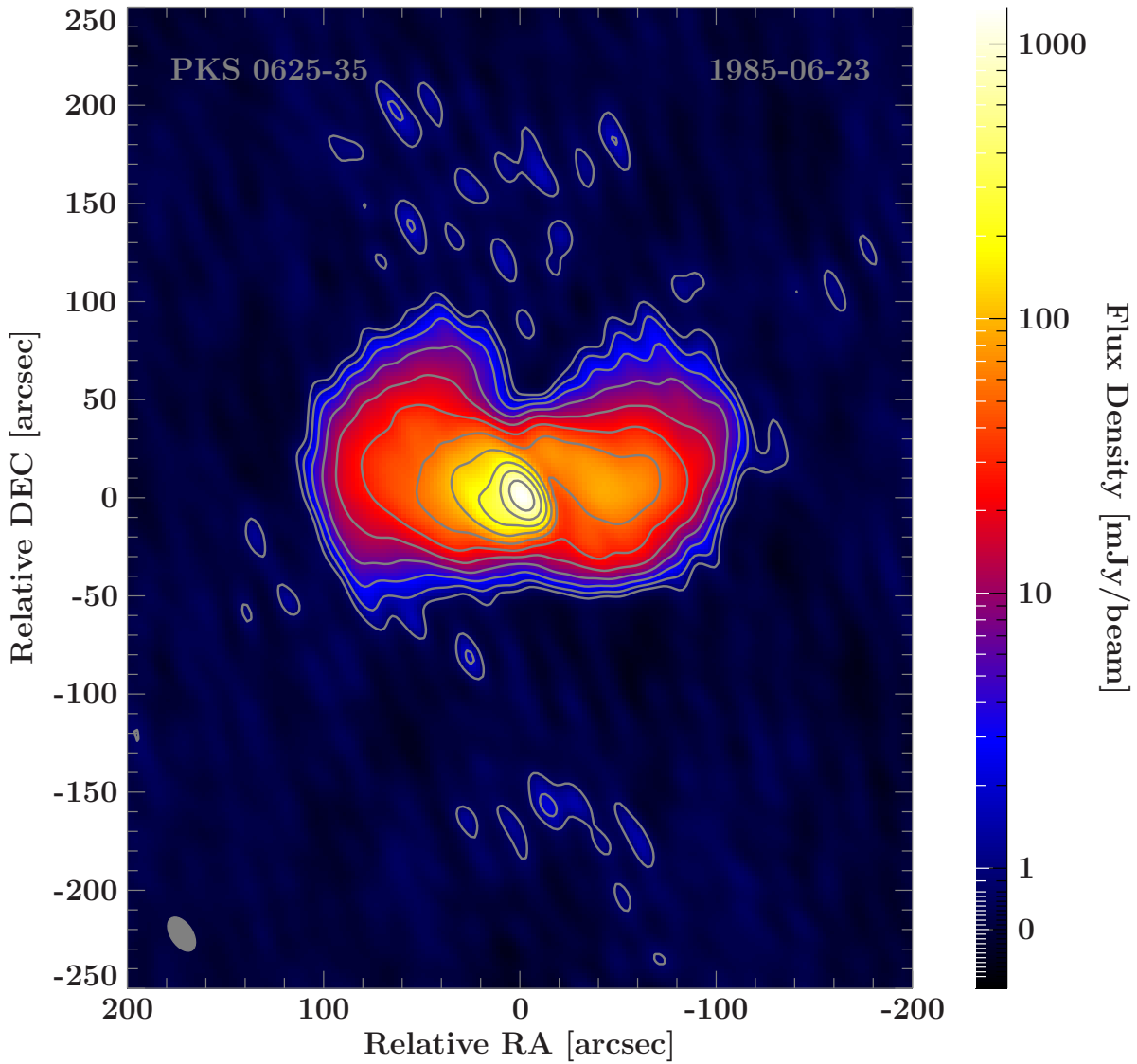


**Figure 3.20.:** VLA image of 0625-354 observed at 1.5 GHz in C-configuration. RMS: 0.33 mJy, map-peak: 1.36 Jy, beam:  $(19.5 \times 11.5)$  arcsec at  $39.2^\circ$ . Smallest contourlevel at three times RMS for positive and negative fluxdensities. The other contours changing exponential with base 2 in the positive fluxdensity regime. A bright core is visible and a FR1 like extended emission with an overall size of  $s \approx 200$  arcsec.

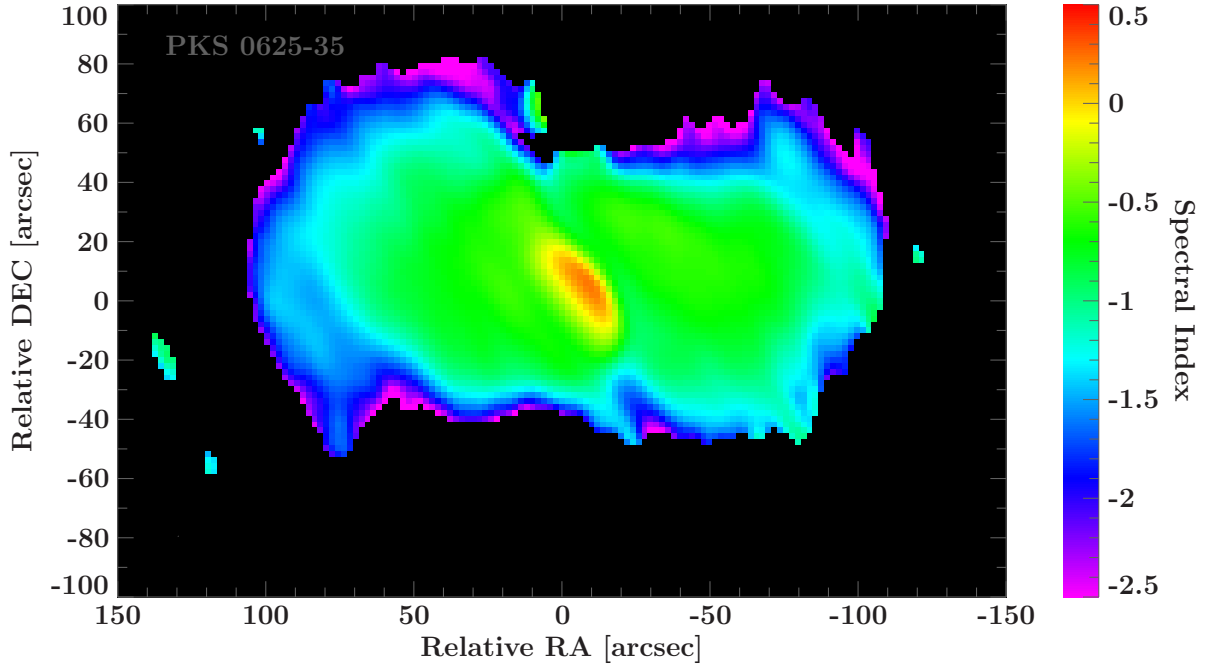


**Figure 3.21.:** Spectral index map of 0625-354 between the VLA observations at 1.5 GHz in figure 3.20 and the 4.9 GHz VLA observation in figure 3.19. Flat core region. Steepening in the plumes to  $\alpha \approx -2.5$

**Table 3.4.:** Summary of the model-components of the jet region of 0625 – 354. For each component the name (Comp.) the fluxdensity  $S_\nu$ , the core-distance  $d_{\text{core}}$ , the position-angle  $\theta$ , the major-axis  $\theta_{\text{maj}}$  and the apparent jet opening angle  $\zeta'$  is shown.

Comp.	$S_\nu$ [mJy]	$d_{\text{core}}$ [arcsec]	$\theta$ [°]	$\theta_{\text{maj}}$ [arcsec]	$\zeta'$ [°]
core	793.5	0.089	4.96	0.656	n.a.
jet 1	218.7	2.703	147.84	1.413	29.29
jet 2	42.8	7.165	117.22	3.221	25.33
jet 3	154.3	13.772	136.31	10.269	40.89
jet 4	96.4	19.605	100.28	10.076	28.82

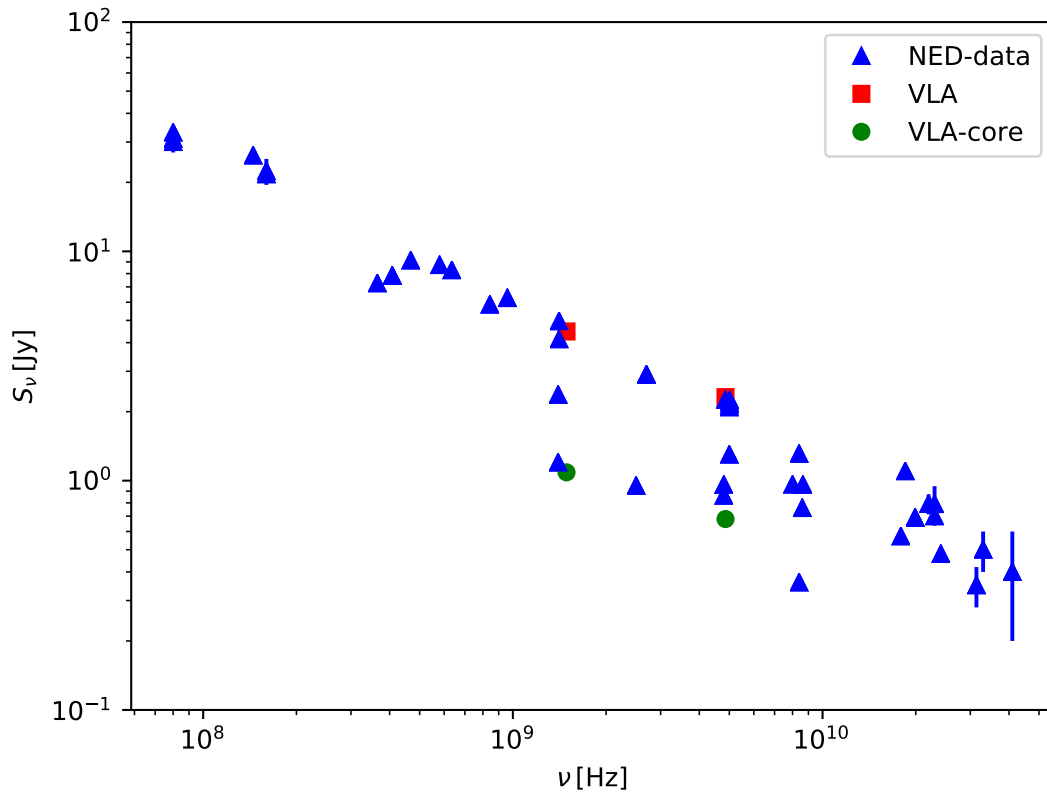


**Figure 3.22.:** Radio-spectrum of 0625 – 354 with the flux data of the NASA/IPAC Extragalactic Database (NED) as blue triangles and the flux measurements due to the analysis of the VLA images at  $\nu = 1.5$  GHz in figure 3.20 and at  $\nu = 4.8$  GHz in figure 3.19 as red squares and the core-fluxdensities for both frequencies as green circles.

one of the hotspot with a misalignment of  $\alpha_{\text{mp}} = 47.39^\circ$  for the most probable case and  $\alpha_{\text{min}} = 17.96^\circ$  for the minimal one.

To calculate the mean opening angle of the hole source the two hotspots are connected crosswise and the opening angle is the angle between the two connecting lines. The apparent opening angle then is  $\zeta' = 3.48^\circ$  and the inclination angle can be calculated to  $\vartheta_{\text{mp}}$  for the most probable case and to  $\vartheta_{\text{min}} = 23.68^\circ$  for the lower limit. To proof the plausibility of the measured apparent speed, the expansion of the source in the VLA image is measured by calculating the distance between the two hotspots with the modelfit parameters in Tab.3.5. By assuming a Hubble-constant of  $H_0 = 73 \frac{\text{km}}{\text{sMpc}}$  the projected distance between the hotspots is  $d_h = 236 \text{ kpc}$ . Deprojecting the size, the real size of 1104-445 can reach values of up to  $s = 588 \text{ kpc}$ . Comparing this size of the source, with the study of the largest NVSS-sources by Lara et al. (2001), where the sizes range between  $236 \text{ kpc} < s < 3739 \text{ kpc}$ , the size of 1104-445 is consistent with the sizes of typical radio-galaxies. A problem arises comparing the large inclination angle of the jet with the apparent jet speed of  $\beta_{\text{app}} = 57.67 \pm 9.58$  measured by Trüstedt (2013). As presented in Fig.3.25 assuming that the internal Lorentz-factor is equal to the apparent jet-speed,  $\gamma = \beta_{\text{app}}$ . In this case the measured  $\beta_{\text{app}}$  is the maximum of the apparent jet-speed distribution with respect to the inclination angle. With this assumption the inclination angle should be  $\vartheta = 1.0^\circ$ . For a higher inclination angle the internal Lorentz-factor must rise highly. But also assuming the limiting case for the internal Lorentz factor  $\gamma \rightarrow \infty$  and taking the error of the measured apparent speed by Trüstedt (2013) into account, the absolute upper limit for the inclination angle for this method is  $\vartheta_{\text{up}} = 2.38^\circ$ , shown in Fig.3.25, which is also far away from value by the method using the opening angle of the jet. Deprojecting the size of the source using the inclination angle produced by the apparent jet-speed the size becomes  $s_{\text{mp}} = 13.527 \text{ Mpc}$  for the most probable case and the absolute lower limit of  $s_1 = 5.685 \text{ Mpc}$  for the case of the upper limit inclination angle. Both values excite the range of source sizes of the largest radio galaxies measured by Lara et al. (2001) with a maximal size of  $s = 3.739 \text{ Mpc}$ . The lower limit for an inclination angle for the source assuming that the size do not excite the maximum value of Lara et al. (2001) can be calculated to  $\vartheta = 3.63^\circ$ . This leads to the conclusion, that the calculated apparent speed by Trüstedt (2013) is way to high and could reach maximal the value of  $\beta_{\text{app}} = 31.56$  assuming the statistic of Lara et al. (2001) or AGN can reach much higher extensions as measured so far. A hint that the measuring of the jet speed gives figure 3.24 from Trüstedt (2013), in which it is possible that the last two epochs of comp 1 can also be associated with a backward moving comp 2. Taking these epochs not into account the apparent jet speed would be lower. If the measured apparent speed is not true the calculated inclination angle with the method of opening angles seems reliable. With the upper limit of  $\vartheta = 23.68^\circ$  a maximal apparent jet speed of  $\beta_{\text{app}} = 4.77$  can be calculated.

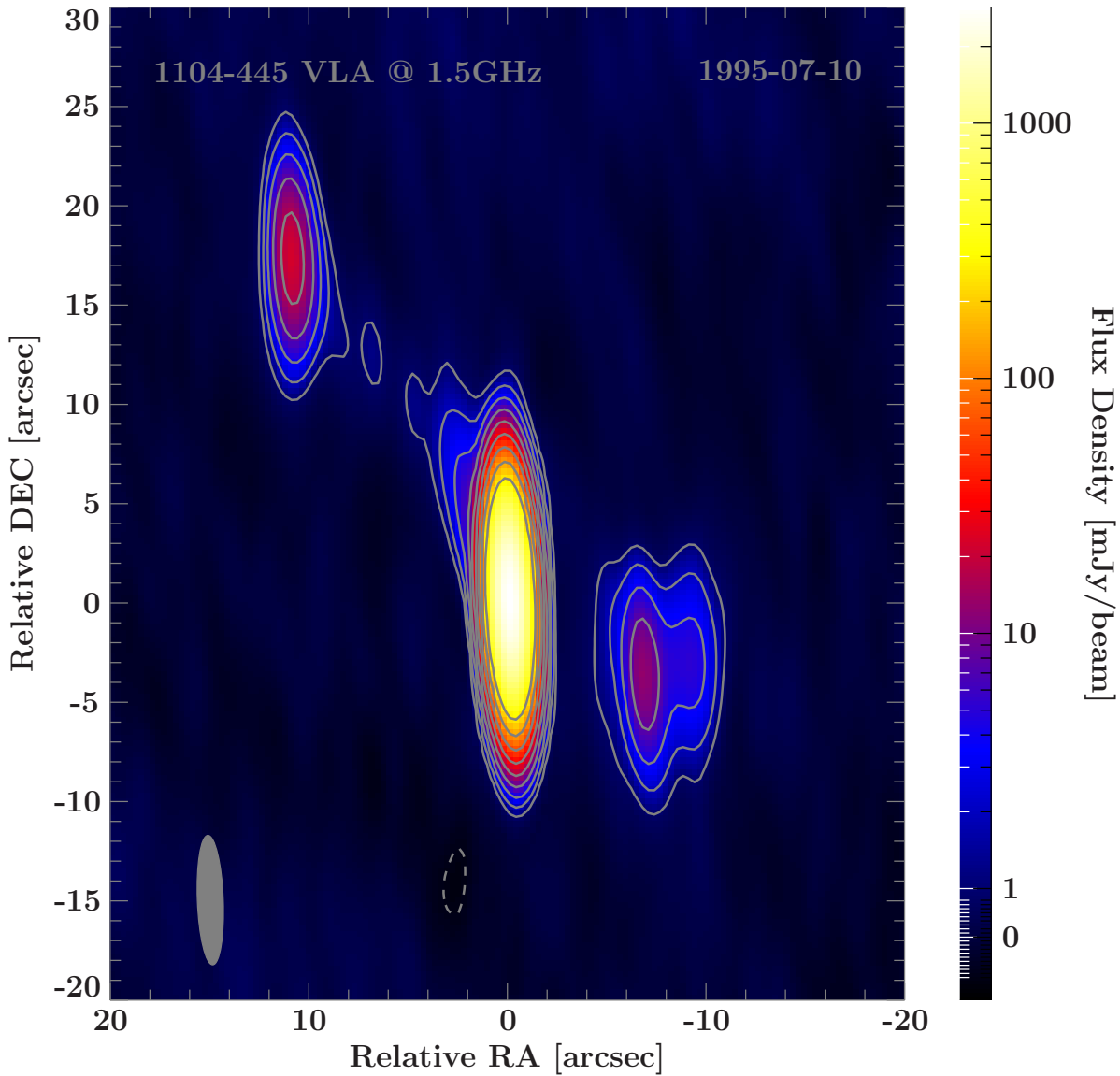


**Figure 3.23.:** VLA image of 1104-445 observed at 1.5 GHz in A-configuration. RMS: 0.37 mJy, map-peak: 2.85 Jy, beam:  $(6.5 \times 1.3)$  arcsec at  $1.44^\circ$ . Smallest contourlevel at three times RMS for positive and negative fluxdensities. The other contours changing exponential with base 2 in the positive fluxdensity regime. A bright core is visible and an extension in nort eastern direction. Also two hotspot-like emission regions are visible at One in north eastern direction and one in south western direction.

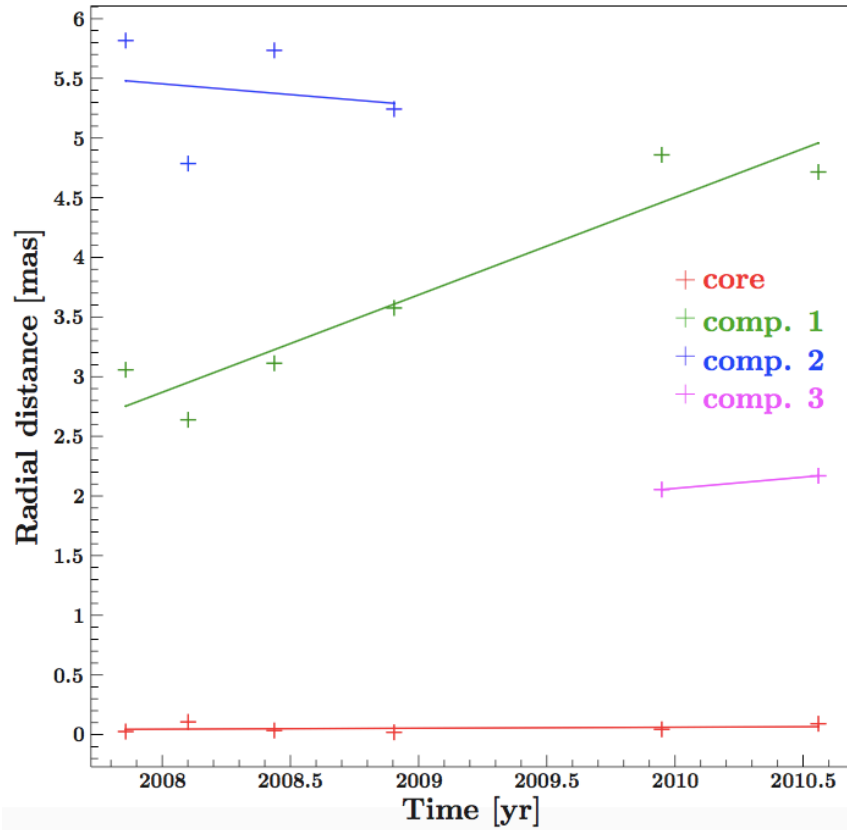


**Figure 3.24.:** Time evolution of the associated components of figure ?? with linear fit for the evolution of every component. The components are coded in the same color like in figure ?. By [Trüstedt \(2013\)](#)

**Table 3.5.:** Summary of the model-components of 1104 – 445. For each component the name (Comp.) the fluxdensity  $S_\nu$ , the core-distance  $d_{\text{core}}$ , the position-angle  $\theta$ , the major-axis  $\theta_{\text{maj}}$ , the projected opening angle  $\zeta'$  and the most probable  $\vartheta_{\text{mp}}$  and minimal inclination angle  $\vartheta_{\text{min}}$  is shown.

Comp.	$S_\nu$ [mJy]	$d_{\text{core}}$ [arcsec]	$\theta$ [deg]	$\theta_{\text{maj}}$ [mas]	$\zeta'$ [deg]	$\vartheta_{\text{mp}}$ [deg]	$\vartheta_{\text{min}}$ [deg]
core	2850	0.00	-162.21	7.35			
N-E	27.36	20.41	32.67	925.27	2.60	74.26	32.62
S-W <sub>1</sub>	13.72	7.73	-119.34	746.07	5.53	26.87	14.66
S-W <sub>2</sub>	8.00	9.38	-110.03	1888.11			

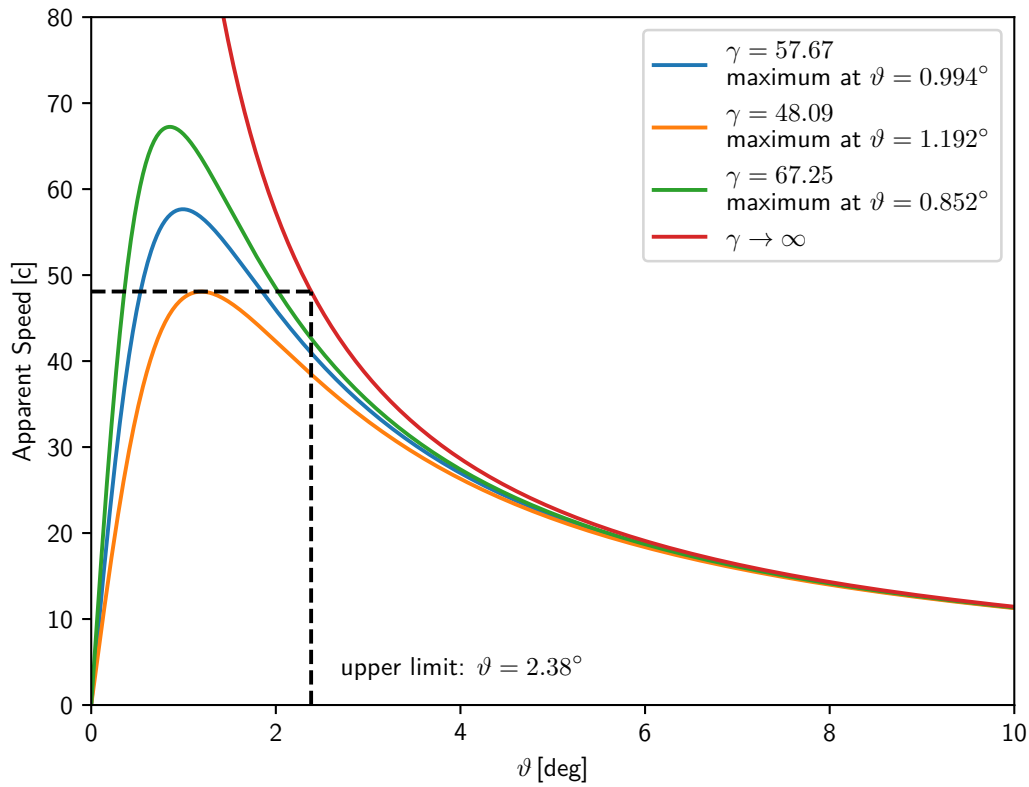


**Figure 3.25.:** Apparent jet speed as function of the inclination angle  $\vartheta$ . The function is presented with Lorentz-factors equal to the most probable, the minimal and the maximal apparent jet speed measured by Trüstedt (2013) and also with  $\gamma \rightarrow \infty$ .

### 1313-333

In the VLA image at  $\nu = 1.4$  GHz the source exhibits a bright core with a fluxdensity of  $S_{\text{core}} 1.0$  Jy and an extension in the south-eastern direction up to  $d_{\text{core}} \approx 3$  arcsec, which is almost the opposite direction as in the VLBI-image, meaning the jet is bent between parsec and kiloparsec-scales as so that the jet crosses the line of sight. 1313 – 333 can be modeled with three Gaussian components, one core-component, one in the south-eastern direction and the last one in the northern direction, which is not visible in the image because of the poorer resolution in the north-south-direction. The model is summarized in Tab.3.6. The two outer components could be parts of the jet respectively the counter-jet or two hotspots ending the two jets. With these assumptions the inclination angles can be constrained with the method of the measured opening angles of the jets explained before, which are summarized also in Tab.3.6. The inclination angles have almost the same range with an most probable value of  $\vartheta_{\text{mp}} \approx 3.3^\circ$ , typically for blazars. According to the redshift and a flat cosmology the northern emission region has a size of  $s = 15.65$  kpc and the south-eastern region of  $s = 20.88$  kpc, which is a typical hotspot size according to Jeyakumar & Saikia (2000). The two jets are misaligned in the projection plane with an angle of  $\delta = 50.77^\circ$ . Deprojecting the measured lengths of the two jets the most probable size of the source is  $s_d = 821$  kpc, which is close to the most probable value of radio-galaxies of the study by Lara et al. (2001) of  $s_d = 906$  kpc.

### 2155-304

To study the multi-scale morphology, the description starts in the most inner part of the source observable with VLBI experiments and works out with several steps in between up to kiloparsec scales with an overview of the whole size of the object. At parsec scales, as presented in the TANAMI image in Fig.2.7, discussed in Sec.2.2, 2155-304 shows besides the bright core a jet extending in south-western direction. Zooming further out, which is done by observing the object with the VLA in A-configuration at  $\nu = 4.8$  GHz, the jet points in the same general direction as known from the VLBI observation. As seen in Fig.3.27 the jet extends up to a distance of  $d_{\text{core}} \approx$  and then disappears. In Fig.3.28 the image obtained from the VLA A-configuration observation at  $\nu = 1.4$  GHz is illustrated, which was observed simultaneously to the 1.4 GHz VLA image. Because of the lower resolution the jet in south-eastern direction appearing in the image before is not recognizable, but a component at a distance up to about  $d_{\text{core}} \approx 20$  arcsec on the other side of the core in north-western direction. This component is not visible in the 4.8 GHz image, because of the smaller beam, as discussed before, but construct a tapered image of the source at  $\nu = 4.8$  with almost the same beam obtained in the 1.4 GHz image, as displayed in Fig.3.29, the emission region is also visible in this observation. So out of the observations at the two different frequencies the spectral-index-map in Fig.3.32 can be calculated. The map shows a flat spectrum as in the core region and spectral indices between  $-1.5 \lesssim \alpha \lesssim -0.5$  in the north-western emission region and in the south-eastern

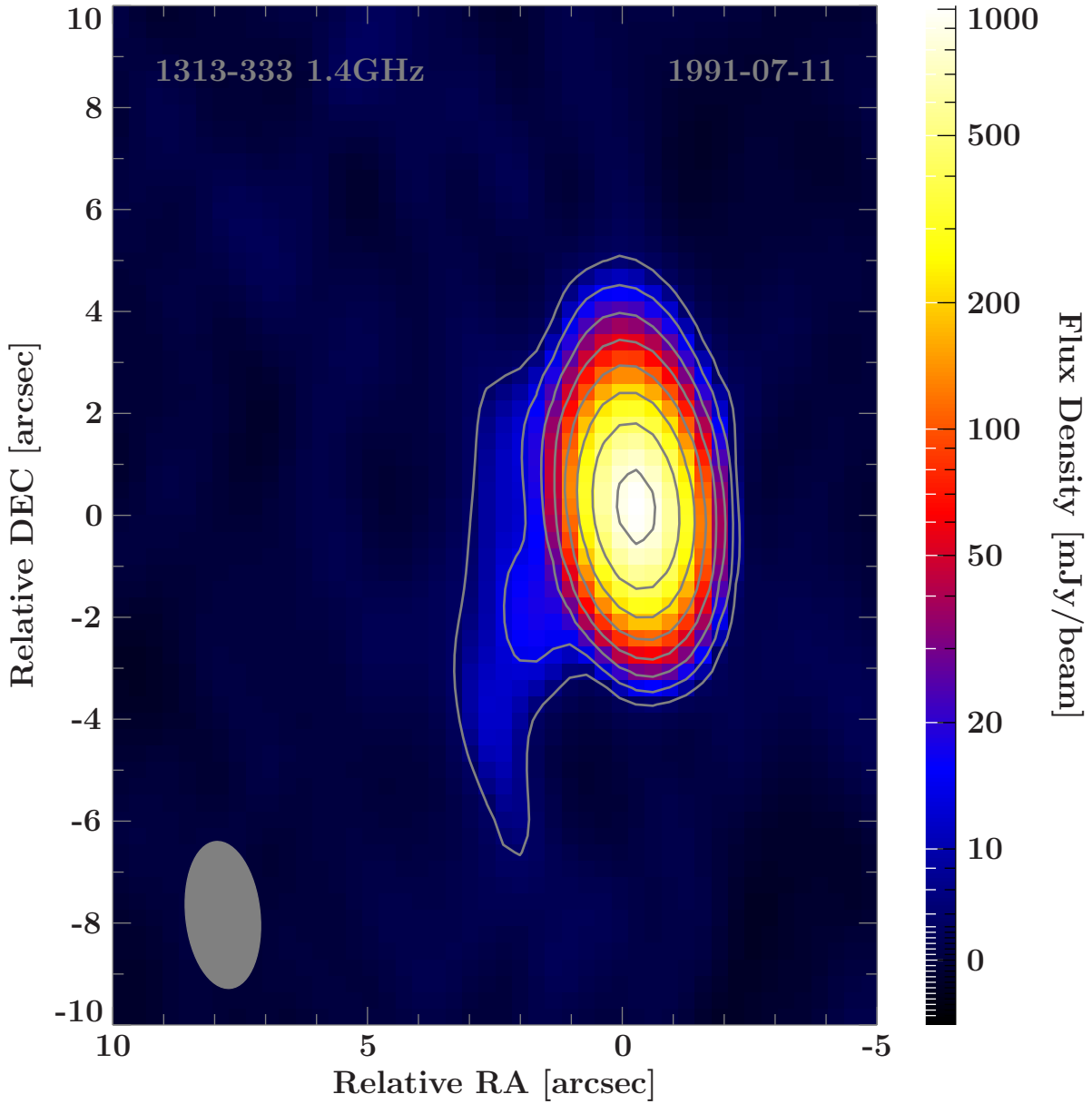


**Figure 3.26.:** VLA image of 1313-333 observed at 1.4 GHz in A-configuration. RMS: 2.2 mJy, map-peak: 1.02 Jy, beam:  $(2.89 \times 1.46)$  arcsec at  $5.85^\circ$ . Smallest contourlevel at three times RMS for positive and negative fluxdensities. The other contours changing exponential with base 2 in the positive fluxdensity regime. A bright core is visible and an extension in eastern direction.

**Table 3.6:** Summary of the model-components of 1313 – 333. For each component the name (Comp.) the fluxdensity  $S_\nu$ , the core-distance  $d_{\text{core}}$ , the position-angle  $\theta$ , the major-axis  $\theta_{\text{maj}}$ , the projected opening angle  $\zeta'$  and the most probable  $\vartheta_{\text{mp}}$ , minimal inclination angle  $\vartheta_{\text{min}}$  and the maximal inclination angle  $\vartheta_{\text{max}}$  is shown. The upper part show the model only for the unresolved core model and the lower one the model for the whole source.

Comp.	$S_\nu$ [mJy]	$d_{\text{core}}$ [arcsec]	$\theta$ [deg]	$\theta_{\text{maj}}$ [arcsec]	$\zeta'$ [deg]	$\vartheta_{\text{mp}}$ [deg]	$\vartheta_{\text{min}}$ [deg]	$\vartheta_{\text{max}}$ [deg]
core	989.98	0.00	-56.26	0.066				
core	1016.72	0.00	167.47	0.157				
S-E	37.07	3.24	133.45	2.47	41.68	3.29	1.84	26.99
N	52.61	2.38	4.21	1.79	41.20	3.33	1.86	27.36

jet, which is in agreement with synchrotron cooling, western next to the core the spectrum seems to be steepen with a positive spectral index. The spectrum in the eastern jet seems steeper as the western one. Besides the core-region and the north-western component also some diffuse halo appears in the 1.4 GHz image around and between the two components, but no bright emission regions which can be attributed to the jet, which should point in south-eastern direction according to Fig.2.7 and Fig.3.27, could be identified. So a possible explanation is that the jet is bent and because of the projection effect due to the high inclination angle of blazars, the jet crosses the line of sight and appears next up in the north-eastern component, which can be seen in Fig.3.28 and Fig.3.29. In the deprojected case the bending is only a few degree, which is typical for FR1-objects, as discussed by Seeg (2017). A fact that substantiate the bending theorem is the higher spectral index in the south-eastern jet, which could be the consequence of a shock leading to the jet-bending. Assuming that the south-eastern part of the jet evolves without any disturbance the inclination angle can be constrained. By measuring an apparent jet opening angle of  $\varphi_{po} = 62.52^\circ$  by modeling the emission region with one Gaussian component the inclination angle assuming an FR1 like opening angle can be calculated for the most probable case to be  $\vartheta_{mp} = 9.04^\circ$  and for the minimal one to be  $\vartheta_{min} = 2.80^\circ$ . This means that the jet must bend only more than the inclination angle of this part of the jet to cross the line of sight, which in the minimal case only  $\Delta\vartheta > 2.80^\circ$ . This estimation of the inclination angle works only for the simplification that the bending happens at one single point and not over a larger region in the jet and that the jet opens conical and only if the jet is not bent on the position of the model already. So the real bending angle should be in the regime of a few degree, which is possible in such kind of objects. Because of the low jet-speeds in the outer kiloparsec parts in the jet, the jet can easily bent. The typical jet-bending of FR1 objects in the outer parts was presented by Seeg (2017) with the sketch in figure 3.30, where the edge on view, here shown as a typical FR1 radio galaxy, is compared with the blazar picture for 2155 – 304. As shown both images of 2155-304 at  $\nu = 1.4$  GHz and  $\nu = 4.8$  GHz show different parts of the jet. A possible cause of the bending can be that the object moves in the cluster medium of a larger galaxy cluster. In the last radio image in figure 3.31 almost the whole source is visible with a size comparable with previous studies discussed in section 2.2. In the image the same FR1 like structure appears, also the prominent jet-component in the south-western direction shown in figure 3.28 can be identified.

The overall fluxdensity of the source at 1.4 GHz can be determined to be  $S_{source} = 434.9$  mJy and the core-fluxdensity can be estimated with an unresolved Gaussian model to  $S_{core} = 298.7$  mJy, so that the extended radio-luminosity can be calculated to  $L_{ext}/(W Hz^{-1}) = 24.59$ , which is on the border between the FR1 object and the transitory region between FR1 and FR2 objects. The spectrum shown in figure 3.33 is flat with a possible steepening below about  $\nu \approx 300$  MHz and a high scattering in high frequencies. The possible steepening in the lower frequency range is in accordance with the high extended emission already detectable at frequencies above  $\nu \approx 300$  MHz. This fact together with the FR1 like morphology and luminosity is an evidence that the source is a true beamed and

rotated counterpart of a FR1 radio galaxy.

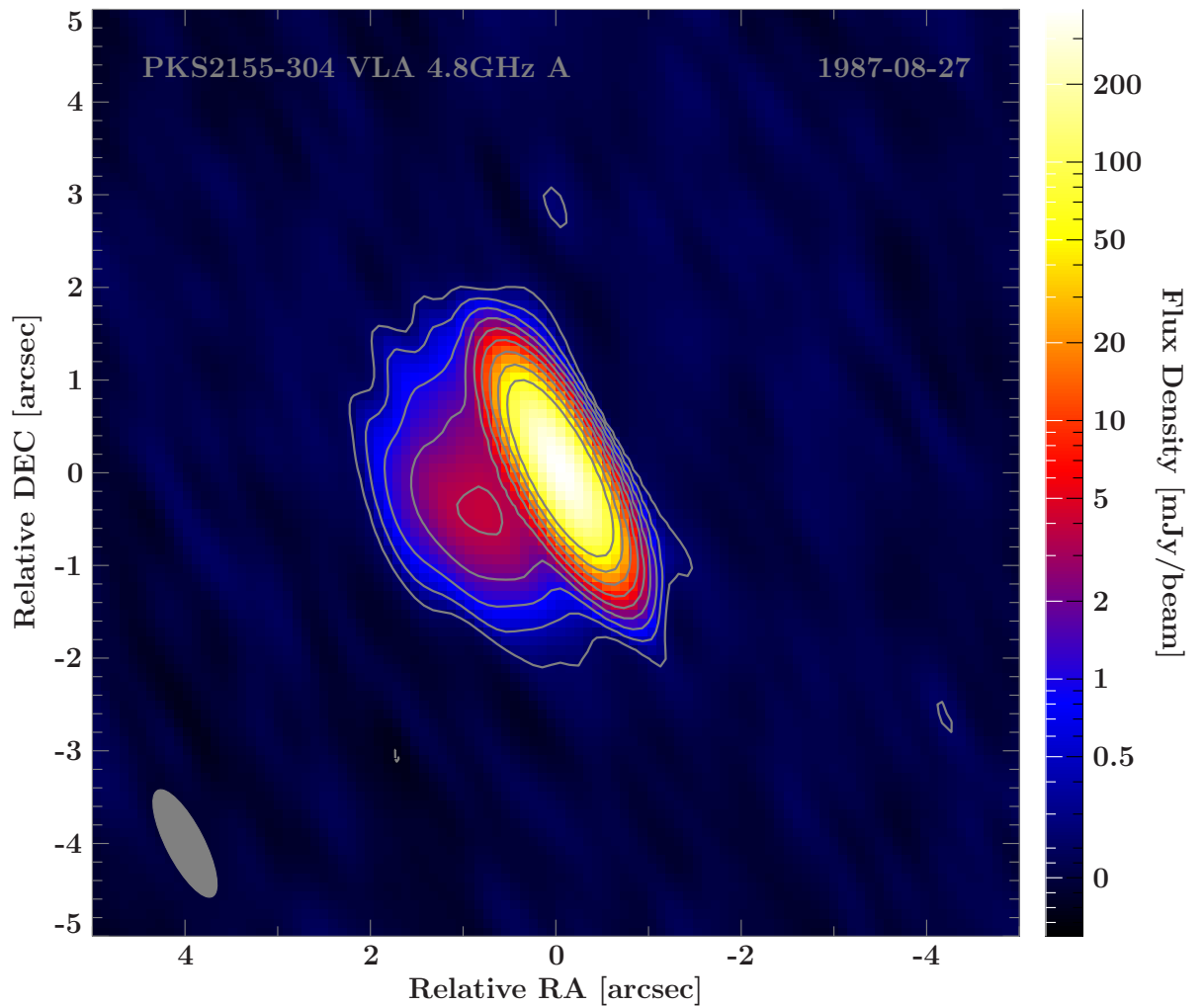


**Figure 3.27.:** VLA image of 2155-304 observed at 4.8 GHz in A-configuration. RMS: 0.084 mJy, map-peak: 0.389 Jy, beam:  $(1.29 \times 0.406)$  arcsec at  $27.3^\circ$ . Smallest contour level at three times RMS for positive and negative fluxdensities. The other contours changing exponential with base 2 in the positive fluxdensity regime. A bright core is visible and an extension in south eastern direction. up to about  $d_{\text{core}} \approx 2$  arcsec.

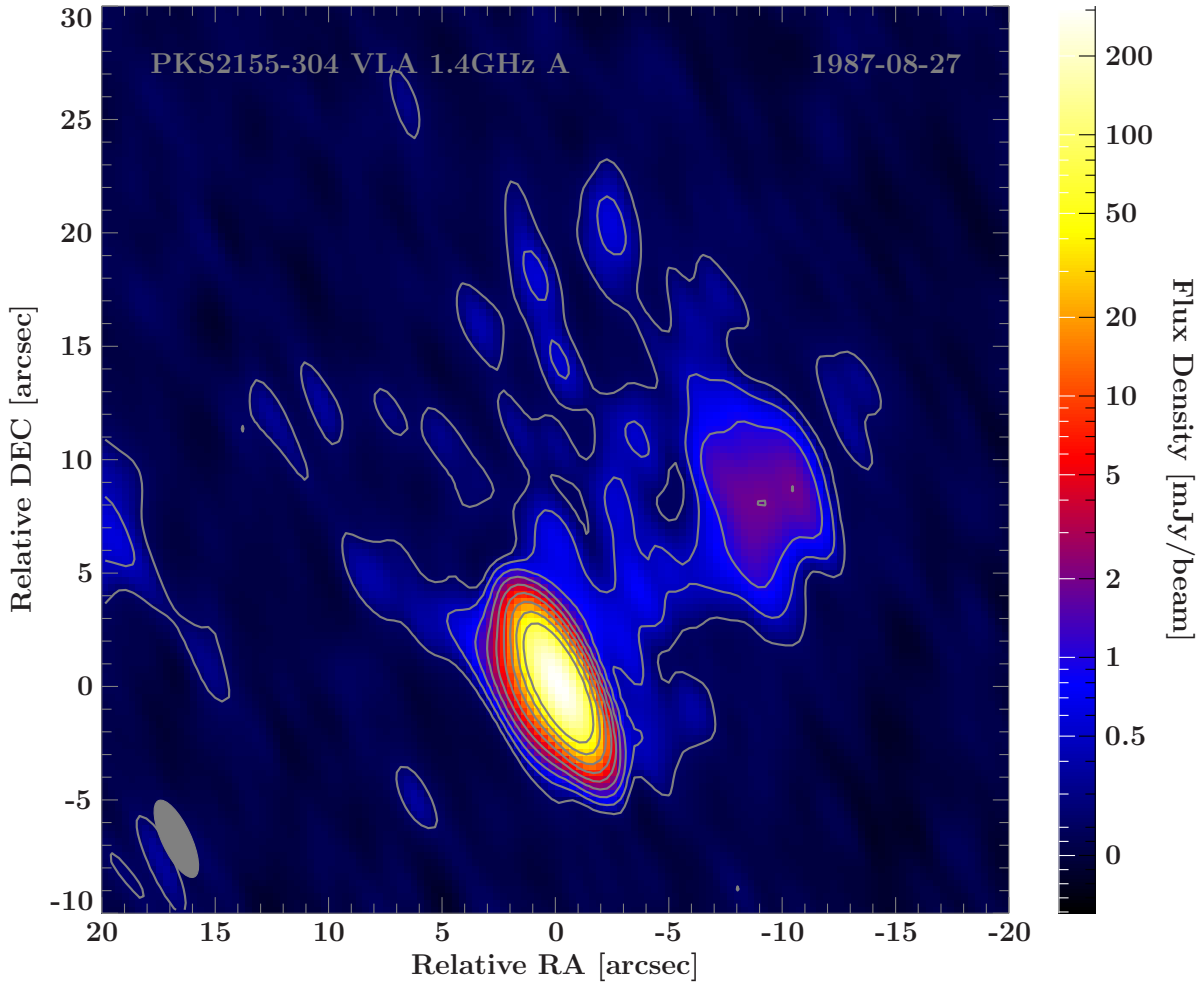


**Figure 3.28.:** VLA image of 2155-304 observed at 1.4 GHz in A-configuration. RMS: 0.078 mJy, map-peak: 0.312 Jy, beam:  $(3.71 \times 1.28)$  arcsec at  $25.2^\circ$ . Smallest contour level at three times RMS for positive and negative fluxdensities. The other contours changing exponential with base 2 in the positive fluxdensity regime. A bright core is visible and an emission region in north western direction. up to about  $d_{\text{core}} \approx 15$  arcsec.

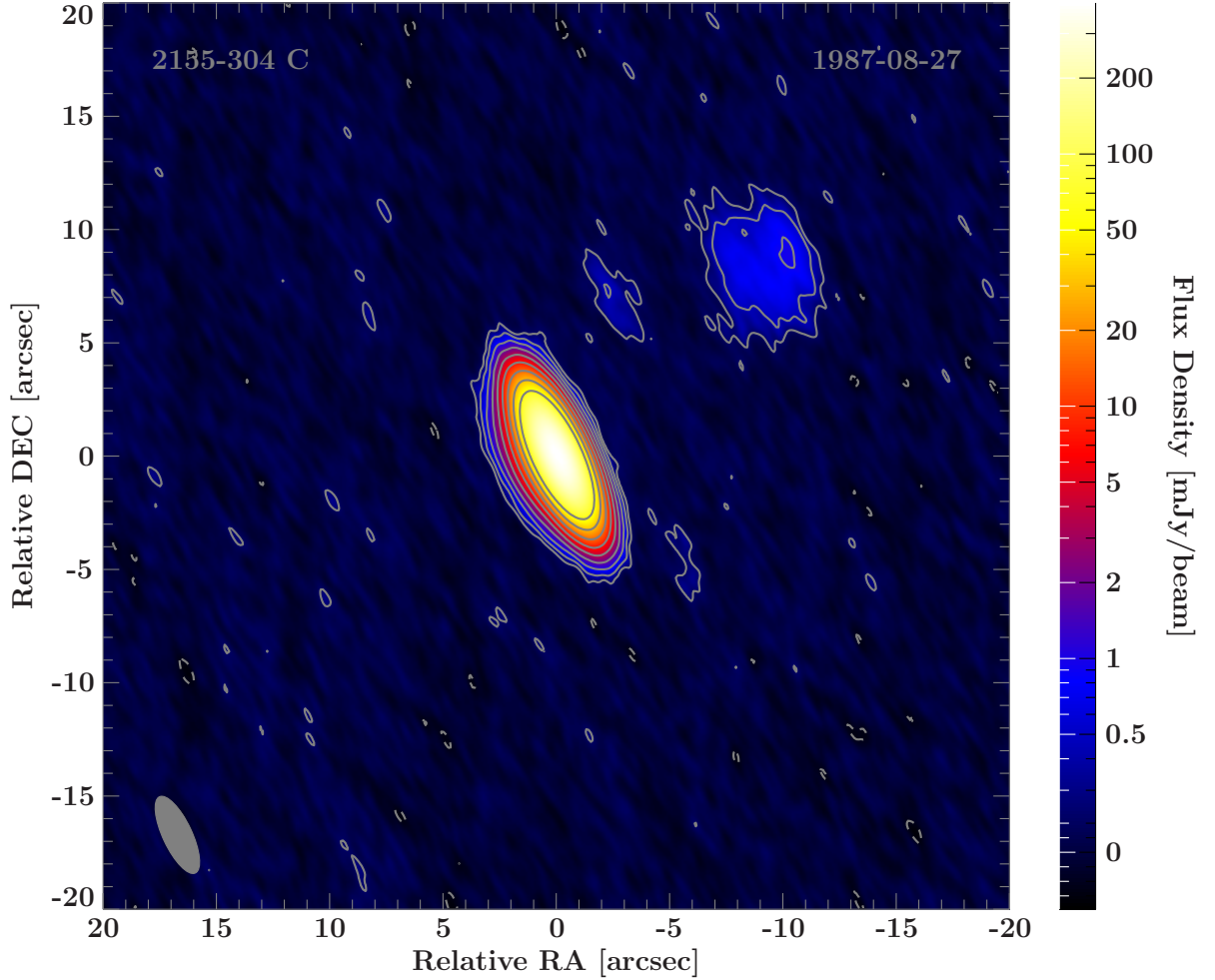


**Figure 3.29.:** Tapered VLA image of 2155-304 observed at 4.8 GHz in A-configuration. RMS: 0.084 mJy, map-peak: 0.389 Jy, beam:  $(3.71 \times 1.28)$  arcsec at  $25.2^\circ$ . Smallest contourlevel at three times RMS for positive and negative fluxdensities. The other contours changing exponential with base 2 in the positive fluxdensity regime. bright core is visible and an emission region in north western direction. up to about  $d_{\text{core}} \approx 15$  arcsec.

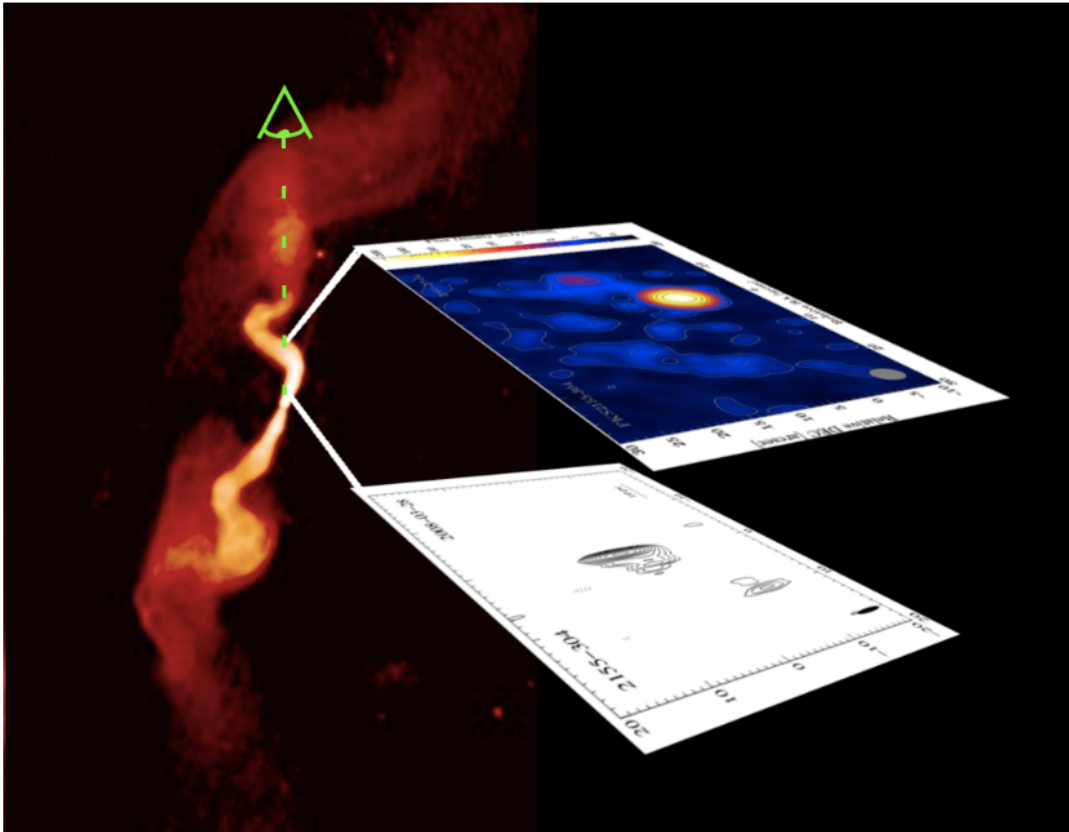


**Figure 3.30.:** The typical FR1 radio galaxy 3C31 (from: <http://www.cv.nrao.edu/>) is presented for the edge on view of an FR1 object, compared with the blazar view of an FR1 object for this case 2155 – 304 observed with the VLA at  $\nu = 4.8$  GHz and with the GMRT at  $\nu = 1.4$  GHz. As shown both images of 2155-304 show several parts of the jet.

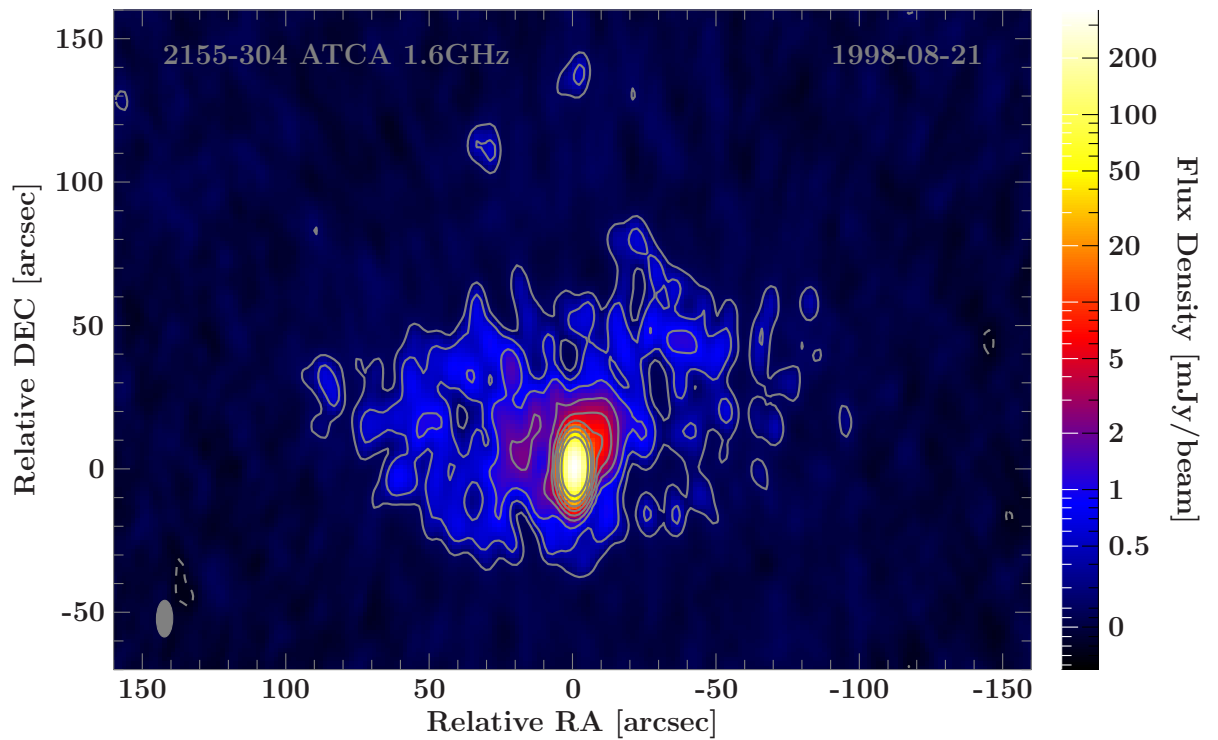


**Figure 3.31.:** ATCA image of 2155-304 observed at 1.4 GHz in standard 6 km configuration. RMS: 0.079 mJy, map-peak: 0.361 Jy, beam:  $(12.7 \times 5.64)$  arcsec at  $-0.695^\circ$ . Smallest contourlevel at three times RMS for positive and negative fluxdensities. The other contours changing exponential with base 2 in the positive fluxdensity regime. A bright core is visible and an extended emission halo with a source size of  $s \approx 200$  arcsec.

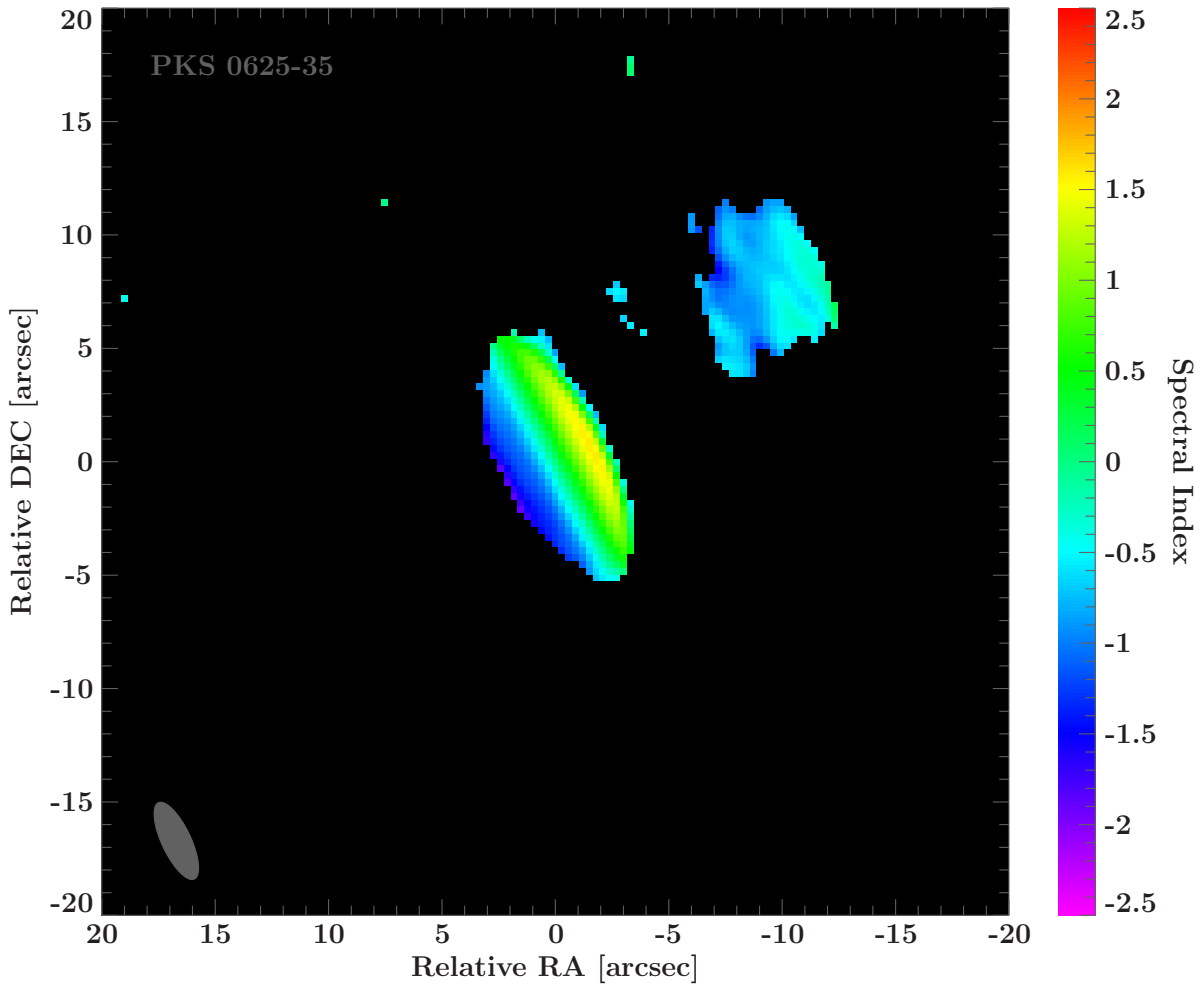


**Figure 3.32.:** Spectral index map of 2155-304 between the 1.4GHz VLA observation in figure 3.28 and the 4.8GHz VLA observation in figure 3.27. Flat core region with changing between positive and negative spectral indices because of different observation times. Steepening in the S-E direction and the N-W emission region down to  $\alpha \approx -1.5$ .

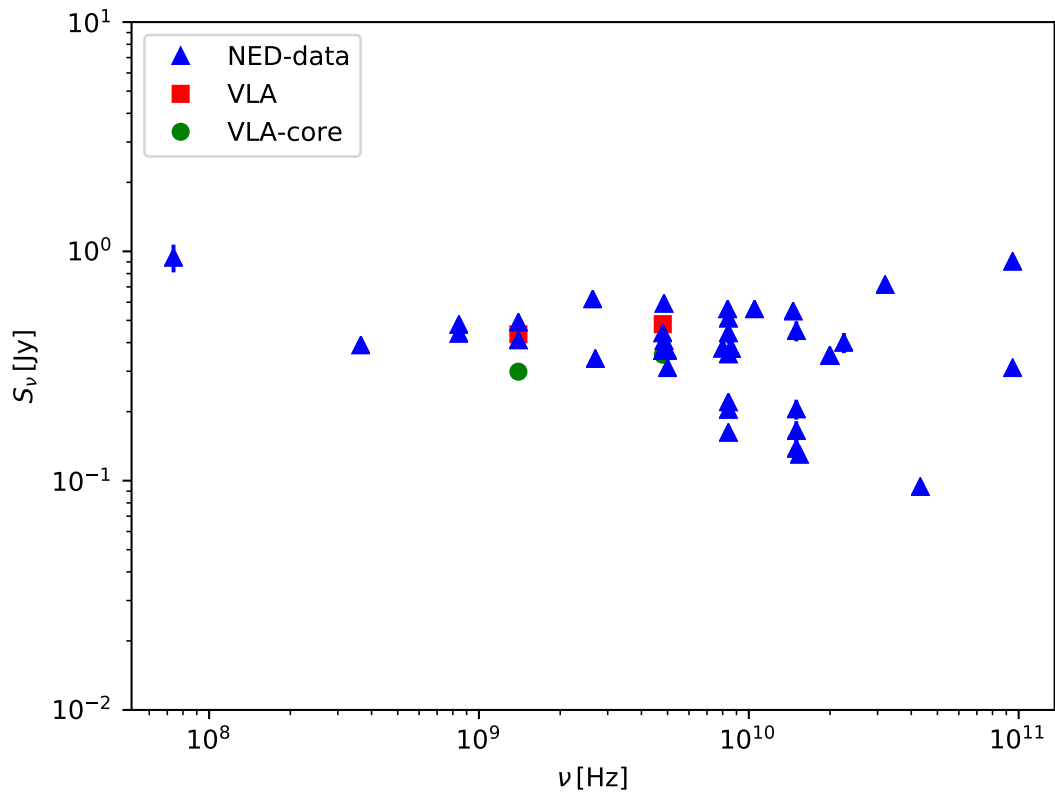


**Figure 3.33.:** Radio-spectrum of 2155 – 304 with the flux data of the NASA/IPAC Extragalactic Database (NED) as blue triangles and the flux measurements due to the analysis of the VLA images at  $\nu = 1.5$  GHz in figure 3.28 and at  $\nu = 4.8$  GHz in figure 3.27 as red squares and the core-fluxdensities for both frequencies as green circles.

## 4. Conclusion and outlook

In this study the extended emission of nine AGN, mainly blazar like object, was studied with respect to their luminosity and morphology using VLA observations at  $\nu = 1.4$  GHz and other frequencies. According to the unification scheme the subclass of blazars, BL Lacs and FSRQs, should be the beamed and rotated counterparts of FR1 and FR2 galaxies. All FSRQs lay in the luminosity regime of FR2 object as expected by the unification scheme, 1104-445 also show two hotspot, and 0402-362 only one. All BL Lacs except 0521-365 lay in the intermediate regime between FR1 and FR2, which is also consistent with unification. Only the Bl Lac 0521-365 is located in the FR2 regime, but this object shows also a one sided jet and a hotspot on the counterjet side, which is a hint for a more FR2 like behavior. For all sources with measured apparent jetspeed a envelope function for the apparent jet speed - core luminosity relation could be constrained. Also for single sources the inclination angle could be constrained, with the method of projected opening angles intruduced by [Burd \(2017\)](#). An interesting fact is that in most of the sources jet bending is present not only in not that powerful FR1 like objects but also in FR2 like object. Also there are two objects with asymmetric morphologies such as hotspots only on one side visible, which could for one reason that the second hotspot is hidden behind the core or the central engine by itself is build up asymmetric like the 'flip-flop effect' introduced by [Rudnick & Edgar \(1984\)](#). In the study of 1104-445 a discrepancy between high inclination angle calculated in this study and the high apparent jet speed of about  $\beta_{\text{app}}$  respectively low inclination angle by the VLBI study of [Trüstedt \(2013\)](#) was detected. By comparing the resulting deprojected size calculated with the VLBI inclination angle with typical sizes of radio galaxies by [Lara et al. \(2001\)](#) leads to irregularities in the speed measurement analysis in the study. In future work the analysis for all sources should be elaborated, meaning every source should be analyzed at minimum two frequencies to study the spectral behavior. For all sources with calculated spectral index map the image with smaller beam should be tapered get a more meaningful result for the spectral behavior. With regards of the study by [Kharb et al. \(2010\)](#) and the expansion on the southern hemisphere, a proposal for all sources in the TANAMI sample observable with the GMRT could be applied.



# Danksagung

An dieser Stelle möchte ich mich ganz herzlich bei all den Leuten bedanken ohne die diese Arbeit niemals möglich gewesen wäre.

Als erstes möchte ich mich bei meinem Betreuer Matthias Kadler bedanken, der mein Interesse in der Vorlesung Atmosphären- und Weltraumphysik für die Arbeit in der Astronomie geweckt hat und auch schon während meiner Bachelorarbeit betreut hat und dass er mir die Möglichkeit gegeben hat an diesem Projekt zu arbeiten. Seine Vorlesung zu extragalaktischen Jets und die Diskussionen über meine Arbeit haben mich immer inspiriert und motiviert.

Zudem möchte ich mich bei Paulingenfeldth Ray Burd für die hervorragende Betreuung bedanken und dass ich in diesem Projekt mitarbeiten durfte. Er hat mich bestens in das Thema eingeführt und war immer da, wenn ich Fragen hatte und desweiteren war er mir in dieser Zeit auch immer eine freundschaftliche Stütze.

Desweiteren vielen Dank auch an Karl Mannheim für die tolle Unterstützung während der Arbeit und für die gute Zusammenarbeit während ich die Übungen für die Vorlesung Einführung in die Astronomie betreuen durfte.

Danke auch an Michael Seeg, mit dem ich gemeinsam in diesem Projekt an 2155-304 gearbeitet habe, und Amar Hekalo, der einzelne Quellen aus meinem Sample im VLBI bearbeitet, für zahlreiche konstruktive Diskussionen .

Überdies möchte ich mich bei allen Leuten des Lehrstuhls für Astronomie bedanken, die mich immer unterstützt haben und mich hier herzlich aufgenommen hab. Besonderer Dank gilt hier auch Lukas Schrenk und der Spezi-Kasse.

Ganz besonders möchte ich mich auch bei meinen Eltern und meiner Schwester danken die mich in allen Dingen in meinem Studium unterstützen und einfach in jeder Situation für mich da sind.

This research has made use of the United States Naval Observatory (USNO) Radio Reference Frame Image Database (RRFID).

This research has made use of ISIS functions provided by ECAP/Remeis observatory and MIT (<http://www.sternwarte.uni-erlangen.de/isis/>).

This research has made use of the NASA/IPAC Extragalactic Database (NED) which is operated by the Jet Propulsion Laboratory, California Institute of Technology, under contract with the National Aeronautics and Space Administration.



# List of Figures

1.1.	Illustration of the unification model of active galactic nuclei by Beckmann & Shrader (2012). The lower part of the image represents the model of a radio-quiet AGN, with the subclasses Seyfert 1 galaxies and Seyfert 2 galaxies, distinguished by the inclination angle (appearance of broad emission lines in the spectrum). The upper part shows the case of radio loud AGN (objects with prominent particle jet), on the right side the lower luminous objects and on the left side the objects with higher radio luminosity. The objects with low inclination angles are called blazars the objects with high inclination angles are radio galaxies. . . . .	5
1.2.	The radio illustration of surface brightness distribution of 3C 272 observed at $\nu = 5$ GHz with the VLA adapted Beckmann & Shrader (2012) shows the source on kiloparsec scales. The radio fluxdensity is color scaled with red, high fluxdensity, and blue, low fluxdensity. 3C 272 belongs to the more low luminous FR1 radio galaxies. The morphology is dominated by a bright radio core. A two sided jet is visible with decreasing surface brightness going to the outer parts of the jets. In the outer parts more complex plumes are visible. . . . .	7
1.3.	The radio illustration of surface brightness distribution of 3C 175 observed at $\nu = 5$ GHz with the VLA adapted from Beckmann & Shrader (2012) shows the source on kiloparsec scales. The radio fluxdensity is color scaled with withe/bright red, high fluxdensity and black/dark red, low fluxdensity. 3C 175 belongs to the high luminous FR2 radio galaxies. The morphology of the source consists of a bright core in the middle, a faint jet in the S-W direction and two hotspots with lobes in S-W and N-E direction, where the jets terminate, because of deceleration by the intergalactic medium. . . . .	8
1.4.	Illustration of the beamed synchrotron radiation of a single electron with a relativistic circulation around a magnetic field. The radiation is emitted in a cone with opening angle $\theta$ . Credits: Rybicki & Lightman (1979). . .	10
1.5.	Illustration of the difference of a beamed synchrotron emission spectrum (blue) and unbeamd synchrotron emission spectrum (red) of the same electron distribution with spectral index $\alpha$ . By Burd (2017). . . . .	11

1.6.	Illustration of the composition of a blazar spectrum, consisting of a flat spectrum part caused by the beamed core emission and the steep part of the spectrum caused by the unbeamed extended emission of the source. The flat part of the spectrum is the result of the superposition of the beamed spectra of single emission regions of the jet, peaking at different frequencies. Adapted from Burd (2017). . . . .	12
1.7.	Scheme of a two element interferometer, with two single-dish telescopes pointing in the direction of $S$ with baseline $b_\lambda$ and geometrical time-delay $\tau_g$ between the two telescopes. Also an instrumental delay and the correlator is shown. . . . .	16
1.8.	Sketch of the different coordinate-systems used to explain radio interferometry of two antennas with spacing of one baseline $b_\lambda$ . The radiation arrives at the right antenna with a geometrical delay of $\tau_g$ according to the left reference antenna. The grey emission area from which the radiation of the object comes from is given in coordinates $l,m,n$ and the baselines of the array is represented by the $u,v,w$ coordinated. Figure by Burd (2017). . . . .	17
1.9.	Image of the whole VLA at D-configuration with maximal baselines of 1.03 km. <i>Credits: Image courtesy of NRAO/AUI</i> . . . . .	19
1.10.	Illustration of the locations of the different telescopes and subarrays of the TANAMI-project. <i>Credits by M. Kadler and J. Wilms</i> . . . . .	23
2.1.	Illustration for the explanation of the closurephases. A, B, C represent three telescopes of the considered array, the arrows the signal flux between the antennas. $\varphi_{AB}$ , $\varphi_{BC}$ and $\varphi_{CA}$ are the phases of two considered telescopes. $\delta_A$ , $\delta_B$ and $\delta_C$ represent the errors introduced by every single telescope. . . . .	31
2.2.	Optical image of 0521-365 observed with the ESO NTT at the optical R-band by Falomo (1994). The host galaxy was filtered and is located at the black cross in the image. A jet extending beginning at component 'A' up to component 'B' in N-W direction with a length of about 6 arcsec. Alongside the jet axis at a separation of about 1 arcsec from the end of the jet is also a bright red tip visible (component 'C'), which could be caused by a background galaxy. . . . .	36
2.3.	VLA image of 0521-365 at 15.1 GHz in A-B configuration by Keel (1986) reimaged. RMS: 0.30 mJy, map-peak: 2.16 Jy, beam: $(0.490 \times 0.368)$ arcsec at $20.9^\circ$ . Smallest contourlevel at three times RMS for positive and negative fluxdensities. The other contours changing exponential with base 2 in the positive fluxdensity regime. A one-sided jet in north-western direction is visible together with a hotspot and lobe in south-eastern direction. . . . .	37
2.4.	235 MHz image of 2155-304 observed by the GMRT; the source shows a typical FR1 structure. Credits by Pandey-Pommier et al. (2016) . . . . .	40

2.5.	610 MHz image of 2155-304 observed by the GMRT; the source shows a typical FR1 structure. Credits by Pandey-Pommier et al. (2016) . . . . .	40
2.6.	VLA C-configuration image of 2155-304 at 1.5 GHz first described by Ulvestad & Antonucci (1986); the data are new calibrated and reimaged for this study. . . . .	40
2.7.	VLBI images of all sources of the sample. All images except the image <b>c)</b> , was observed at $\nu = 8.4$ GHz. Image <b>c)</b> of 0438-436 was observed at $\nu = 4.8$ GHz. Images <b>d)-i)</b> are obtained from TANAMI observations of Ojha et al. (2010), image <b>b)</b> from TANAMI studies of Müller et al. (2017) and images <b>a)</b> and <b>c)</b> are taken out of the U.S. Naval Observatory archive. Jet directions: <b>a)</b> : N; <b>d)</b> : N-W; <b>h)</b> : W; <b>c)</b> , <b>f)</b> and <b>i)</b> : S-E; <b>b)</b> and <b>g)</b> : E; <b>e)</b> : N-E with possible jet bending anticlockwise. . . . .	41
2.8.	Illustration of the calculation of the inclination-angle using the projected $\zeta'$ and the deprojected opening angle $\zeta$ of a radio-jet. <b>a)</b> : Relation between the projected $s'$ and deprojected length $s$ and the inclination angle $\vartheta$ of the jet. <b>b)</b> : Relation between $s$ , the deprojected opening angle $\zeta$ and the diameter of the jet $b$ . <b>c)</b> : Relation between $s'$ , the projected opening angle $\zeta'$ and the diameter of the jet $b$ . Adapted from Burd (2017) . . . . .	44
2.9.	Illustration of the measurement of the projected opening angle $\zeta'$ . The Relation between the core-distance $d_{\text{core}}$ and the major axis $\theta_{\text{maj}}$ is used compute the projected angle. . . . .	44
2.10.	Histogram for the distribution of opening angles of 55 FR1 radio galaxies according to Parma et al. (1987) with a binning of $\Delta\zeta = 4^\circ$ and a minimal value of $\zeta_{\text{min}} = 3.4^\circ$ and a maximal of $\zeta_{\text{max}} = 33.4^\circ$ . The data are fitted with a Gaussian function to get the most probable opening angle $\zeta_{\text{mp}} = 10.9^\circ$ , adapted from Burd (2017). . . . .	46
2.11.	Histogram for the distribution of opening angles of 27 FR2 radio galaxies according to Jeyakumar & Saikia (2000) with a binning of $\Delta\zeta = 1^\circ$ and a minimal value of $\zeta_{\text{min}} = 1.4$ and a maximal of $\zeta_{\text{max}} = 19.6$ . The data are fitted with a Gaussian function to get the most probable opening angle $\zeta_{\text{mp}} = 2.5^\circ$ adapted from Burd (2017). . . . .	46
3.1.	Apparent jet speed as function of the core-luminosity, shown in logarithmic scale. FSRQs in red and Bl Lac in blue. The references of the single apparent speeds are shown in table 3.1. The envelope function in blue is calculated according to equation 3.1.1. . . . .	50
3.2.	Apparent jet speed as function of the extended luminosity, shown in logarithmic scale. FSRQs in red and Bl Lac in blue. The references of the single apparent speeds are shown in table 3.1.1s. . . . .	50
3.3.	Extended luminosity as function of the core-luminosity, both shown in logarithmic scale. FSRQs in red and Bl Lac in blue . . . . .	51

3.4.	Extended luminosity, in logarithmic scale, as function of the redshift. FSRQs in red and Bl Lac in blue. The the lower dashed line indicate the upper limit for the extended luminosity of FR1-objects and the upper line the lower limit of FR2-objects at $\nu = 1.4$ GHz according to Kharb et al. (2010) . . . . .	51
3.5.	VLA image of 0402-362 observed at 1.5 GHz in A-configuration. RMS: 0.16 mJy, map-peak: 1.11 Jy, beam: $(3.51 \times 1.26)$ arcsec at $-10.5^\circ$ . Smallest contourlevel at three times RMS for positive and negative fluxdensities. The other contours changing exponential with base 2 in the positive flux-density regime. A bright core and a bright hotspot-like emission region up to $d_{\text{core}} \approx 15$ arcsec in southern direction is visible. . . . .	53
3.6.	VLA image of 0402-362 observed at 4.8 GHz in A-configuration. RMS: 0.15 mJy, map-peak: 1.07 Jy, beam: $(1.31 \times 0.393)$ arcsec at $13.5^\circ$ . Smallest contourlevel at three times RMS for positive and negative fluxdensities. The other contours changing exponential with base 2 in the positive flux-density regime. A bright core and a bright hotspot-like emission region at $d_{\text{core}} \approx 12$ arcsec in southern direction is visible. . . . .	54
3.7.	3-sigma spectralindex-map between the images 1.4 GHz in figure 3.5 and 4.8 GHz in figure 3.6. Flat core region with changing between positive and negative spectralindices because of different observation times. Steepening in the hotspot like structure down to $\alpha \approx -1.5$ . . . . .	55
3.8.	VLA image of 0426-380 observed at 1.5 GHz in A-configuration. RMS: 0.14 mJy, map-peak: 0.663 Jy, beam: $(6.57 \times 1.41)$ arcsec at $23.6^\circ$ . Smallest contourlevel at three times RMS for positive and negative fluxdensities. The other contours changing exponential with base 2 in the positive fluxdensity regime. A bright core is visible and a jet extending up to $d_{\text{core}} \approx 5$ arcsec in north western direction. . . . .	57
3.9.	VLA image of 0438-436 observed at 1.5 GHz in A-configuration. RMS: 0.64 mJy, map-peak: 5.02 Jy, beam: $(6.77 \times 1.43)$ arcsec at $-12.6^\circ$ . Smallest contourlevel at three times RMS for positive and negative fluxdensities. The other contours changing exponential with base 2 in the positive fluxdensity regime. A bright core is visible and a jet extending up to $d_{\text{core}} \approx 3$ arcsec in south western direction. . . . .	58
3.10.	VLA image of 0402-362 observed at 1.3 GHz in A-configuration. RMS: 2.8 mJy, map-peak: 3.84 Jy, beam: $(4.05 \times 1.42)$ arcsec at $-6.44^\circ$ . Smallest contourlevel at three times RMS for positive and negative fluxdensities. The other contours changing exponential with base 2 in the positive flux-density regime. A bright core is visible, a jet extending in north-eastern direction and a bright spot at $d_{\text{core}} = 8.4$ arcsec in southern direction is visible. Also an extension in south-western direction identifiable. The source is surrounded by a bright halo. The overall size of the source alongside the jet is about $s \approx 35$ arcsec . . . . .	61

---

3.11. Spectral map of 0521-365 between the VLA 1.5 GHz observation of figure 3.10 and the VLA 15 GHz observation of figure 2.3. Flat core region. Steepening in the hotspot down to $\alpha \approx -0.6$ and in the jet and lobe down to $\alpha \approx -1.5$ . . . . .	62
3.12. Radio-spectrum of 0521 – 365 with the flux data of the NASA/IPAC Extragalactic Database (NED) as blue triangles and the flux measurements due to the analysis of the VLA image at $\nu = 1.4$ GHz in figure 3.10 as red square and the core-fluxdensity as green circles. . . . .	63
3.13. VLA image of 0537-441 observed at 4.8 GHz in A-configuration. RMS: 1.6 mJy, map-peak: 6.10 Jy, beam: $(1.84 \times 0.453)$ arcsec at $1.44^\circ$ . Smallest contourlevel at three times RMS for positive and negative fluxdensities. The other contours changing exponential with base 2 in the positive fluxdensity regime. A bright core is visible and an extension in eastern direction. . . . .	65
3.14. VLA image of 0537-441 observed at 1.5 GHz in A-configuration. RMS: 2.0 mJy, map-peak: 4.22 Jy, beam: $(5.56 \times 1.49)$ arcsec at $-6.42^\circ$ . Smallest contourlevel at three times RMS for positive and negative fluxdensities. The other contours changing exponential with base 2 in the positive fluxdensity regime. A bright core is visible and a jet extending up to $d_{\text{core}} \approx 5$ arcsec in north western direction, with a bending in southern direction up to $d_{\text{core}} \approx 10$ arcsec . . . . .	66
3.15. ATCA image of 0537-441 observed at 1.5 GHz in standard 6 km configuration. RMS: 0.84 mJy, map-peak: 2.84 Jy, beam: $(11.5 \times 7.36)$ arcsec at $-2.85^\circ$ . Smallest contourlevel at three times RMS for positive and negative fluxdensities. The other contours changing exponential with base 2 in the positive fluxdensity regime. A bright core is visible and an emission region up to $d_{\text{core}} \approx 50$ arcsec in southern direction. . . . .	67
3.16. Tapered VLA image of 0537-441 observed at 1.5 GHz in A-configuration. RMS: 1.6 mJy, map-peak: 6.10 Jy, beam: $(11.5 \times 7.36)$ arcsec at $-2.85^\circ$ . Smallest contourlevel at three times RMS for positive and negative fluxdensities. The other contours changing exponential with base 2 in the positive fluxdensity regime. A bright core is visible and an emission region up to $d_{\text{core}} \approx 35$ arcsec in southern direction and on in north eastern direction up to $d_{\text{core}} \approx 20$ arcsec . . . . .	68
3.17. Spectral map of 0537-441 between the VLA 1.5 GHz observation of figure 3.14 and the VLA 4.8 GHz observation of figure 3.13. Flat core region with changing between positive and negative spectralindices because of different observation times. Steepening in the outer regions down to $\alpha \approx -1.5$ . . . . .	69

3.18. Radio-spectrum of 0537 – 441 with the flux data of the NASA/IPAC Extragalactic Database (NED) as blue triangles and the flux measurements due to the analysis of the VLA images at $\nu = 1.5$ GHz in figure 3.14 and at $\nu = 4.8$ GHz in figure 3.13 as red squares. . . . .	70
3.19. VLA image of 0625-354 observed at 4.9 GHz in C-configuration. RMS: 0.13 mJy, map-peak: 0.844 Jy, beam: $(5.45 \times 3.94)$ arcsec at $39.2^\circ$ . Smallest contourlevel at three times RMS for positive and negative fluxdensities. The other contours changing exponential with base 2 in the positive flux-density regime. A bright core is visible and a FR1 like extended emission with an overall size of $s \approx 200$ arcsec. . . . .	72
3.20. VLA image of 0625-354 observed at 1.5 GHz in C-configuration. RMS: 0.33 mJy, map-peak: 1.36 Jy, beam: $(19.5 \times 11.5)$ arcsec at $39.2^\circ$ . Smallest contourlevel at three times RMS for positive and negative fluxdensities. The other contours changing exponential with base 2 in the positive flux-density regime. A bright core is visible and a FR1 like extended emission with an overall size of $s \approx 200$ arcsec. . . . .	73
3.21. Spectral index map of 0625-354 between the VLA observations at 1.5 GHz in figure 3.20 and the 4.9 GHz VLA observation in figure 3.19. Flat core region. Steepening in the plumes to $\alpha \approx -2.5$ . . . . .	74
3.22. Radio-spectrum of 0625 – 354 with the flux data of the NASA/IPAC Extragalactic Database (NED) as blue triangles and the flux measurements due to the analysis of the VLA images at $\nu = 1.5$ GHz in figure 3.20 and at $\nu = 4.8$ GHz in figure 3.19 as red squares and the core-fluxdensities for both frequencies as green circles. . . . .	75
3.23. VLA image of 1104-445 observed at 1.5 GHz in A-configuration. RMS: 0.37 mJy, map-peak: 2.85 Jy, beam: $(6.5 \times 1.3)$ arcsec at $1.44^\circ$ . Smallest contourlevel at three times RMS for positive and negative fluxdensities. The other contours changing exponential with base 2 in the positive flux-density regime. A bright core is visible and an extension in north eastern direction. Also two hotspot-like emission regions are visible at One in north eastern direction and one in south western direction. . . . .	77
3.24. Time evolution of the associated components of figure ?? with linear fit for the evolution of every component. The components are coded in the same color like in figure ?. By Trüstedt (2013) . . . . .	78
3.25. Apparent jet speed as function of the inclinaton angle <i>vartheta</i> . The function is presented with Lorentz-factors equal to the most probable, the minimal and the maximal apparent jet speed measured by Trüstedt (2013) and also with $\gamma \rightarrow \infty$ . . . . .	79

---

3.26. VLA image of 1313-333 observed at 1.4 GHz in A-configuration. RMS: 2.2 mJy, map-peak: 1.02 Jy, beam: $(2.89 \times 1.46)$ arcsec at $5.85^\circ$ . Smallest contourlevel at three times RMS for positive and negative fluxdensities. The other contours changing exponential with base 2 in the positive flux-density regime. A bright core is visible and an extension in eastern direction.	81
3.27. VLA image of 2155-304 observed at 4.8 GHz in A-configuration. RMS: 0.084 mJy, map-peak: 0.389 Jy, beam: $(1.29 \times 0.406)$ arcsec at $27.3^\circ$ . Smallest contourlevel at three times RMS for positive and negative fluxdensities. The other contours changing exponential with base 2 in the positive flux-density regime. A bright core is visible and an extension in south eastern direction. up to about $d_{\text{core}} \approx 2$ arcsec.	84
3.28. VLA image of 2155-304 observed at 1.4 GHz in A-configuration. RMS: 0.078 mJy, map-peak: 0.312 Jy, beam: $(3.71 \times 1.28)$ arcsec at $25.2^\circ$ . Smallest contourlevel at three times RMS for positive and negative fluxdensities. The other contours changing exponential with base 2 in the positive flux-density regime. A bright core is visible and an emission region in north western direction. up to about $d_{\text{core}} \approx 15$ arcsec.	85
3.29. Tapered VLA image of 2155-304 observed at 4.8 GHz in A-configuration. RMS: 0.084 mJy, map-peak: 0.389 Jy, beam: $(3.71 \times 1.28)$ arcsec at $25.2^\circ$ . Smallest contourlevel at three times RMS for positive and negative fluxdensities. The other contours changing exponential with base 2 in the positive fluxdensity regime. bright core is visible and an emission region in north western direction. up to about $d_{\text{core}} \approx 15$ arcsec.	86
3.30. The typical FR1 radio galaxy 3C31 (from: <a href="http://www.cv.nrao.edu/">http://www.cv.nrao.edu/</a> ) is presented for the edge on view of an FR1 object, compared with the blazar view of an FR1 object for this case 2155 – 304 observed with the VLA at $\nu = 4.8$ GHz and with the GMRT at $\nu = 1.4$ GHz. As shown both images of 2155-304 show several parts of the jet.	87
3.31. ATCA image of 2155-304 observed at 1.4 GHz in standard 6 km configuration. RMS: 0.079 mJy, map-peak: 0.361 Jy, beam: $(12.7 \times 5.64)$ arcsec at $-0.695^\circ$ . Smallest contourlevel at three times RMS for positive and negative fluxdensities. The other contours changing exponential with base 2 in the positive fluxdensity regime. A bright core is visible and an extended emission halo with a source size of $s \approx 200$ arcsec.	88
3.32. Spectral index map of 2155-304 between the 1.4 GHz VLA observation in figure 3.28 and the 4.8 GHz VLA observation in figure 3.27. Flat core region with changing between positive and negative spectralindices because of different observation times. Steepening in the S-E direction and the N-W emission region down to $\alpha \approx -1.5$ .	89

3.33. Radio-spectrum of 2155 – 304 with the flux data of the NASA/IPAC Extragalactic Database (NED) as blue triangles and the flux measurements due to the analysis of the VLA images at $\nu = 1.5$ GHz in figure 3.28 and at $\nu = 4.8$ GHz in figure 3.27 as red squares and the core-fluxdensities for both frequencies as green circles. . . . .	90
A.1. Radio-spectrum of 0402 – 362 with the flux data of the NASA/IPAC Extragalactic Database (NED) as blue triangles and the flux measurements due to the analysis of the VLA images at $\nu = 1.5$ GHz in figure 3.5 and at $\nu = 4.8$ GHz in figure 3.6 as red squares. . . . .	109
A.2. Radio-spectrum of 0426 – 380 with the flux data of the NASA/IPAC Extragalactic Database (NED) as blue triangles and the flux measurements due to the analysis of the VLA image at $\nu = 1.4$ GHz in figure 3.8 as red square. . . . .	110
A.3. Radio-spectrum of 0438 – 436 with the flux data of the NASA/IPAC Extragalactic Database (NED) as blue triangles and the flux measurements due to the analysis of the VLA image at $\nu = 1.4$ GHz in figure 3.9 as red square. . . . .	110
A.4. Radio-spectrum of 1104 – 445 <sub>spec</sub> with the flux data of the NASA/IPAC Extragalactic Database (NED) as blue triangles and the flux measurement due to the analysis of the VLA image at $\nu = 1.5$ GHz in figure 3.23 as red squares. . . . .	111
A.5. Radio-spectrum of 1313 – 333 with the flux data of the NASA/IPAC Extragalactic Database (NED) as blue triangles and the flux measurements due to the analysis of the VLA image at $\nu = 1.4$ GHz in figure 3.26 as red square. . . . .	111

# List of Tables

1.1.	VLA-bands with their frequency-range, the time of operation and the angular resolution for the four main configurations A-D. . . . .	20
1.2.	Every actual radio telescope of the TANAMI project is listed with its name, the diameter and the location of the antenna. . . . .	22
2.1.	All sources of the sample ordered by $\gamma$ -loudness, with name, the AGN class, redshift $z$ , fermi $\gamma$ -flux $S_\gamma$ between $100 \text{ MeV} < E_\gamma < 100 \text{ GeV}$ , the photon-index $\Gamma$ in this energy range, radio fluxdensity $S_R$ at $\nu = 1.4 \text{ GHz}$ and the $\gamma$ -loudnes $G$ . The upper part contains the $\gamma$ -loudest sources of the TANAMI sample observed with the VLA and the lower part the three $\gamma$ -quiet sources for comparison. . . . .	34
3.1.	The classification the redshift $z$ , the apparent speed $\beta_{\text{app}}$ , the core-luminosity $L_{\text{core}}$ and the extended luminosity $L_{\text{ext}}$ is shown for each source of the sample.	49
3.2.	Summary of the model-components of 0426-380. For each component the name (Comp.) the fluxdensity $S_\nu$ , the core-distance $d_{\text{core}}$ , the position-angle $\theta$ and the major-axis $\theta_{\text{maj}}$ is shown. The table is split in two parts. The first row shows the modelfit for the core with an unresolved component. The other rows shows the object modeled with 3 model-components including one core-component . . . . .	56
3.3.	Summary of the model-components of 0537–441. For each component the name (Comp.) the fluxdensity $S_\nu$ , the core-distance $d_{\text{core}}$ , the position-angle $\theta$ and the major-axis $\theta_{\text{maj}}$ is shown. The table is split in two parts. The first two rows shows the modelfit for the ATCA image. The other rows shows the object modeled with 4 extended model-components and the model for the unresolved core for the 1.4 GHz VLA observation. . . . .	71
3.4.	Summary of the model-components of the jet region of 0625 – 354. For each component the name (Comp.) the fluxdensity $S_\nu$ , the core-distance $d_{\text{core}}$ , the position-angle $\theta$ , the major-axis $\theta_{\text{maj}}$ and the apparent jet opening angle $\zeta'$ is shown. . . . .	74
3.5.	Summary of the model-components of 1104–445. For each component the name (Comp.) the fluxdensity $S_\nu$ , the core-distance $d_{\text{core}}$ , the position-angle $\theta$ , the major-axis $\theta_{\text{maj}}$ , the projected opening angle $\zeta'$ and the most probable $\vartheta_{\text{mp}}$ and minimal inclination angle $\vartheta_{\text{min}}$ is shown. . . . .	78

- 3.6. Summary of the model-components of 1313–333. For each component the name (Comp.) the fluxdensity  $S_\nu$ , the core-distance  $d_{\text{core}}$ , the position-angle  $\theta$ , the major-axis  $\theta_{\text{maj}}$ , the projected opening angle  $\zeta'$  and the most probable  $\vartheta_{\text{mp}}$ , minimal inclination angle  $\vartheta_{\text{min}}$  and the maximal inclination angle  $\vartheta_{\text{max}}$  is shown. The upper part show the model only for the unresolved core model and the lower one the model for the whole source.

82

# Bibliography

- Abdo A.A., Ackermann M., Ajello M., et al., 2009, ApJ 700, 597
- Aharonian F., Akhperjanian A.G., Aye K.M., et al., 2005 430, 865
- Aharonian F., Akhperjanian A.G., Bazer-Bachi A.R., et al., 2007, ApJL 664, L71
- Antonucci R., 1993, ARA&A 31, 473
- Attridge J.M., Roberts D.H., Wardle J.F.C., 1999, ApJL 518, L87
- Beckmann V., Shrader C., 2012, In: Proceedings of “An INTEGRAL view of the high-energy sky (the first 10 years)” - 9th INTEGRAL Workshop and celebration of the 10th anniversary of the launch (INTEGRAL 2012)., p. 69
- Blandford R.D., Königl A., 1979, ApJ 232, 34
- Burd P.R., 2017, Master thesis, Julius-Maximilian-Universität Würzburg
- Burke B., Graham-Smith F., 2010, An Introduction to Radio Astronomy, Cambridge University Press
- Chiappetti L., Maraschi L., Tavecchio F., et al., 1999, ApJ 521, 552
- Cohen M.H., Lister M.L., Homan D.C., et al., 2007, ApJ 658, 232
- Condon J.J., 1988, Radio sources and cosmology, p.641
- Condon J.J., Cotton W.D., Greisen E.W., et al., 1998, AJ 115, 1693
- Costero R., Osterbrock D.E., 1977, ApJ 211, 675
- Czerny B., Li J., Loska Z., Szczerba R., 2004, MNRAS 348, L54
- Dahari O., De Robertis M.M., 1988, ApJS 67, 249
- Falomo R., 1994, The Messenger 77, 49
- Falomo R., Pesce J.E., Treves A., 1993, ApJL 411, L63
- Fanaroff B.L., Riley J.M., 1974, MNRAS 167, 31P

- Fanti C., Fanti R., Dallacasa D., et al., 1995, *A&A* 302, 317
- Frater R.H., Brooks J.W., Whiteoak J.B., 1992, *Journal of Electrical and Electronics Engineering Australia* 12, 103
- Gaskell C.M., Goosmann R.W., Antonucci R.R.J., Whysong D.H., 2004, *ApJ* 616, 147
- Gopal-KrishnaWiita P.J., 2000, *A&A* 363, 507
- Hachenberg O., Grahl B.H., Wielebinski R., 1973, *Proc. IEEE* 61, 1288
- Hartman R.C., Bertsch D.L., Bloom S.D., et al., 1999, *ApJS* 123, 79
- Healey S.E., Romani R.W., Taylor G.B., et al., 2007, *ApJS* 171, 61
- Heidt J., Tröller M., Nilsson K., et al., 2004, *A&A* 418, 813
- Högbom J.A., 1974, *A&AS* 15, 417
- Jauncey D.L., Batty M.J., Gulkis S., Savage A., 1982, *AJ* 87, 763
- Jennison R.C., 1958, *MNRAS* 118, 276
- Jeyakumar S., Saikia D.J., 2000, *MNRAS* 311, 397
- Jones D.H., Read M.A., Saunders W., et al., 2009, *MNRAS* 399, 683
- Kataoka J., Takahashi T., Makino F., et al., 2000, *ApJ* 528, 243
- Keel W.C., 1986, *ApJ* 302, 296
- Kellermann K.I., Sramek R., Schmidt M., et al., 1989, *AJ* 98, 1195
- Kharb P., Lister M.L., Cooper N.J., 2010, *ApJ* 710, 764
- Komesaroff M.M., Roberts J.A., Milne D.K., et al., 1984, *MNRAS* 208, 409
- Kovalev Y.Y., Kellermann K.I., Lister M.L., et al., 2005, *AJ* 130, 2473
- Lara L., Cotton W.D., Feretti L., et al., 2001, *A&A* 370, 409
- Lewis G.F., Ibata R.A., 2000, *ApJ* 528, 650
- Linford J.D., Taylor G.B., Schinzel F.K., 2012, *ApJ* 757, 25
- Lister M.L., Aller M., Aller H., et al., 2011, *ApJ* 742, 27
- Lister M.L., Aller M.F., Aller H.D., et al., 2013, *AJ* 146, 120
- Liu F.K., Xie G.Z., 1992, *A&AS* 95, 249

- Mannheim K., 1993, *A&A* 269, 67
- Maraschi L., Treves A., Schwartz D.A., Tanzi E.G., 1985, *ApJ* 294, 615
- Mie G., 1908, *Ann. Phys. (Leipzig)* 330, 377
- Morton D.C., Savage A., Bolton J.G., 1978, *MNRAS* 185, 735
- Müller C., Kadler M., Ojha R., et al., 2017, *ArXiv e-prints*
- Nolan P.L., Abdo A.A., Ackermann M., et al., 2012, *ApJS* 199, 31
- Nolan P.L., Bertsch D.L., Chiang J., et al., 1996, *ApJ* 459, 100
- Ojha R., Kadler M., Böck M., et al., 2010, *A&A* 519, A45
- Osterbrock D.E., Koski A.T., Phillips M.M., 1976, *ApJ* 206, 898
- Osterbrock D.E., Shuder J.M., 1982, *ApJS* 49, 149
- Padovani P., Giommi P., 1995, *MNRAS* 277, 1477
- Pandey-Pommier M., Sirothia S., Chadwick P., et al., 2016, In: Reylé C., Richard J., Cambrésy L., Deleuil M., Pécontal E., Tresse L., Vauglin I. (eds.) *SF2A-2016: Proceedings of the Annual meeting of the French Society of Astronomy and Astrophysics.*, p.373
- Parma P., Fanti C., Fanti R., et al., 1987, *A&A* 181, 244
- Perley R.A., Butler B.J., 2013, *ApJS* 204, 19
- Perley R.A., Chandler C.J., Butler B.J., Wrobel J.M., 2011, *ApJL* 739, L1
- Peterson B.A., Jauncey D.L., Condon J.J., Wright A.E., 1976, *ApJL* 207, L5
- Peterson B.A., Wright A.E., Jauncey D.L., Condon J.J., 1979, *ApJ* 232, 400
- Piner B.G., Edwards P.G., 2004, *ApJ* 600, 115
- Piner B.G., Mahmud M., Fey A.L., Gospodinova K., 2007, *Astron. J.* 133, 2357
- Piner B.G., Pant N., Edwards P.G., 2008, *ApJ* 678, 64
- Prestage R.M., Constantikes K.T., Hunter T.R., et al., 2009, *Proc. IEEE* 97, 1382
- Quintana H., Ramirez A., 1995, *A&AS* 96, 343
- Rösch F., 2016, Bachelor thesis, Julius-Maximilian-Universität Würzburg

- Rudnick L., Edgar B.K., 1984, ApJ 279, 74
- Rybicki G.B., Lightman A.P., 1979, Radiative processes in astrophysics, New York, Wiley-Interscience
- Sbarufatti B., Treves A., Falomo R., 2005, ApJ 635, 173
- Schellenberger G., Vrtilik J.M., David L., et al., 2017, ApJ 845, 84
- Schwarz U.J., 1978, A&A 65, 345
- Seeg M., 2017, Bachelor thesis, Julius-Maximilian-Universität Würzburg
- Seyfert C.K., 1943, ApJ 97, 28
- Shen Z.Q., Wan T.S., Moran J.M., et al., 1997, Astron. J. 114, 1999
- Stickel M., Fried J.W., Kuehr H., 1988 206, L30
- Stickel M., Meisenheimer K., Kuehr H., 1994, A&AS 105
- Taylor G.B., Carilli C.L., Perley R.A., (eds.) 1999, Synthesis Imaging in Radio Astronomy II, Vol. 180 of *Astronomical Society of the Pacific Conference Series*, Astronomical Society of the Pacific Conference Series
- Thompson A.R., Clark B.G., Wade C.M., Napier P.J., 1980 44, 151
- Thompson A.R., Moran J.M., Swenson, Jr. G.W., 2001, Interferometry and Synthesis in Radio Astronomy, 2nd Edition
- Tingay S.J., Jauncey D.L., King E.A., et al., 2003, PASJ 55, 351
- Trüstedt J., 2013, Master thesis, Julius-Maximilian-Universität Würzburg
- Ulvestad J.S., Antonucci R.R.J., 1986, Astron. J. 92, 6
- Urry C.M., Padovani P., 1995, PASP 107, 803
- Valtonen M.J., Lehto H.J., Nilsson K., et al., 2008, Nat 452, 851
- Venturi T., Morganti R., Tzioumis T., Reynolds J., 2000, A&A 363, 84
- Véron-Cetty M.P., Véron P., 2006, A&A 455, 773
- Vestrand W.T., Stacy J.G., Sreekumar P., 1995, ApJL 454, L93
- Wills K.A., Morganti R., Tadhunter C.N., et al., 2004, MNRAS 347, 771
- Wilson W.E., Ferris R.H., Axtens P., et al., 2011, MNRAS 416, 832

# A. Appendix

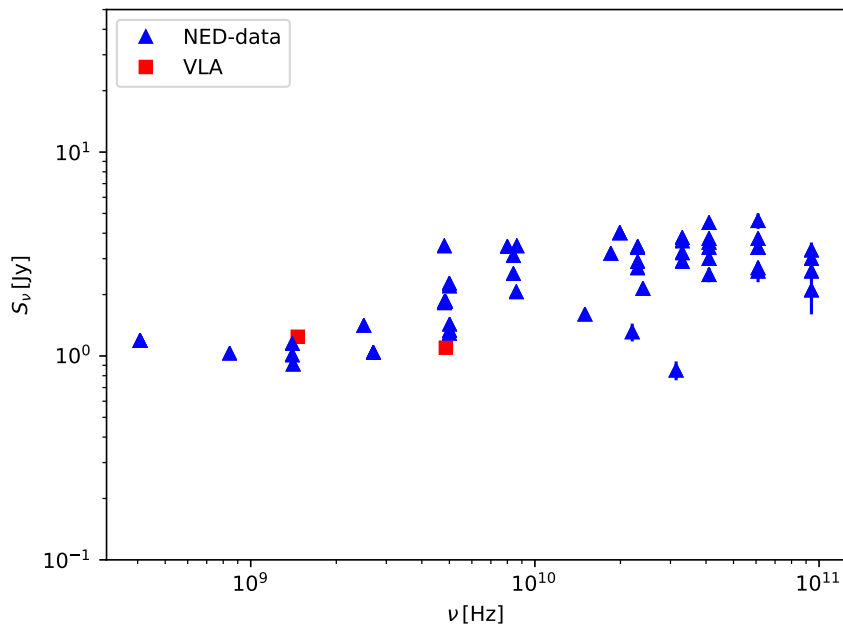


**Figure A.1.:** Radio-spectrum of 0402 – 362 with the flux data of the NASA/IPAC Extragalactic Database (NED) as blue triangles and the flux measurements due to the analysis of the VLA images at  $\nu = 1.5$  GHz in figure 3.5 and at  $\nu = 4.8$  GHz in figure 3.6 as red squares.

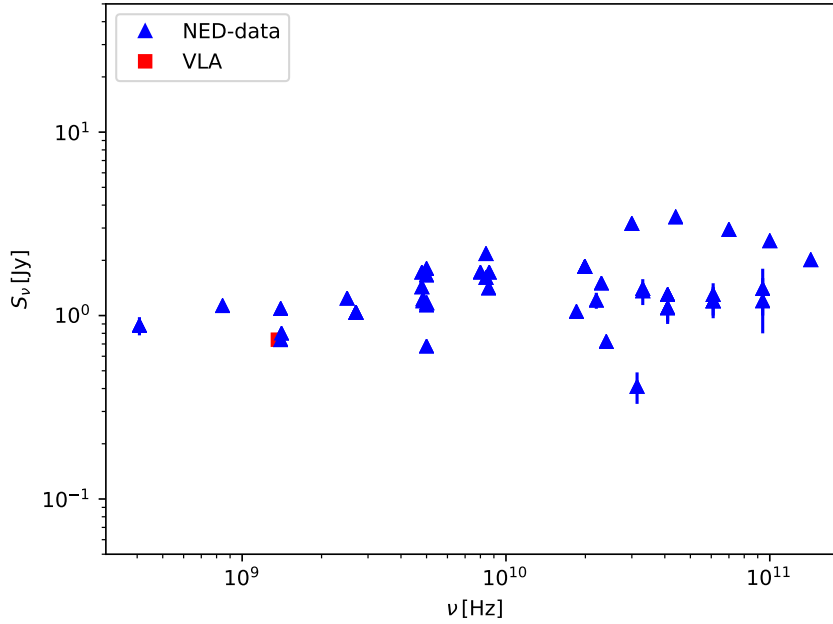


**Figure A.2.:** Radio-spectrum of 0426 – 380 with the flux data of the NASA/IPAC Extragalactic Database (NED) as blue triangles and the flux measurements due to the analysis of the VLA image at  $\nu = 1.4$  GHz in figure 3.8 as red square.

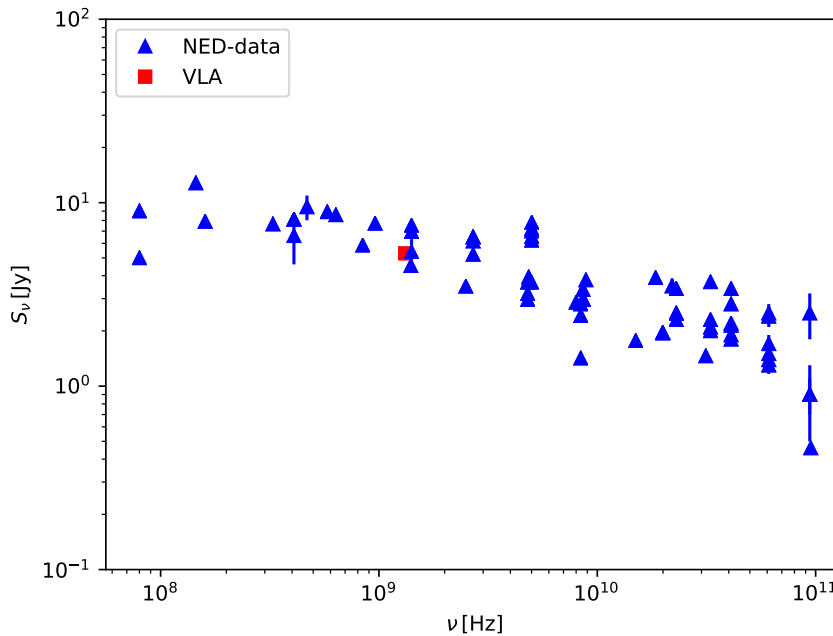


**Figure A.3.:** Radio-spectrum of 0438 – 436 with the flux data of the NASA/IPAC Extragalactic Database (NED) as blue triangles and the flux measurements due to the analysis of the VLA image at  $\nu = 1.4$  GHz in figure 3.9 as red square.

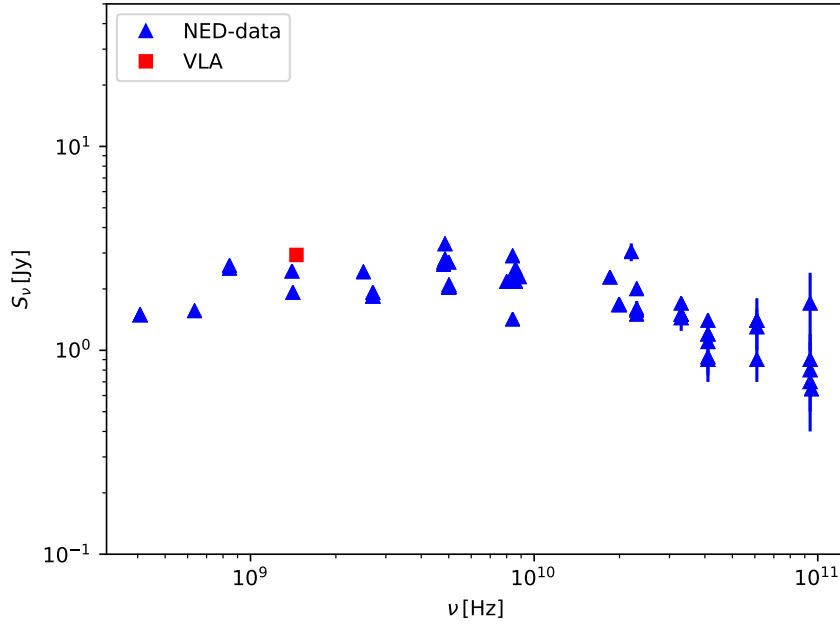


**Figure A.4.:** Radio-spectrum of 1104 – 445<sub>spec</sub> with the flux data of the NASA/IPAC Extragalactic Database (NED) as blue triangles and the flux measurement due to the analysis of the VLA image at  $\nu = 1.5$  GHz in figure 3.23 as red squares.

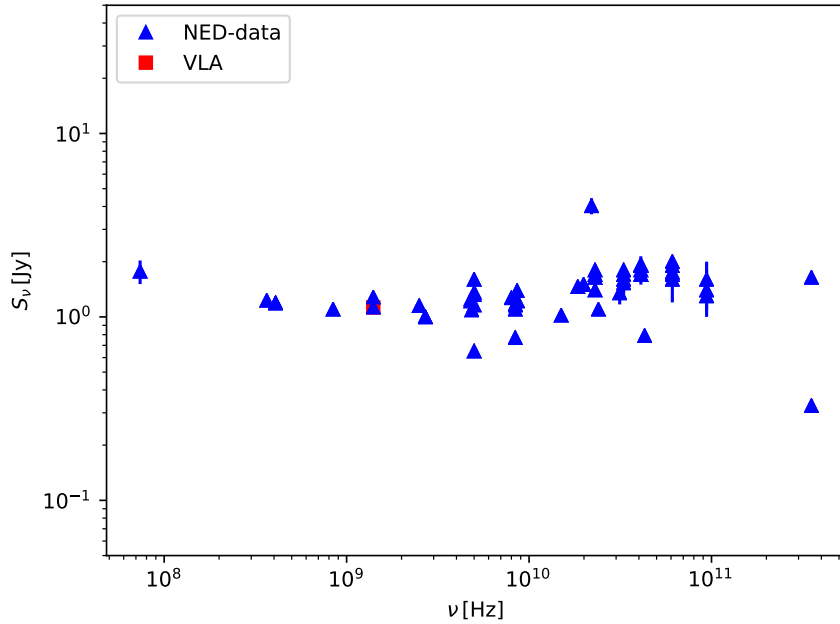


**Figure A.5.:** Radio-spectrum of 1313 – 333 with the flux data of the NASA/IPAC Extragalactic Database (NED) as blue triangles and the flux measurements due to the analysis of the VLA image at  $\nu = 1.4$  GHz in figure 3.26 as red square.



# Selbstständigkeitserklärung

Der Verfasser erklärt, dass er die vorliegende Arbeit selbständig, ohne fremde Hilfe und ohne Benutzung anderer als der angegebenen Hilfsmittel angefertigt hat. Die aus fremden Quellen (einschließlich elektronischer Quellen) direkt oder indirekt übernommenen Gedanken sind ausnahmslos als solche kenntlich gemacht. Die Arbeit ist in gleicher oder ähnlicher Form oder auszugsweise im Rahmen einer anderen Prüfung noch nicht vorgelegt worden.

---

Würzburg, 17. Januar 2018